Fast and Ultrafast Multiphoton-Multicolour Ionization and Spectroscopy of Small Quantum Systems

A thesis submitted for the degree of :
Doctor of Philosophy

Dublin City University (DCU)

School of Physical Sciences
National Center for Plasma Science and Technology (NCPST)

Military University of Technology (MUT)

Institute of Optoelectronics (IOE)

Lazaros Varvarezos
B. Sc., M. Sc.

Research Supervisors :
Prof. John Costello
Dr. hab. inż Andrzej Bartnik

June 22, 2020

Fast and Ultrafast Multiphoton-Multicolour Ionization and Spectroscopy of Small Quantum Systems

Thesis presented by

Lazaros Varvarezos

B. Sc., M. Sc.

Prof. John Costello
(Promoter)
Dublin City University

Dr. hab. inż Andrzej Bartnik
(Co-Promoter)
Military University of Technology

Doctoral Studies Panel Membership :
Prof. John Costello
Dr. hab. inż Andrzej Bartnik
Erasmus Mundus Joint Doctorate, EXTATIC

June 22, 2020

Declaration of Authorship

I hereby certify that this material, which I now submit for assessment on the programme of study leading to the award of Doctor of Philosophy is entirely my own work, that I have exercised reasonable care to ensure that the work is original, and does not to the best of my knowledge breach any law of copyright, and has not been taken from the work of others save and to the extent that such work has been cited and acknowledged within the text of my work.

Signed:

Date:

ID No.:

DUBLIN CITY UNIVERSITY

Abstract

Faculty of Science and Health

School of Physical Sciences

Doctor of Philosophy

Fast and Ultrafast Multiphoton-Multicolour Ionization and Spectroscopy of Small Quantum Systems

by Lazaros Varvarezos

The interaction of atoms (Kr) and small molecules (CO_2, CH_4), with laser light emitted by different types of sources was investigated.

Photoelectron spectroscopy was applied to study the two photon double ionization of krypton, induced by free electron laser (FEL) photons at 25.2 eV. Velocity map imaging (VMI) spectroscopy was also used to record the angular distributions of the photoelectrons for both the first and second ionization steps. The resolution of the spectrometer was high enough to allow for resolving the spin-orbit components in the photoelectron spectra. Measurements for different FEL intensities were performed to illustrate the intensity dependence for each spin-orbit component. The main result was the observation of an intensity dependent pattern, characteristic for each spin-orbit component.

Photoabsorption measurements around the carbon and oxygen K-edges were acquired for neutral 'not ionized' CO_2 and CH_4 molecules. Similar measurements were performed for the CO_2 and CH_4 photoionized plasmas. The photons used to create and subsequently probe the plasmas were emitted by a laser produced plasma (LPP) source based on the double stream gas puff target geometry. The main result, was the observation of atomic ions in the absorption spectra of the photoionized plasmas, contrary to the case of the 'not ionized' neutral molecules.

A comparative study was performed for methane irradiated by ultrafast laser pulses at 800 nm and 400 nm. Ionization and subsequent dissociation mechanisms were investigated via ion spectroscopy at different laser intensities for both the fundamental (800 nm) laser field and the second harmonic (400 nm) field. The main result was the observation of different fragmentation pathways for each laser wavelength. The fragmentation pathways were also found to be dependent on the laser intensity.

Acknowledgements

First I would like to thank my supervisor Prof. John Costello for his continuous support and encouragement over these years. Without his guidance the completion of this work would not have been possible. I would also like to thank Prof. Henryk Fiedorowicz and Dr. Andrzej Bartnik and the wider research group in MUT for their assistance and support during my mobility period. In addition, I am grateful for the opportunity to collaborate with Dr. Michael Meyer and his group members at XFEL in Hamburg.

A owe a big thank you to Dr. Mossy Kelly, Dr. Lampros Nikolopoulos and Assist. Prof. Manolis Benis for their ample support both in science and everyday life. Many thanks also go to Dr. Paddy Hayden. Furthermore, I would like to thank all the postgraduates in DCU (with special mention to Hu Lu), who shared this journey with me. I wish to express my appreciation to all the people I worked with during the beamtimes at FLASH and LCLS.

I wish to extend my sincere thanks to all the support staff in DCU and the NCPST including Pat Wogan, Sheila Boughton, Alan Hughes, Lisa Peyton, Des Lavelle and Irene Ryan.

Special thanks to my friends in Greece, particularly to the undergraduate squad (Vassilis, Nick, Kostas, Nikos, Padelis, Thomas) for all the good memories, physics was fun with you.

Finally, I would like to thank Karmel for her endless support in the tough moments, and of course my family to whom I dedicate this thesis.

Contents

Declaration of Authorship **i**

Abstract **iii**

Acknowledgements **iv**

List of Figures **xii**

List of Tables **xiii**

1 Introduction **1**

2 Sources in the NIR region **4**
2.1 Historical background 4
2.2 The 'fast' regime 5
2.3 The 'ultrafast' regime 9
2.4 The oscillator 9
2.5 The chirped pulse amplification (CPA) technique 13
2.6 The stretcher 13
2.7 The regenerative amplifier (RGA) 14
2.8 The compressor 16
2.9 Summary 16

3 Sources in the VUV and SXR spectral regions **17**
3.1 Synchrotron radiation 17
3.2 The free electron laser (FEL) principle 21
3.3 The micro-bunching process 22
3.4 The self amplified spontaneous emission (SASE) mechanism 24
3.5 The free electron laser facility in Hamburg (FLASH) 24
3.6 The photo-injector 25
3.7 The linear accelerator 25
3.8 The bunch compressor 26
3.9 The undulator 27
3.10 Properties of the FEL radiation 27
3.11 Table-top extreme ultraviolet/soft X-ray laser produced plasma source 30

3.11.1 Sources based on gas puff targets 30
3.12 Summary 32

4 VUV ionization of Kr **33**
4.1 Two-photon double-ionization 35
4.2 Experiment 40
4.3 Results and discussion 43
4.4 Angle-averaged photoelectron spectra 44
4.5 Angle-resolved photoelectron spectra for the first ionization step . . . 46
4.6 Angle-resolved photoelectron spectra for the second ionization step . . 48
4.7 Summary 51

5 Low temperature photoionized plasmas **52**
5.1 Photoabsorption of molecules in the soft X-ray region 53
5.2 Experiment 57
5.3 Results and discussion 62
5.4 Measurements on the carbon k-edge 62
5.5 Measurements on the oxygen k-edge 68
5.6 Summary 71

6 Molecules irradiated by intense laser fields ($\omega/2\omega$) **72**
6.1 Molecules in Intense laser fields 72
6.2 Experimental setup 74
6.2.1 The time of flight (TOF) spectrometer 75
6.3 Second harmonic generation 77
6.4 Results and discussion 79
6.5 Multistep dissociation of methane 79
6.6 Effect of laser intensity on the fragmentation mechanism 83
6.7 Summary 88

7 Summary and future work **89**

A The VMI technique **90**
A.1 Introduction 90
A.2 The Newton spheres 91
A.3 The inversion process 91

B Optimization of the LPP SXR source **93**

Bibliography **95**

List of Figures

2.1 The main stages of the Q-switching process for the generation of 'fast' laser pulses in the nanosecond regime. 5
2.2 Energy band diagram for the Nd:YAG active medium. It represents a four level system in which the ${}^4F_{3/2} \longrightarrow {}^4 I_{11/2}$ and the ${}^4F_{3/2} \longrightarrow {}^4 I_{13/2}$ transitions result in laser emission at 1064 nm and 1322 nm respectively. 6
2.3 (a) Longitudinal and (b) transverse arrangement of a Pockels cell. . . . 8
2.4 A typical Flashlamp-pumped, Q-switched Nd:YAG laser system [1]. . 8
2.5 (a) Energy level diagram for the Ti:Sapphire crystal used as the active medium for generation of ultrafast pulses (b) Absorption and emission spectra for the Ti:Sapphire crystal. 10
2.6 A representative oscillator cavity (Coherent Micra^{TM} series) [2]. The green Coherent Verdi^{TM} pump laser beam is directed towards the Ti:Sapphire crystal by a set of mirrors (R1, R2) while a polarizer (ROT) is placed between them. A lens (L1) is then used to focus the green beam in order to ensure that a population inversion is induced in the active medium (Ti:S). Subsequently, the generated red beam travels around a 'ring' cavity, formed by eight mirrors (M1-M8) before leaving the oscillator, while MAC is an auxiliary cavity end mirror. A pair of prisms (PR1, PR2) is used to compensate for the pulse broadening. After mirror M8 the beam passes through a beamsplitter (BS) where the reflected beam is directed towards two photodiodes (PD1, PD2) and the transmitted beam encounters a collimating lens (L2). 11
2.7 The main stages (oscillator, stretcher, amplifier, compressor) of the CPA technique used to generate ultrashort laser pulses. 13
2.8 A single grating stretcher [3]. This geometry includes a grating (SG) and 5 mirrors (SM6, SM7, SM8, SM9, SM10) to induce a linear positive chirp to the pulse [3]. 14
2.9 The regenerative amplifier [3]. Four mirrors (M1, M2, M3, M4) are used to form the laser cavity. Appropriate timing between two Pockels cells (PC1, PC2) ensures a sufficient number of roundtrips required for amplification. A rotating waveplate (RWP) is then used to eject the amplified laser pulse. Additional optical components include a quarter waveplate and two irises. 16

3.1 The radiation pattern emitted by a bending magnet. 18
3.2 The different sources of synchrotron radiation. 20
3.3 The measured FLASH peak brilliance compared to other sources. . . . 21
3.4 The 'slippage' effect. The faster propagation of the emitted electromagnetic radiation results in a 'slippage' of the more slowly moving electrons with respect to the generated x-ray photons. 23
3.5 The microbunching process. 23
3.6 A schematic layout of the FLASH FEL in Hamburg. Figure adapted from [4]. 24
3.7 The cells of the TESLA cavity in FLASH. The system utilizes superfluid helium for RF module cooling. 26
3.8 FEL radiation in the temporal (left) and spectral (right) domains. Figure adapted from [5]. 28
3.9 The FLASH 1 FEL pulse structure, operating at a macropulse repetition frequency of $5Hz$. 29
3.10 Maximum electron energy versus minimum output wavelength for a non-exhaustive list of FEL facilities. 29
3.11 Emission spectra obtained for LPP sources based on the double gas puff target geometry. 31

4.1 Different ionization scenarios: when a NIR laser field irradiates a small quantum system (atom and/or molecule) it induces valence shell ionization. On the other hand a short wavelength FEL photon can access the core level electrons. 34
4.2 Sequential versus direct two photon double ionization (TPDI) processes for atoms irradiated by XUV or soft X-ray FEL photons. 36
4.3 Angular distributions for different β parameters ($\beta = -1, 0, 1, 2$) in two and three dimensions. 38
4.4 A schematic representation of the two-photon double-ionization scenario. 39
4.5 Angular distributions for different combinations of β_2 ($\beta_2 = 0, 1$) and β_4 ($\beta_2 = -1, 0, 1, 2$) parameters. 39
4.6 Partial energy level diagram corresponding to the conditions chosen in our experiment. In that case, a 4p electron departs at the first step and a 4s electron at the second step of the ionization process. 40
4.7 A simplified schematic diagram of the experimental setup in the CFEL-ASG Multi-purpose (CAMP) chamber. The angle-resolved spectra were recorded by means of a VMI spectrometer. Other important parts are the GMD detector, used to estimate the FEL intensity, and the gas jet via which the krypton is injected to the interaction region. . 41
4.8 (a) FEL pulse energy measurements acquired by means of the GMD detector. (b) Transmission curve of the nickel-coated KB mirrors. . . . 42

4.9 The raw VMI data (top left), the reconstructed image (top right), a 3D slice (bottom left) and the angular distribution (bottom right) for the sum of 100,000 single shot recordings. 43
4.11 The integrated angle averaged photoelectron signal as a function of the FEL intensity, for all five bins. 46
4.12 Angular distributions for the two open channels of the first step and for three different FEL intensities. 47
4.13 The extracted anisotropy parameters (β_2 and β_4) for the first step, as a function of the FEL intensity. 48
4.14 Angular distributions of the three channels open in the second step of the sequential process. 49
4.15 Anisotropy parameters for the open channels pertaining to the second step of the two-photon double ionization (a) The β_2 anisotropy parameter for three different FEL intensities. (b) The β_4 anisotropy parameter for the same three FEL intensities. 51

5.1 A schematic representation of the molecular potential for a diatomic molecule together with the corresponding K-shell x-ray absorption spectrum. 55
5.2 Possible dissociation processes following core hole creation in a triatomic molecule composed of three different atomic species. 56
5.3 (a) Schematic diagram of the setup. The laser beam is focused onto the double stream gas puff target to generate soft X-ray radiation. The emitted radiation is then used to perform absorption measurements on a molecular gas target located at a distance (D) away from the source. (b) Photographs of the experimental setup. 58
5.4 The time duration of the laser pulse. Assuming a Gaussian profile, the duration is estimated to be $\simeq 1.6\ ns$. 59
5.5 Emission spectrum including the spectral region between carbon and oxygen K-edge, for Kr and Kr/Xe (90/10) mixtures in the double stream gas puff source 60
5.6 A Harada type grating, used in the home-made spectrograph in our setup. Atomic (Ne) and molecular gases (SF_6) were used to perform the wavelength calibration. 60
5.7 (a) Soft X-ray emission spectrum of the $N_2 : O_2 : Ar\ (1:1:1)$ gas mixture. (b) the calibration curve of the spectrometer. 61
5.8 Soft X-ray emission spectrum of Ne and SF_6. 62
5.9 Experimental SXR absorption of the 'not ionized' (a) carbon dioxide and (b) methane plotted together with the normalized oscillator strength adapted from [6]. A gas mixture of xenon/krypton (90/10) was used as the medium to generate the soft X-ray radiation. 63

5.10 Absorption measurements in the vicinity of the carbon K-edge in CO_2 for three distances between the sample gas and the LPP soft X-ray source (a) using the Kr/Xe mixture and (b) using Kr in the double stream gas puff target. Corresponding spectra for methane (c) using the Kr/Xe mixture as the inner gas and (d) using Kr as the inner gas, in the double stream gas puff target. 64
5.11 Experimental SXR absorption spectra of the neutral or 'not ionized' (a) carbon dioxide and (b) methane, in the vicinity of the carbon K-edge plotted together with the normalized oscillator strength adapted from [6]. In addition, the corresponding SXR absorption spectra for a distance $D = 2\ mm$ between the sample gas and the LPP soft X-ray source are shown. A gas mixture of xenon/krypton (90/10) was used as the medium to generate the soft X-ray radiation. 67
5.12 Photoabsorption spectrum of the 'not ionized' or neutral CO_2 sample gas in the oxygen K-edge spectral region, shown together with the oscillator strength for the carbon dioxide molecule. Krypton gas was used in the soft X-ray source. 68
5.13 Absorption spectra in the vicinity of the oxygen K-edge in CO_2 for three different distances with respect to the LPP soft X-ray source (a) using Kr and (b) using the Kr/Xe mixture in the double stream gas puff target. 69
5.14 Absorption spectrum of CO_2 in the vicinity of the oxygen K-edge for a distance of 2 mm with respect to the LPP soft X-ray source using the Kr/Xe mixture, plotted together with Cowan code calculations [7, 8] for the O, O^+ and O^{2+} species. In addition, oscillator strength data of the CO molecule acquired from the Gas Phase Core Excitation Database are shown [6]. The spectral features in the low photon energy region of the photoabsorption spectrum of the ionized carbon dioxide plasma can be attributed to these species. 70

6.1 Evolution of the shortest attainable pulse duration over the passage of time. 73
6.2 Characteristic timescales of the most fundamental physical processes observed when molecules are irradiated by ultrashort laser pulses. . . 74
6.3 A three-dimensional representation of the experimental setup, together with a schematic of the TOF spectrometer. 76
6.4 TOF spectrum in the region of the Xe isotopes, used for the calibration of the spectrometer. 76
6.5 Experimental points together with SIMION simulations and the fit curve used for calibration of the spectrometer. 77
6.6 Second harmonic generation by means of a Type I Barium Borate (BBO) crystal. 78

6.7 Ion TOF spectra as a function of the laser intensity for dissociation of methane irradiated by 800 nm laser pulses. 80
6.8 Ion TOF spectra as a function of the laser intensity for dissociation of methane irradiated by 400 nm laser pulses. 81
6.9 Ion yields as a function of the laser intensity for dissociation of methane irradiated by (a) 800 nm and (b) the second harmonic of the fundamental wavelength at 400nm laser pulses. 82
6.10 Ion TOF spectra for a set of higher laser intensities ranging from 4 10^{14} W/cm^2 to 7 10^{14} W/cm^2. The upper panel (a) corresponds to the fragmentation of methane induced by the 800 nm laser field, whereas the bottom panel (b) refers to the fragmentation of the same molecule irradiated by the second harmonic field at a wavelength of 400 nm. . . 84
6.11 The same TOF spectra as in Figure 6.10 focused on the H^+ fragments. In that case we observe a forward - backward peak structure for both 800 nm and 400 nm laser fields. When the fundamental laser field at 800 nm is concerned, we observe three pairs of forward - backward peaks, as a result of the Coulomb explosion of unstable doubly charged ions (CH_4^{2+}, CH_3^{2+}, CH_2^{2+}, CH^{2+}). The same is true for the second harmonic field, where in addition to the central peak that was observed at lower intensities, one extra forward - backward component appears. 85
6.12 The same TOF spectra as in Figure 6.10 focused on the H_2^+, CH_4^{2+} and CH_2^{2+} fragments that were not present in the spectra for lower laser intensities. As can be seen for 800 nm laser pulses, the H_2^+ signal exhibits a forward - backward peak structure in addition to the central peak. This structure is indicative of two different contributions to the H_2^+ fragments : the forward - backward components represent fragments with high kinetic energies coming from Coulomb explosion processes, whereas the central peak is indicative of H_2^+ fragments with a thermal energy distribution that can emerge from a stepwise process. In the case of the second harmonic laser field, only fragments with negligible kinetic energies are present in the TOF spectrum. This leads us to exclude any Coulomb explosion channels that would result in the H_2^+ fragments. 86
6.13 Ponderomotive energy acquired by the free electrons in the laser field for the range of laser intensities involved in our experiment. The horizontal black line corresponds to the minimum energy required for double ionization of neutral methane precursor. 87

A.1 The main parts of a VMI spectrometer. 91
A.2 The four main steps of the VMI technique. 92

B.1 Timing scheme of the double stream gas puff target. 94

B.2 Integrated spectral intensities, for different set of time delays in the case of krypton (inner gas) and helium (outer gas) gases. 94

List of Tables

2.1 Tabulated values of the refractive index and the Pockels coefficient for two electro-optic media. The calculated half wave voltage values are tabulated for two laser wavelengths (1064 and 532 nm). 7

4.1 Atomic photo-ionization for different photon energies. 35
4.2 Anisotropy parameters for the $^2P_{3/2}$ component of the first ionization step. 47
4.3 Anisotropy parameters for the $^2P_{1/2}$ component of the first ionization step. 47
4.4 Anisotropy parameters for the $^3P_2$ component of the second ionization step. 50
4.5 Anisotropy parameters for the combination of $^2P_{1/2} \longrightarrow {}^3P_{1,0}$ / $^2P_{3/2} \longrightarrow {}^3P_2$ components of the second ionization step. 50
4.6 Anisotropy parameters for the $^2P_{3/2} \longrightarrow {}^3P_{1,0}$ component of the second ionization step. 50

5.1 Tabulated main technical characteristics of the spectrometer grating . 58
5.2 Tabulated optimum experimental parameters 59
5.3 Tabulated transitions for the CO_2 and CH_4 plasmas, including transitions in CH_3^+, CO, C, C^+ species. 66
5.4 Tabulated transitions for the CO_2 plasma, including transitions in O, O^+, O^{2+} species. 71

Dedicated to my Family

Chapter 1

Introduction

The interaction of intense laser light with matter gives rise to a plethora of fascinating observations pertaining to physical and life sciences. Specifically, the double slit experiment performed by Thomas Young in 1802 provided evidence regarding the wave nature of light. Observation of the photoelectric effect by Heinrich Hertz in 1887 [9] and the subsequent explanation of this effect by Albert Einstein in 1905 [10], confirmed the particle nature of light. The answer to the conundrum regarding the nature of light (wave or particle representation) was given by Louis de Broglie who introduced wave-particle duality in 1923. These, together with other important landmarks such as Compton's scattering experiment [11], the formulation of Schrödinger's equation [12], Heisenberg's uncertainty principle [13] and many more, laid the foundations for further investigations on light-matter interactions. Hence, processes such as valence and inner shell photoionization of atoms, photoinduced breaking or making of interatomic bonds in molecules and the evolution of sub-cellular structures in biological objects have been, and still remain, in the spotlight of current research investigations into light matter interactions. Besides the deep understanding of light and interactions arising from fundamental research, understanding of light matter interactions has been beneficial to technologically-oriented research and its applications.

More specifically, in materials science extreme-UV lithography in the 11-14 nm range, provides improved resolution required for production of more-advanced integrated circuits [14]. In addition, laser induced breakdown spectroscopy (LIBS) is used for simultaneous multi-element analysis in materials [15]. In the field of biology, soft X-ray laser microscopy [16] and coherent diffraction imaging (CDI) [17] allow for structural studies with increased resolution in various specimens. One other application involves the investigation of the four 'areas' of environment (air, water, land, space) by means of the Light Detection And Ranging (LiDAR) remote sensing technique [18]. From this non-exhaustive list of applications, it can be seen that laser matter interactions are relevant to a manifold research fields.

In order to induce such interactions, different types of laser sources have been developed. Importantly, the combination of output parameters of the source (e.g.,

wavelength, brightness, pulse duration, etc.) define the nature of the experimental study. For example when short wavelength radiation in the extreme ultraviolet (XUV) to soft X-ray (SXR) range is used, inner shell electrons become accessible. On the other hand, investigations of the valence shell electrons are carried out by means of radiation in the visible and/or near infrared (NIR) range. In the latter case, the photoionization process is sensitive to the chemical bonding of each atom, since the valence electrons act as a glue to form the interatomic bonds. On the other hand, in the case of XUV and SXR sources, the photoabsorption process is site-specific, although small chemical shifts due to the coordination environment may be present in the spectrum. From a different point of view, short wavelength radiation is required for microscopy applications as it offers increased spatial resolution, whereas short pulse duration is a favorable characteristic in time resolved studies of dynamical processes.

The aforementioned examples highlight how insight into different aspects of the same physical process can be gained by careful selection of the source parameters and how the output characteristics of the source determine its suitability for a particular experiment. As a part of this doctoral training process, three different light sources were used to perform spectroscopic investigations on small quantum systems such as atoms (Kr) and small molecules (CO_2, CH_4). These systems are important fundamental quantum entities and a thorough understanding of their nature paves the way for similar studies of more complex quantum systems.

This doctoral thesis consists of two discrete parts. The first part (chapter 2 and chapter 3) contains an extensive description of the laser sources used in the work which is then described in the second part (chapter 4, chapter 5 and chapter 6) which deals with the experimental results.

In chapter 2 we introduce the background theory and techniques used to generate laser radiation in the visible and near infrared part of the spectrum. Within this context, we describe the principles of operation for two solid state table-top sources, namely the Ti:sapphire and the Nd:YAG lasers.

Chapter 3 is concerned with the development of sources in the vacuum UV and soft X-ray spectral range. Here, the historical framework of the synchrotron is used as a prelude to its successor, the free electron laser (FEL). A detailed description of the FELs is presented, in order to illustrate the characteristics of the output radiation. An alternative to the large scale facilities such as synchrotrons and FELs namely, the laser produced plasma (LPP) source is introduced. Specifically, a double stream gas puff target scheme is used to successfully cover the soft X-ray spectral range.

In chapter 4 we report a photoionization study in krypton irradiated by intense FEL pulses in the vacuum-UV (VUV) spectral range. Angle-resolved photoelectron spectroscopy (ARPES) is applied to investigate the effect of FEL intensity on the angular

distributions of the photoelectrons, emitted upon near threshold double ionization of Kr.

Chapter 5 is dedicated to soft X-ray photoabsorption measurements in photoionized molecular plasmas. For the sake of these investigations, photons delivered by a LPP source were used to create and probe both ionized and neutral carbon dioxide and methane. Photoabsorption measurements were made around the carbon and oxygen K-edges. Striking differences were observed between the neutral, i.e., 'not ionized', and the ionized molecular gases. Our findings underline the role of molecular dissociation in the latter case, as signatures of atomic and molecular fragments were identified in the photoabsorption spectra.

Chapter 6 is concerned with the fragmentation of CH_4 molecules in the presence of intense laser fields generated by a table-top laser system. The fundamental wavelength (800 nm) and its second harmonic (400 nm) were used to drive fragmentation upon photoionization of one or two valence electrons. Ion spectroscopy was applied to identify the fragmentation pathways.

Chapter 2

Sources in the NIR region

2.1 Historical background

The word Laser is an acronym for Light Amplification by Stimulated Emission of Radiation. As will become clear later in that chapter, it is the physical process of stimulated emission, discovered by Einstein in 1916 [19], that lies at the core of the laser operation. The first operating laser was constructed in 1960 by T.H. Maiman [20]. This pioneering design incorporated a Ruby ($Cr^{3+} : Al_2O_3$) rod as a gain medium, and it could thus be classified as a solid state laser. Several months later, following an alternative design by A. Javan, W.Bennet and D.Harriot [21], the gain medium consisted of a mixture of helium and neon atoms excited by an electric discharge. In this way, the first gas laser, namely the He-Ne laser was developed. With the passage of time, laser technology has progressed decisively. As a result, shorter pulse durations on the order of nanoseconds were achieved by means of the Q switching technique (e.g., [22]). An important step towards further shortening pulse duration was made via the mode-locking technique [23]. The minimum pulse duration of a mode-locked system is then achieved by means of chirped pulse amplification (CPA) technique [24]. As a matter of fact, nowadays ultrashort pulses in the femtosecond regime (see review article [25]), are commercially available.

Since their invention, lasers have played a catalytic role in the field of atomic and molecular physics. This has indeed been emphasized by the Nobel prizes awarded to researchers in the field of laser technology. In particular, C.H. Townes, N.G. Basov and A.M. Prokhorov were awarded the Nobel prize in 1964 "for fundamental work in the field of quantum electronics, which has led to the construction of oscillators and amplifiers based on the maser-laser principle". More recently, in 2018 Gérard Mourou and Donna Strickland were awarded the Nobel prize "for their method of generating high-intensity, ultra-short optical pulses" [26].

In a first approach, the laser consists of a gain medium (an amplifier) placed within an optical cavity. This arrangement, is essentially a loop with a positive feedback to form what is defined as an optical oscillator. The net gain of the amplifier must be larger than unity in order to overcome any losses in the cavity, including the external

coupling. In addition, the change in phase, induced by the feedback loop should be equal to $n \times 2\pi$, where $n = 0, 1, 2, ...$ in order to ensure a constructive interference between the input and amplified (output) signals. The latter condition imposes a set of resonant frequencies supported by the cavity. Furthermore, work by Schawlow and Townes [27], Basov and Prokhorov [28] showed that the number of resonant frequencies in an optical resonator could be reduced by confinement of light in only one dimension leading to a set of longitudinal modes only. The amplification process is then achieved by stimulated emission from an ensemble of atoms/molecules. This is only possible in the case of a transition for which inversion of populations holds between the upper and the lower levels.

2.2 The 'fast' regime

Generation of pulses in the nanosecond regime, sometimes termed the 'fast' regime, is achieved by means of the so-called Q switching technique [22]. In that case, the quality factor (Q) is used to describe the losses of the laser resonator. A high Q factor is indicative of a low-loss cavity, whereas a low Q factor is representative of a lossy laser cavity (i.e. the cavity Q is low). Thus, the Q switching technique involves an abrupt change of the Q factor, from a low to a high value. The main stages of the Q switching technique may be described as follows: Initially, pumping of the active medium begins while the cavity losses are high enough to prevent lasing inside the cavity. Provided that the lifetime of the upper laser level is long enough, energy is stored by the active medium and the amplifier gain increases. Suddenly, one switches to a high Q factor by reducing the loss of the cavity. Now the lasing action evolves quickly since the energy stored in the active medium is extracted by stimulated emission. Thus a very intense laser pulse is generated within several nanoseconds before the amplifier gain gets depleted. The aforementioned process is schematically depicted in Figure 2.1.

Out of many solid state materials, $Nd : YAG$ is probably the most commonly used

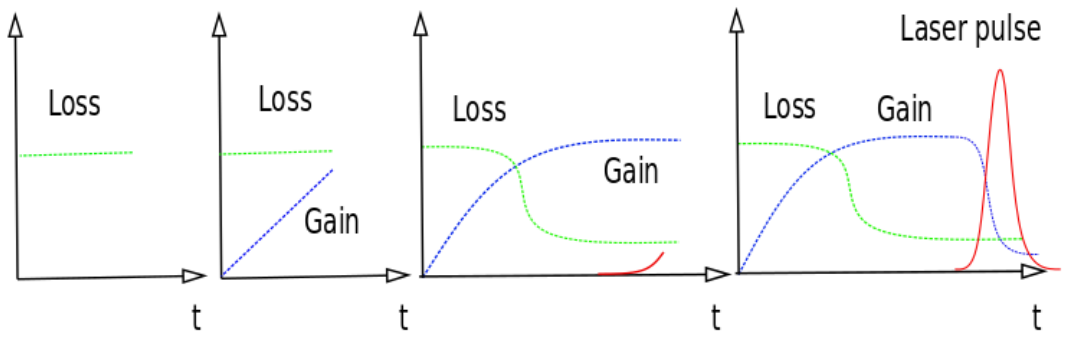

Figure 2.1: The main stages of the Q-switching process for the generation of 'fast' laser pulses in the nanosecond regime.

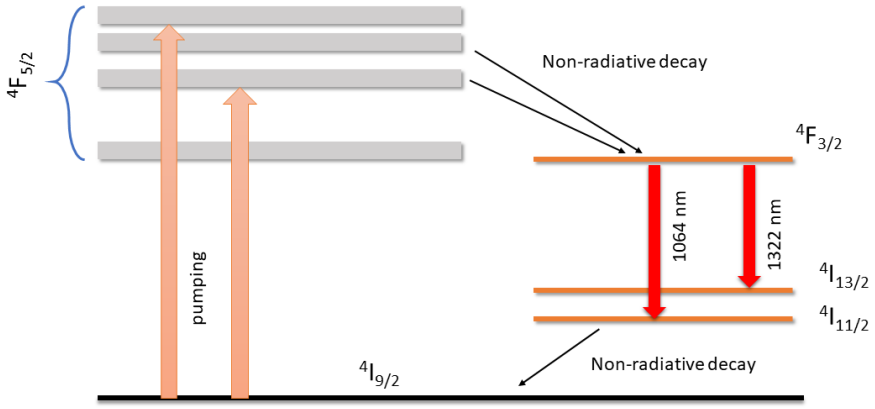

Figure 2.2: Energy band diagram for the Nd:YAG active medium. It represents a four level system in which the $^4F_{3/2} \longrightarrow^4 I_{11/2}$ and the $^4F_{3/2} \longrightarrow^4 I_{13/2}$ transitions result in laser emission at 1064 nm and 1322 nm respectively.

as a laser medium. The energy levels of the Nd^{3+} ions are split into manifolds in the presence of the YAG crystal field allowing for broad pump (energy) bands to be formed (see Figure 2.2). Making use of Xe flash lamps, a strong pumping band at around 810 nm can be exploited to populate the $^4F_{5/2}$ manifold from the ground state $^4I_{9/2}$. Then a rapid radiationless decay leaves the system in the upper laser level $^4F_{3/2}$. The lifetime (230 μs) of this upper laser level is long enough to ensure that a population inversion can be achieved. The laser transition to the $^4I_{11/2}$ and $^4I_{13/2}$ components of the ^4I manifold result in laser emission at 1064 nm and 1322 nm respectively. The final step in this four level system is a rapid non radiative transition to the ground state. The $Nd:YAG$ medium has a high thermal conductivity thus it is able to support repetition rates up to 1 KHz [29].

Out of several possible alternatives (Kerr cell, acousto-optic shutter, saturable absorber), our system, NL129 (EKSPLA), makes use of an electro-optic shutter in order to achieve Q switching. The so called Pockels cell, named after German physicist F. C. A. Pockels, is a crystal that becomes birefringent when an electric field is applied to it. Thus, it induces a polarization rotation on the laser beam which is proportional to the thickness of the cell and the magnitude of the applied voltage. Assuming a fixed thickness of the cell, one can adjust the voltage so that the polarization rotation is 45 degrees when the voltage is 'on' and zero degrees when the voltage is 'off'. The former arrangement results in high cavity losses, whereas the latter offers a cavity with low loss. As a result, the voltage 'ramp' acts as a switch for the cavity losses with respect to time.

Table 2.1: Tabulated values of the refractive index and the Pockels coefficient for two electro-optic media. The calculated half wave voltage values are tabulated for two laser wavelengths (1064 and 532 nm).

material	n	r ($\times 10^{-12} m/V$)	V_π (kV) $\lambda = 1064nm$	V_π (kV) $\lambda = 532nm$
KDP	1.507	10.6	14.7	7.3
ADP	1.520	8.5	17.8	8.9

For a weak variation of the refractive index of an electro-optic medium with respect to the applied field it can be expanded in a Taylor series around E=0

$$n(E) = n + a_1 * E + \frac{1}{2} a_2 * E^2 + \dots \tag{2.1}$$

If we now introduce the Pockels coefficient defined as $r = -\frac{a_1}{n^3}$ and neglect terms of third or higher order we get

$$n(E) \approx n - \frac{1}{2} r n^3 E \tag{2.2}$$

When a laser beam propagates though a Pockels cell of length L, it acquires a phase shift $\phi = n(E)\frac{2\pi L}{\lambda}$, where λ is the wavelength of the incident beam. After substituting the relation for n(E) we get

$$\phi \approx \phi_0 - \frac{2\pi r n^3 E L}{\lambda} \tag{2.3}$$

where $\phi_0 = \frac{2\pi n L}{\lambda}$. The electric field can be obtained by applying a voltage V across the longitudinal or the transverse direction as seen in Figure 2.3. Then $E = \frac{V}{d}$ and we can write

$$\phi \approx \phi_0 - \pi \frac{V}{V_\pi} \tag{2.4}$$

where $V_\pi = \frac{d}{L}\frac{\lambda}{2rn^3}$ is the half wave voltage, which is the voltage needed to induce a phase shift of π. For the longitudinal case ($d = L$) one gets half wave voltage values of several kilovolts, whereas in the case of transverse arrangement where $d \ll L$ half wave voltages of several volts to several hundred volts are encountered. In Table 2.1 we summarize the half wave voltage values in the longitudinal case, for two commonly used materials, namely the potassium dihydrogen phosphate (KDP) and the ammonium dihydrogen phosphate (ADP). The half wave voltage values are calculated for two different laser wavelengths (1064 and 532 nm) that are common for $Nd:YAG$ laser systems.

A schematic diagram of a typical Flashlamp-pumped, Q-switched ND:YAG laser system is shown in Figure 2.4. The main components include: a pair of mirrors (Rear, Output), the Flashlamps, the pump cavity and the Pockels cell, required for the Q-switching process.

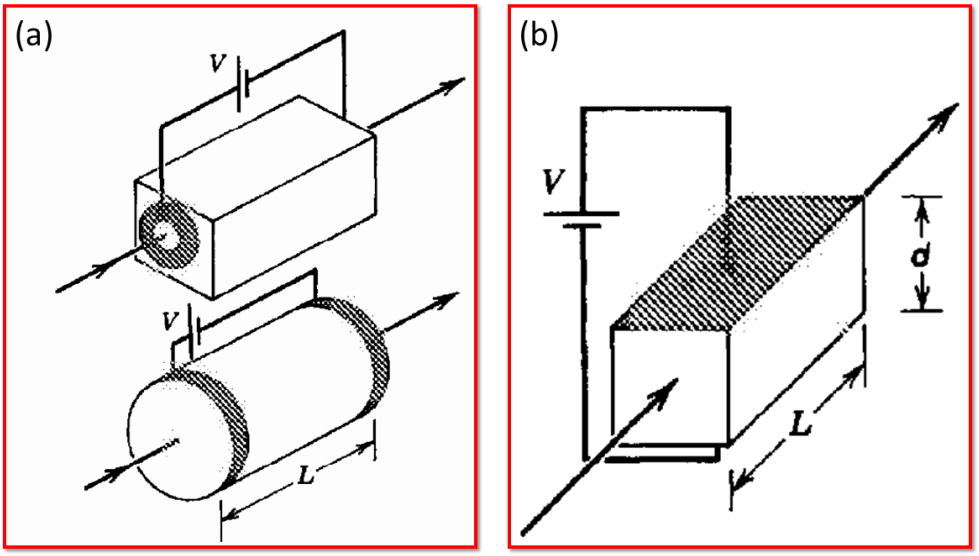

Figure 2.3: (a) Longitudinal and (b) transverse arrangement of a Pockels cell. Figures adapted from reference [30].

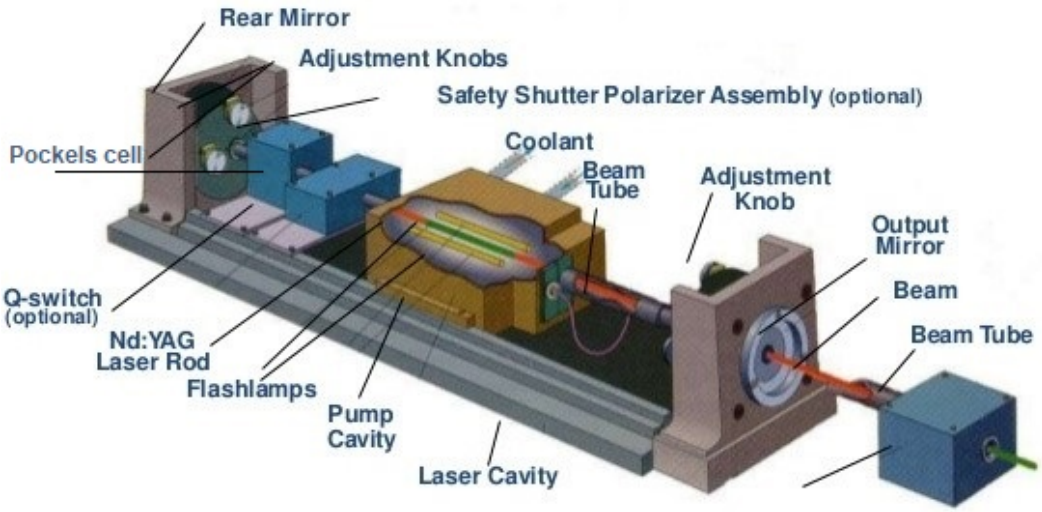

Figure 2.4: A typical Flashlamp-pumped, Q-switched Nd:YAG laser system [1].

2.3 The 'ultrafast' regime

The so called mode locking technique is required in order to generate really short pulses on the order of femtoseconds (see textbook [31]). This approach is based on coupling together the longitudinal modes and locking the relative phases between them together. In the case of the $Ti : Sapphire$ laser system a self locking mechanism is possible as we will see later [23]. For now we focus on the main parts of an ultrafast laser system which are: the oscillator, the stretcher, the amplifier and the compressor.

2.4 The oscillator

The oscillator generates the train of ultrashort pulses which will subsequently be amplified. The active medium is a titanium-doped aluminum oxide ($Ti : Al_2O_3$, Ti:Sapphire) crystal. The potential of this active medium was demonstrated for the first time by P.F Moulton in 1986 [32]. Ti:Sapphire exhibits a very broadband gain bandwidth ($680 - 800nm$), high thermal conductivity and high energy storage density.

The energy level diagram of the Ti^{3+} ions is presented in Figure 2.5a. The Ti^{3+} ion has a single electron in its outer 3d subshell. In the presence of the octahedral electric field of the crystal the $3d$ level splits into a twofold degenerate, spin doublet $^2T_{2g}$ state and a twofold degenerate, spin doublet ^2E_g. Excitation from the lowest vibronic levels of the $^2T_{2g}$ energy state to several vibronic levels of the excited ^2E_g takes place via optical pumping. For this reason the second harmonic ($527nm$, $4.5W$) by a Verdi-18 Nd:YLF laser [33] is used to pump the Ti:Sapphire system (or alternatively the second harmonic of an $Nd : YAG$ Laser). As can be seen in Figure 2.5b, the absorption spectrum of the Ti:Sapphire crystal exhibits a strong absorption peak in the region around 500 nm. The second harmonic generation occurs in an LBO (LiB_3O_5) crystal inside the Verdi cavity.

Then, a very rapid non radiative relaxation to the lowest vibronic state of ^2E_g takes place. The long lifetime (about $3.2\mu s$) of this state ensures efficient inversion of population. The laser transition occurs from the ground vibronic state ^2E_g to excited vibronic states $^2T_{2g}$ leading to laser emission which peaks around 750 nm and has a broad bandwidth, on the order of several tens of nanometers. The final step of this four level system includes a rapid non radiative relaxation to the lowest vibronic state of $^2T_{2g}$.

A schematic representation of an indicative oscillator cavity (Coherent $Micra^{TM}$ series) can be seen in Figure 2.6. The aforementioned broad gain bandwidth implies that there are several modes oscillating inside the cavity. The steady state laser operation demands that the electric field must repeat itself after a cavity round trip. This limits the number of frequencies supported by the oscillator cavity as stated earlier.

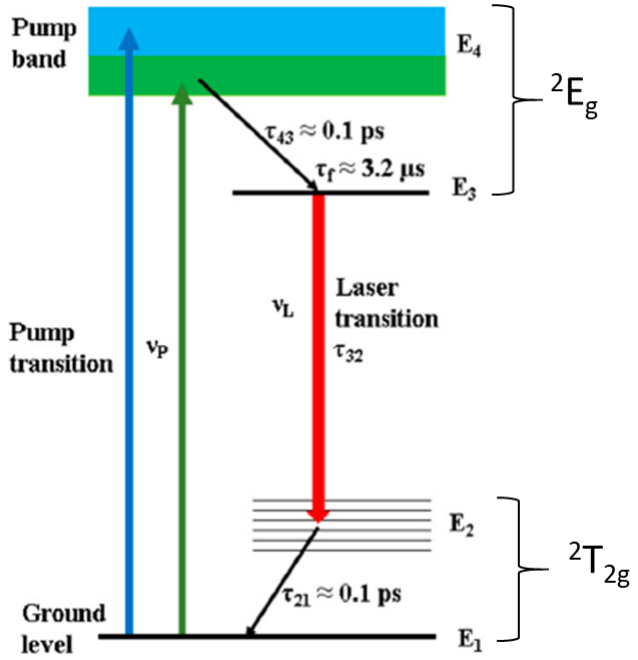

(a)

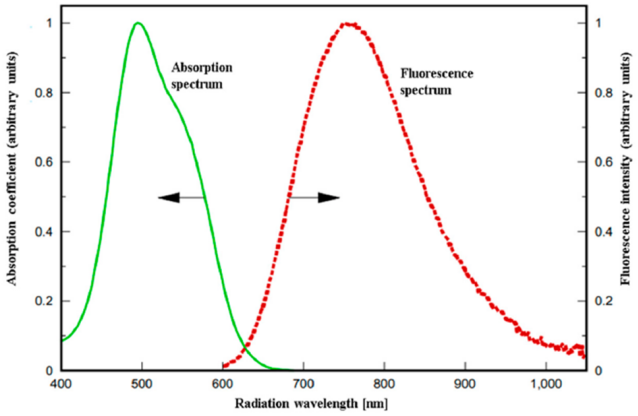

(b)

Figure 2.5: (a) Energy level diagram for the Ti:Sapphire crystal used as the active medium for generation of ultrafast pulses (b) Absorption and emission spectra for the Ti:Sapphire crystal. Figures adapted from reference [34].

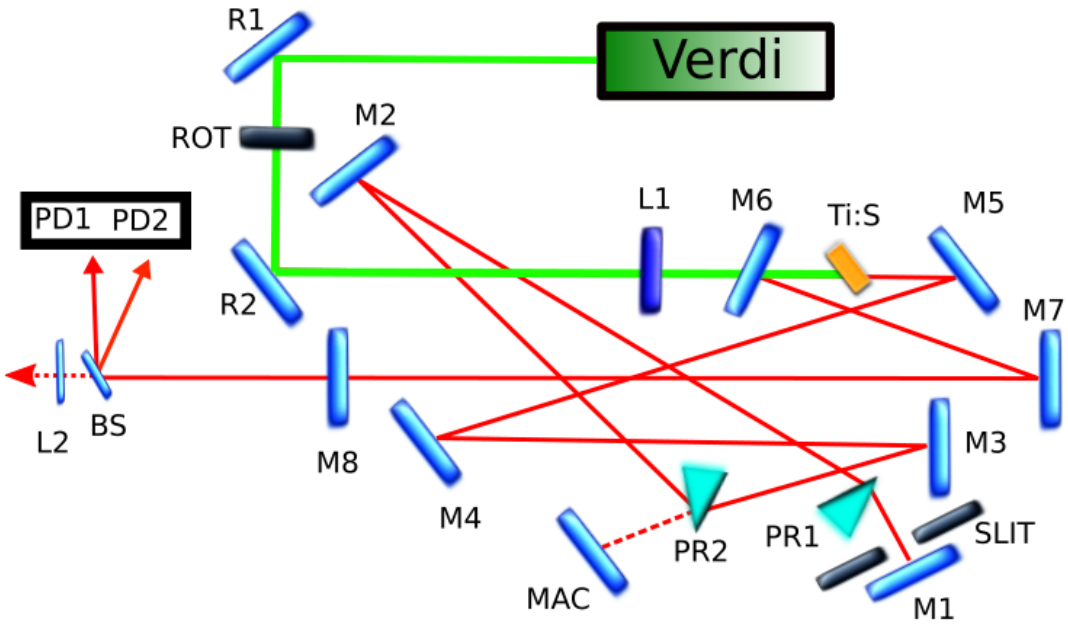

Figure 2.6: A representative oscillator cavity (Coherent Micra^{TM} series) [2]. The green Coherent Verdi^{TM} pump laser beam is directed towards the Ti:Sapphire crystal by a set of mirrors (R1, R2) while a polarizer (ROT) is placed between them. A lens (L1) is then used to focus the green beam in order to ensure that a population inversion is induced in the active medium (Ti:S). Subsequently, the generated red beam travels around a 'ring' cavity, formed by eight mirrors (M1-M8) before leaving the oscillator, while MAC is an auxiliary cavity end mirror. A pair of prisms (PR1, PR2) is used to compensate for the pulse broadening. After mirror M8 the beam passes through a beamsplitter (BS) where the reflected beam is directed towards two photodiodes (PD1, PD2) and the transmitted beam encounters a collimating lens (L2).

The so called longitudinal modes satisfy the condition:

$$\nu = \frac{n \times c}{2 \times l} \tag{2.5}$$

Where c is the speed of light, l is the optical path of the "ring" cavity, determined by the end mirrors M1, M8 and n is an integer.

Production of ultrashort pulses requires multiple mode (longitudinal) operation, since a broad spectral bandwidth is necessary to support a temporally short pulse. When the relative mode-phases are random (CW operation), the output intensity periodically fluctuates about an average value. The situation is completely different when the relative mode-phases are fixed. In this scenario, the oscillator produces a series of intense, ultrashort pulses. This behavior can be perceived as a case of constructive interference between the different modes. The period after which the lasing effect is repeated equals the cavity round trip time and it is given by

$$T = \frac{2l}{c} \tag{2.6}$$

The typical optical path l for an oscillator is roughly two meters, which results in a cavity round trip time of $12ns$ and a high repetition rate of $80MHz$. The technique applied to fix the relative mode phases is the well established optical mode locking process. More specifically, our system makes use of the Kerr Lens Mode-locking (KLM). This technique was first demonstrated early in the 90's [35] and is based on the optical Kerr effect. According to this effect, when the intense laser field (pulsed radiation) propagates through a non-linear material (which in our case is Ti:Sapphire), it induces an intensity-dependent contribution to the refractive index of the material. Since intensity varies in time but also radially, the field acquires a phase shift, which is both radially dependent as well as time dependent. This phase shift is only present in the pulsed operation. On the other hand, the continuous wave is not intense enough to induce this non-linear effect. Thus, the radial dependence of the refractive index leads to a lensing effect, which in turn reduces the pulsed beam diameter.

In the soft aperture mode locking scheme, the pulsed beam is co-linear with the pump beam but not in the case of the cw mode. This arrangement, combined with the aforementioned focusing effect results in a better overlap of the pulsed radiation with the spatial profile of the pump beam in the Ti:Sapphire crystal. Thus, there is a gain discrimination between the pulsed radiation and the cw mode. The mode locking process is triggered by a small variation of the cavity optical path. In this specific oscillator design, it is the movement of the mirror M4 that initiates the mode locking process. Once the mode locking process starts, it is self-maintained.

As the laser pulse propagates inside the oscillator cavity, it undergoes broadening caused by two different effects. First, the pulse is affected by self phase modulation (SPM). As mentioned above the refractive index of the active medium is time dependent. This effect, by its nature introduces additional frequency components. The pulse is further broadened by group velocity dispersion (GVD) induced by the optical elements of the cavity. More to the point, all materials exhibit a non linear dependence of their refractive index with respect to the wavelength. This means that the different wavelengths included in the pulse will propagate with different velocities inside a dispersive material. This non uniformity is the chirp of the pulse. In our case the red components of the pulse move faster than the blue components, leading to a "positively chirped " pulse. The two contributions (SPM) and (GVD) add-up to broaden the pulse. In order to compensate for this broadening, a pair of prisms (PR1, PR2) is present inside the cavity. In that case, the two prisms are arranged in a folded geometry to introduce negative GVD in order to counterbalance the positive GVD introduced by the laser medium. Also it is worth mentioning, that the central wavelength of the pulse can be slightly tuned by adjusting the slit in front of M1.

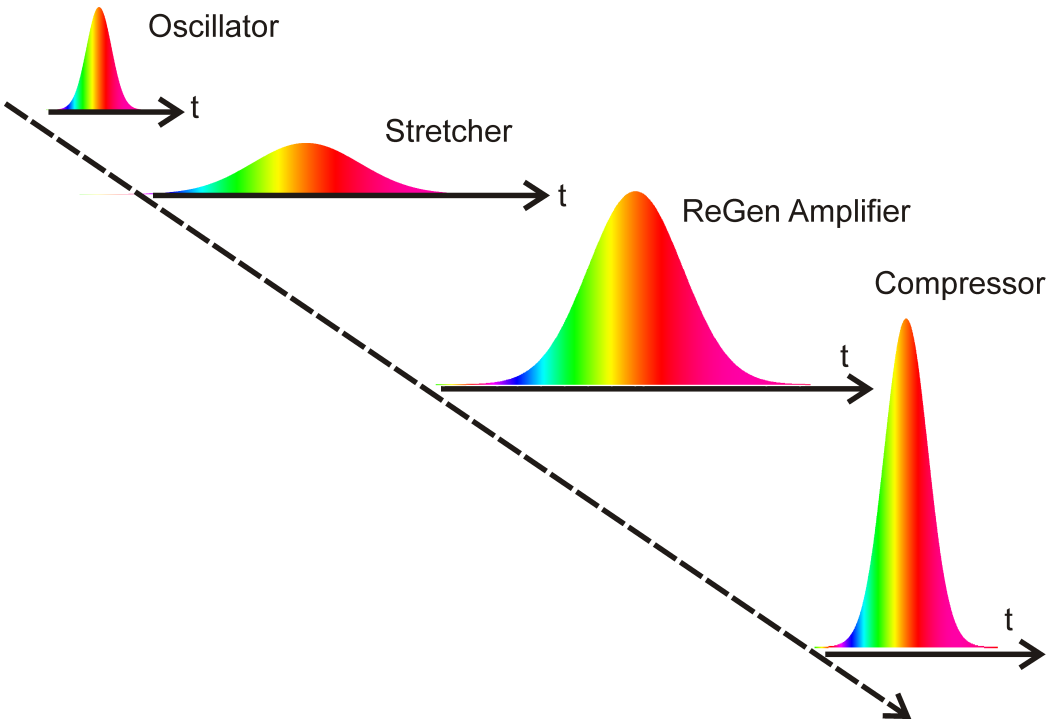

Figure 2.7: The main stages (oscillator, stretcher, amplifier, compressor) of the CPA technique used to generate ultrashort laser pulses.

2.5 The chirped pulse amplification (CPA) technique

While the output pulse of the oscillator is short enough ($\sim 30fs$), the output power is still low ($\sim 350mW$) meaning that an amplification stage is required. However, the direct amplification of the short pulses delivered by the oscillator is not viable. The reason is that the peak intensity induced by the amplified pulse would surpass the damage threshold of the active medium. In order to overcome this difficulty the Chirped Pulse Amplification (CPA) technique was developed [24]. The outline of this scheme is depicted in Figure 2.7 and can be described as follows: Initially ultra-short, intense pulses are generated in the oscillator. Subsequently, these pulses are directed to the stretcher where they are broadened in time. Then the temporally broadened pulses can be introduced into the amplifier without risk of damage to the active medium. Finally, following amplification, the pulses are temporally compressed back to their initial duration.

2.6 The stretcher

A schematic representation of the stretcher is given in Figure 2.8. The input beam is incident on the diffraction grating (SG). The laser beam falls in the grating at the Littrow angle, meaning that the angle of incidence equals the angle of diffraction. Then, the beam hits mirrors SM6 and SM7 and it is directed again towards SG. After being diffracted, the beam encounters the retro reflectors (SM8, SM9) and once again is incident on the grating. This path is repeated several times before the beam is

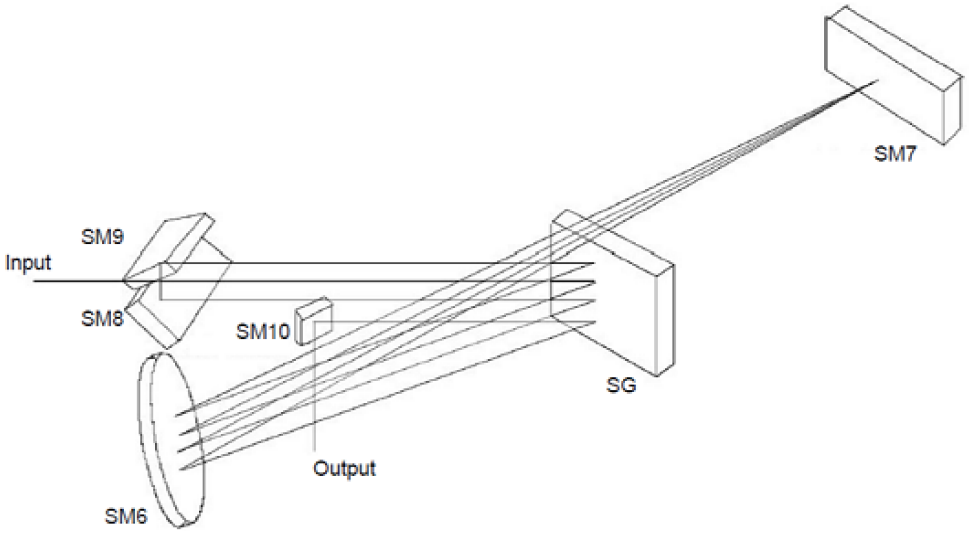

Figure 2.8: A single grating stretcher [3]. This geometry includes a grating (SG) and 5 mirrors (SM6, SM7, SM8, SM9, SM10) to induce a linear positive chirp to the pulse [3].

ejected from the stretcher by means of the pickoff mirror (SM10). This design makes use of a single grating to spatially disperse the different frequencies contained in the laser pulse. Thus, every frequency component travels an optical path of different length. The stretcher introduces a group velocity dispersion (GVD), which induces a linear positive chirp to the pulse. The GVD causes a spectral de-phasing of the pulse without affecting its spectral amplitude. Any higher order contributions (third-order dispersion etc.) are not desirable because the re-compression becomes difficult to achieve.

2.7 The regenerative amplifier (RGA)

After the pulse is broadened, the next step is the amplification process. Two types of amplifiers have been developed, namely the multi-pass and the regenerative amplifiers. In the first design, the beam passes through the medium several times as it is implied by the amplifier's name. The different cavity trips, which range from 4 to 8, are geometrically separated. This feature does not allow for the multi-pass design to be considered a resonator. On the other hand, the regenerative amplification scheme is based on a pulse which remains trapped inside the amplifier cavity. Now, the laser pulse makes more passes through the medium ($\sim$ 20 round-trips) and when it accumulates enough energy, it is ejected out of the cavity.

The amplifier in DCU (Coherent Legend USP HE 1K) makes use of the regenerative technique. A schematic diagram of the set-up of this amplifier is presented in Figure 2.9. The $Ti : Sapphire$ crystal is pumped by a Coherent Evolution $Nd : YLF$ laser ($527nm, 100ns, 19W$) which is externally cooled at $-10^{\circ}C$ to avoid thermal damage. The S-polarized seed beam comes from the stretcher and it is reflected off the

Ti : Sapphire rod towards the mirror M1. The laser beam then passes through a quarter wave plate and a Pockels cell denoted as PC1. No voltage is applied to the Pockels cell, so that the pulse is only affected by the $\lambda/4$ plate and becomes circularly polarized. After the pulse is reflected by mirror M2 it passes again through the $\lambda/4$ plate and is now P-polarised. The perpendicularly polarised pulse passes through the active medium and it is subsequently reflected off the other two mirrors M3, M4. After a cavity round trip the pulse comes back to M1 for a second pass. Meanwhile a voltage is applied to Pockels cell PC1 which is now turned into a $\lambda/4$ plate, eliminating the effect of the static quarter wave plate. This traps the P-polarised pulse in the cavity. After $10-15$ passes, the pulse is intense enough to be ejected out of the cavity. The ejection process is rather simple: A $\lambda/4$ voltage is applied to the other Pockels cell (PC2) and the pulse becomes S-polarised after a double pass through the PC2. Finally the pulse is reflected out of the cavity by the rotating wave plate (RWP). The rotating wave plate reflects the S-polarized beam whereas it transmits the P-polarized beam.

One can infer that the amplification process demands a very accurate timing synchronization. As a matter of fact, the first Pockels cell PC1 must be synchronized to the seed pulse train. In order to do this, the PC1 is synchronized to the oscillator RF signal. For this to happen, the time delay between PC1 activation with respect to the seed pulse is adjustable. In addition a delay between the PC1 and PC2 activation times is required to ensure that the pulse gets ejected after a sufficient number of round trips. All the aforementioned processes are controlled by the synchronization and delay generator (SDG) module.

For an in-depth analysis of the amplifier, one should take into account two phenomena which are inherently related to the amplification process. The first is the so called amplified spontaneous emission (ASE) process. As mentioned above, the pump pulses are on the ns time-scale, much longer than the fs seed pulses. Consequently the medium remains inverted before and after the amplification process takes place. In parallel the medium de-excites by means of the spontaneous emission, which results in an isotropic light emission. Some of the emitted photons propagate in directions close to the optical axis of the gain medium. These photons are amplified in every passage through the active medium. Thus, ASE limits the available gain and results in a background signal. In order to prevent ASE, the regenerative amplifiers make use of low gain configurations. A second phenomenon is the so-called gain narrowing. When a pulse passes through the active medium, the wavelengths which are closest to the peak of the gain spectrum, undergo the strongest amplification. This fact eventually leads to narrowing of the pulse spectrum.

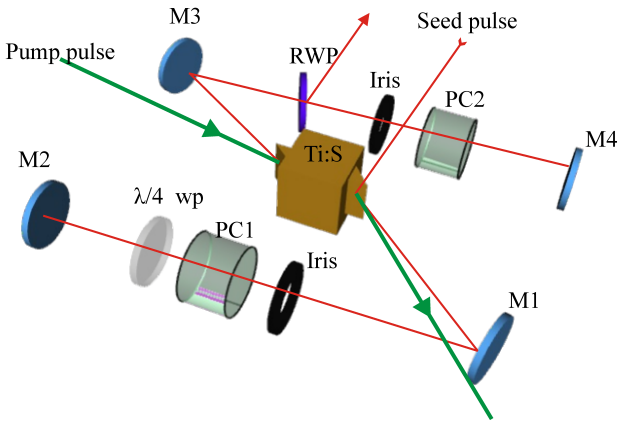

Figure 2.9: The regenerative amplifier [3]. Four mirrors (M1, M2, M3, M4) are used to form the laser cavity. Appropriate timing between two Pockels cells (PC1, PC2) ensures a sufficient number of roundtrips required for amplification. A rotating waveplate (RWP) is then used to eject the amplified laser pulse. Additional optical components include a quarter waveplate and two irises.

2.8 The compressor

The last step in the CPA technique is the compression process. The compressor acts to compensate for the chirp that the stretcher induces in the pulse, as well to minimize any dispersion effects caused by the amplifier. The optical layout of the compressor is similar to the stretcher (see Figure 2.8). This arrangement makes use of a single grating (an alternative early desing consisting of two gratings is demonstrated in [36]) combined with two retro-reflectors. Initially, the incoming beam is dispersed by the grating towards the horizontal retro-reflector where it is horizontally shifted. The beam hits the grating again and is dispersed towards the vertical retro-reflector. Subsequently it propagates in a direction parallel to the incoming beam but it is horizontally shifted. In the vertical retro-reflector the beam is shifted upwards, and reflected again towards the grating. Then it gets dispersed to the horizontal retro-reflector and reflected back to the grating. Finally, the beam exits the compressor being re-compressed to its original duration.

2.9 Summary

Throughout this chapter we have focused on the principles of operation of a couple of table-top lasers that cover the NIR spectral region. Within this framework we illustrated the Q switching technique used for generation of ns laser pulses. Next, we moved on to the mode locking technique developed to obtain ultrashort laser pulses in the fs regime. In this context, the main parts (oscillator, stretcher, amplifier, compressor) of a CPA based laser system were described in detail.

Chapter 3

Sources in the VUV and SXR spectral regions

3.1 Synchrotron radiation

It was in 1895 when the German physicist Wilhelm Conrad Rontgen developed the X-ray tube [37]. In this early experiment, electrons were accelerated towards a metal target losing part of their energy due to deceleration. The emitted radiation forms a continuous spectrum of X-rays via what is called the bremsstrahlung effect. It also exhibits characteristic K-α and K-β line radiation. The aforementioned experiment, was based on the fundamental principle that accelerating and/or decelerating charged particles emit electromagnetic radiation. The advent of large scale accelerators, resulted in charged particles moving at relativistic velocities. In that case, the emitted radiation is confined in a small cone tangent to the path of the particle. The first experimental observation of the so called synchrotron radiation was in 1947 [38].

In the early days, the bending magnets in storage rings, were the first source of synchrotron radiation. In this geometry, a relativistic electron travels in a circular path, emitting radiation over a broad range of angles in its own frame of reference. By applying a Lorenz transformation the observer in the laboratory frame sees a different radiation pattern as the emission gets confined in a narrow cone (see Figure 3.1) of half angle given by [39]:

$$\theta \simeq \frac{1}{2\gamma} \tag{3.1}$$

and

$$\gamma = \frac{1}{\sqrt{1-\beta^2}} = \frac{W}{m_e c^2} \tag{3.2}$$

where W expresses the relativistic energy of the electron, m_e the rest mass, c the speed of light in vacuum and $\beta \equiv \frac{v}{c}$. The emitted radiation, spans a broad range of energies which is further shifted to the X-ray spectral range as a result of the Doppler effect. The total power emitted by a single electron in a bending magnet of radius R

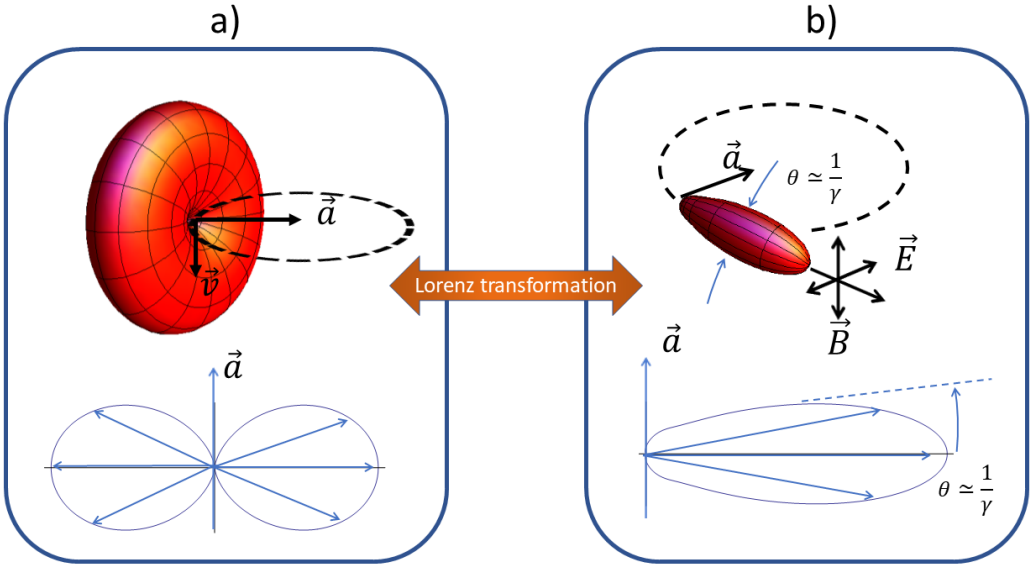

Figure 3.1: The radiation pattern emitted by a particle in bending magnet. a) In the reference frame of the moving particle, the pattern exhibits the characteristic 'donut' shape and the emission is absent in the direction of acceleration. In that case the radiation is emitted in a broad range of angles. b) In the laboratory frame of reference the radiation is confined to a narrow cone tangent to the path of the accelerating particle.

is given by

$$P = \frac{e^2 c \gamma^4}{6\pi\epsilon_0 R^2} \tag{3.3}$$

where ϵ_0 is the vacuum permittivity.

With the passing of time, synchrotron facilities evolved and so-called third generation facilities incorporated planar arrangements of magnets with alternating polarity. In that case, the emission of radiation is a result of the oscillatory movement of the electrons, enforced by the magnetic field of the undulator (or wiggler) [1]. The first theoretical investigation of radiation emitted by fast electrons passing through a succession of electric or magnetic fields of alternating polarity was reported by Motz [40], whereas an experimental study of undulator radiation was first demonstrated by Ginzburg in 1953 [41]. Later in 1960 Phillips developed the so called Ubitron, an undulator emitting at microwave wavelengths [42].

Undulators can be classified as planar or helical depending on the plane in which the magnetic field lies. In the former case, linearly polarized radiation is generated whereas in the latter case the polarization is circular or elliptical.

When working in the frame that moves together with the electron this effect corresponds to an oscillating dipole, in the framework of classic electromagnetism. In

[1] When the electron's angular excursions are small compared to the natural radiation width, the arrangement is called undulator, otherwise it is referred to as a wiggler

the particle's reference frame, the electron 'feels' the magnetic structure moving towards it. The relativistically contracted wavelength of the emitted radiation is then expressed as:

$$\lambda = \frac{\lambda_u}{\gamma} \tag{3.4}$$

where λ_u is the undulator period. The emitted wavelength is further reduced in the laboratory reference frame due to the Doppler shift. Hence, the wavelength of the Doppler-shifted, on-axis emitted radiation is given by

$$\lambda = \frac{\lambda_u}{\gamma^2} \tag{3.5}$$

A more detailed calculation taking into consideration the oscillations of the longitudinal component of the electron's velocity gives[2]:

$$\lambda_{FEL} = \frac{\lambda_u}{2\gamma^2}\left(1 + \frac{K^2}{2} + \gamma^2\theta^2\right) \tag{3.6}$$

where, $K = \frac{eB_u\lambda_u}{2\pi cm_e}$ is the so-called undulator parameter [3], and θ is the angle of observation (for the on axis case $\theta = 0$). One easily notices that the wavelength can be tuned by varying the magnetic field or the undulator period. The small electron excursions ($K \leq 1$) correspond to the undulator limit whereas, when ($K \gg 1$) one approaches the wiggler limit. By comparing the half angle of the radiation cone mentioned above to the maximum excursion angle given by

$$\theta_{exc} \simeq \frac{K}{\gamma} \tag{3.7}$$

one sees that in the case of undulators the excursions take place within the cone, thus allowing for interference of radiation coming from different parts of the oscillatory trajectory. However this can not be realized in the wiggler limit. It is also worth noting that the power of the emitted radiation is proportional to the number of electrons in the undulator. Whereas, as we will see later, the power scales quadratically with the number of electrons in FEL's.

Now, we can make an estimation regarding the width of the undulator spectrum. Using equation 3.6 and for a typical value of the undulator parameter ($K = 1$) we get

$$\lambda_{FEL} \simeq \frac{\lambda_u}{2\gamma^2}\left(1 + \frac{1}{2} + \gamma^2\theta^2\right) \tag{3.8}$$

[2]This calculation assumes a negligible electric field in the undulator. As we will see later on, this is not valid for FEL radiation

[3]Typical undulator parameters range between 1 and 3 assuming undulator periods on the order of a few cm and magnetic fields on the order of $\approx 1T$

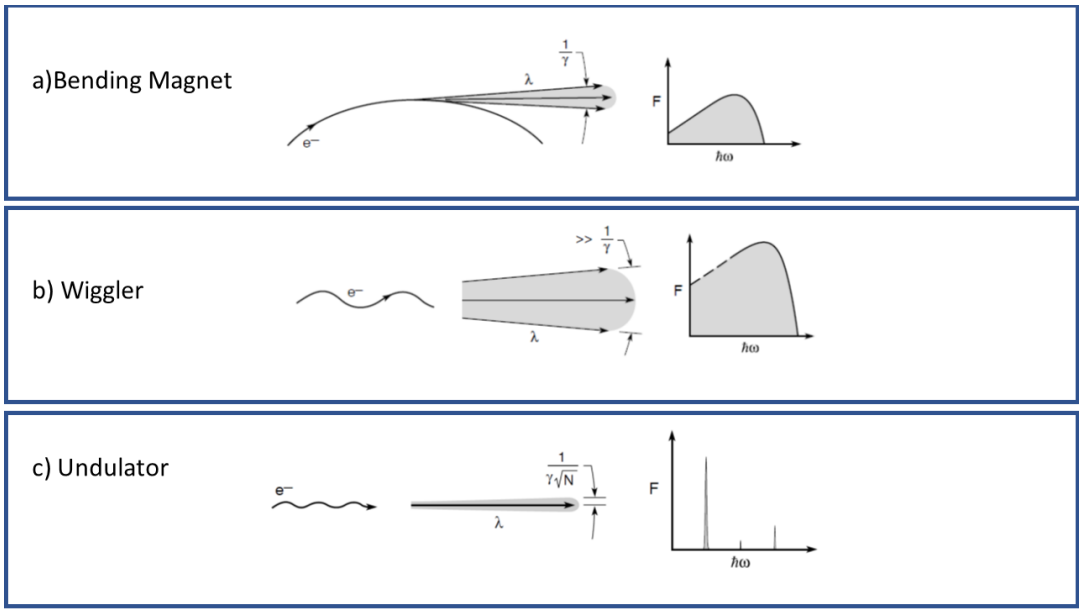

Figure 3.2: A summary of the different magnetic structures, used to generate Synchrotron radiation. a) a bending magnet exhibits a broad radiation spectrum, similar to a white-light source. The radiation is confined in a narrow radiation cone. b) A wiggler has a broad radiation spectrum, similar to that of the bending magnet. Furthermore, the radiation is emitted in a broader cone resulting in lower brightness for this arrangement. c) In the case of an undulator, the radiation is emitted in a narrower cone compared to the other two arrangements. In addition the spectrum is narrow and the brightness of the source is higher [39].

Taking λ as the on-axis ($\theta = 0$) wavelength and $\lambda + \Delta\lambda$ as the wavelength corresponding to the half-angle of the radiation cone ($\theta \simeq \frac{1}{2\gamma}$) and then using the equation 3.8, one gets:

$$\lambda \equiv \lambda_{FEL}(\theta = 0) = \frac{\lambda_U}{2\gamma^2}(\frac{3}{2}) \tag{3.9}$$

and

$$\lambda + \Delta\lambda \equiv \lambda_{FEL}(\theta \simeq \frac{1}{2\gamma}) = \frac{\lambda_U}{2\gamma^2}(\frac{7}{4}) \tag{3.10}$$

by subtraction:

$$\Delta\lambda = \frac{\lambda_U}{2\gamma^2}(\frac{1}{4}) \tag{3.11}$$

as a result:

$$\frac{\Delta\lambda}{\lambda} \simeq \frac{1}{6} \tag{3.12}$$

Thus, approximately 20 % of the spectral bandwidth lies within the radiation cone. A summary of the different sources of synchrotron radiation is presented in Figure 3.2.

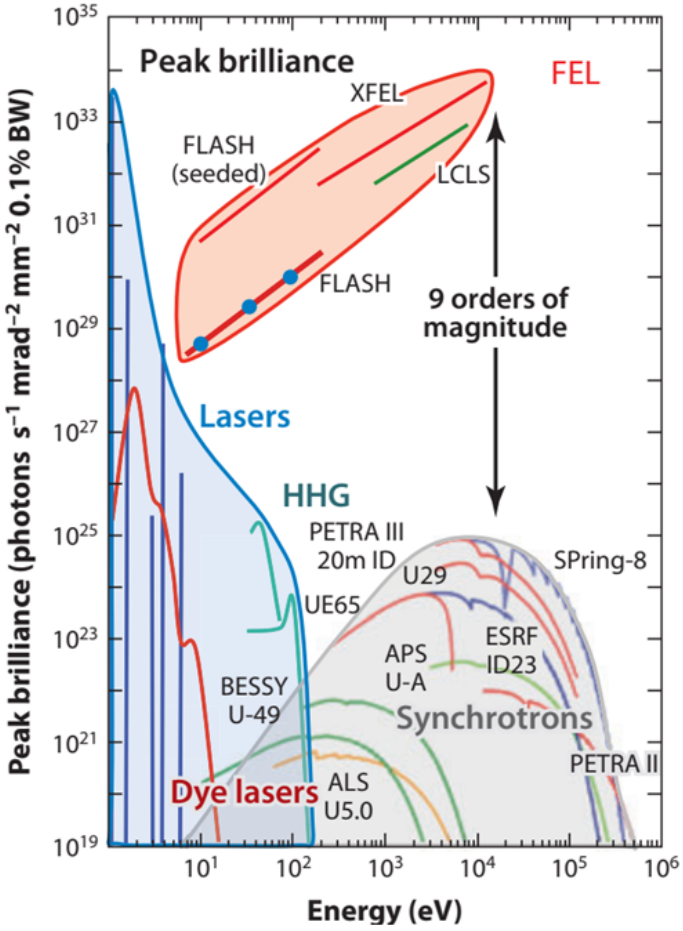

Figure 3.3: The measured FLASH FEL peak brilliance (blue points) compared to that of other sources. [46].

3.2 The free electron laser (FEL) principle

Opposite to conventional solid state lasers, FELs employ a beam of highly energetic relativistic electrons as a gain medium. An undulator forces the electrons to oscillate in a direction orthogonal to the direction of propagation, leading to emission of electromagnetic radiation.

The FEL radiation exhibits most of the desired properties of a table-top laser such as spatial coherence, short duration and partial temporal coherence. In addition, the aforementioned characteristics are combined with the high photon energy of the FEL radiation. When compared to synchrotrons, FELs emit radiation of higher brightness and significantly shorter duration (see Figure 3.3).

The first theoretical approach to the FEL lasing process goes back to 1971 [43]. This pioneering work of Madey and his coworkers unveiled the possibility of generating coherent X-ray radiation by leading a beam of relativistic electrons through an undulator. This theoretical investigation set the foundation for the first operational FEL, in Stanford University in 1977, lasing at a wavelength of 12μm [44, 45].

3.3 The micro-bunching process

The active medium of the FEL is a bunch of approximately 10^9 relativistic electrons. This beam propagates through an undulator and the emission of radiation is a result of the oscillatory movement of the electrons enforced by the magnetic field in the undulator. Electrons that oscillate at random relative phases result in emission of incoherent radiation. In that case the total field strength is proportional to the square root of the number of electrons. On the other hand, if one forces the electrons to oscillate in phase, the resulting electric field is greatly enhanced. Most importantly, in the latter case the emitted radiation is coherent. Consequently a question arises, how can one establish the conditions required to ensure coherence?

The answer lies in the phenomenon called micro-bunching. In short, electrons in the undulator interact with radiation emitted by other electrons of the same bunch. Thus, electrons exchange energy with the electromagnetic field. Depending on the relative phase between the electrons and the electromagnetic field, part of the electrons will gain energy whereas others will lose energy to the field. The former electrons will travel along a transverse trajectory with larger amplitude compared to the latter electrons. This will in turn modulate the longitudinal velocities of the particles. Hence, the initial electron bunch is actually 'sliced' into smaller pieces, the so called 'micro-bunches'. It is worth noting that the length of the micro-bunches is similar to the wavelength of the emitted radiation [47].

The faster propagation of the emitted electromagnetic radiation results in a 'slippage' of the more slowly moving electrons with respect to the generated x-ray photons. Thus the aforementioned interaction seems rather unsustainable. However if the radiation leads by exactly one wavelength per undulator period, the transverse velocity component of the electrons and the electric field of the radiation repeatedly point in the same direction, (see Figure 3.4). Hence, the energy transfer is maintained provided that the slippage length equals the wavelength of the radiation. This requirement is equivalent to the constructive interference condition in classical optics. Electrons that belong to the same micro-bunch behave like a single radiating particle, thus ensuring coherence. As micro-bunching becomes strong enough, it enhances the emission of coherent radiation and vice versa. The intensity of the radiation exhibits an exponential increase with the distance of propagation in the undulator, up to a saturation level. The micro-bunching process is schematically presented in Figure 3.5.

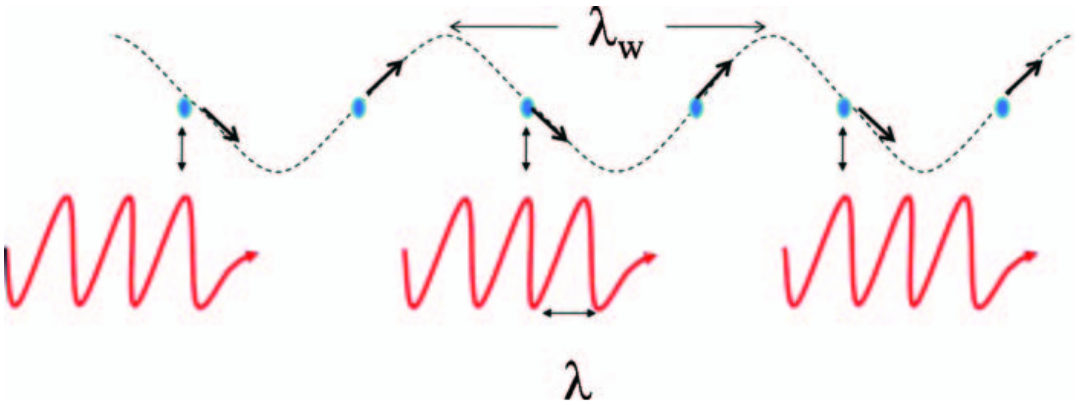

Figure 3.4: The 'slippage' effect. The faster propagation of the emitted electromagnetic radiation results in a 'slippage' of the more slowly moving electrons with respect to the generated x-ray photons. Adapted from reference [48]

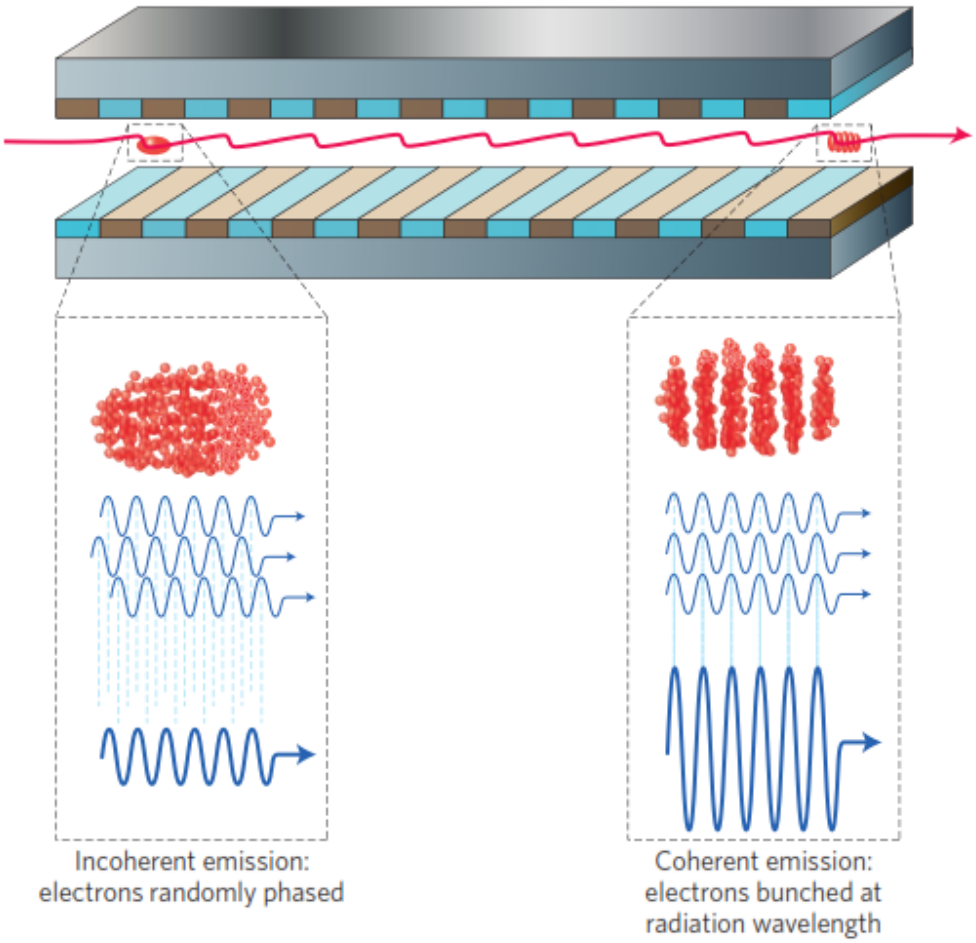

Figure 3.5: The microbunching process: As the electrons oscillate out of phase, i.e. with random relative phases, they generate incoherent radiation. On the other hand, when microbunching is established electrons oscillate in phase giving rise to coherent radiation. Figure adapted from reference [49].

3.4 The self amplified spontaneous emission (SASE) mechanism

One can classify FELs into three categories depending on the different methods of achieving micro-bunching. Two of them, resonator FELs and Seeded FEL amplifiers, incorporate a resonator arrangement. Obvious as it may seem, these types of FELs cover the infrared and optical spectral regions. The reason is the limited reflectivity of any mirrors in the XUV and the X-ray spectral ranges. Thus, in that case it is not feasible to include a resonator. In order to overcome this obstacle, a very long undulator is necessary in order to accomplish lasing in a single pass. It is now the spontaneous emission of radiation that initiates the lasing process. The idea was first proposed by Kondratenko, Saldin and Derbenev in 1982 [50]. This type of FEL process is known as SASE (Self Amplified Spontaneous Emission). We note that the FLASH facility in Hamburg is a SASE-based FEL.

3.5 The free electron laser facility in Hamburg (FLASH)

A key achievement took place in 2000 when the VUV spectral region became accessible to FEL operation. At that time, accelerator physicists and engineers demonstrated lasing at 109nm [51] and soon afterwards, it reached GigaWatt (GW) peak power levels [52]. The generated wavelength was further reduced to 82nm in 2002 [53] and 32nm in 2005 [54]. In the same year the VUV FEL in Hamburg was renamed 'FLASH'. A further success took place in 2007 [55] when the fifth harmonic at 2.7nm reached the important spectral region known as the 'water window'. The layout of the FLASH FEL is depicted in figure 3.6. The four main parts are: a photo-injector, a linear accelerator, the compressors and the series of undulators.

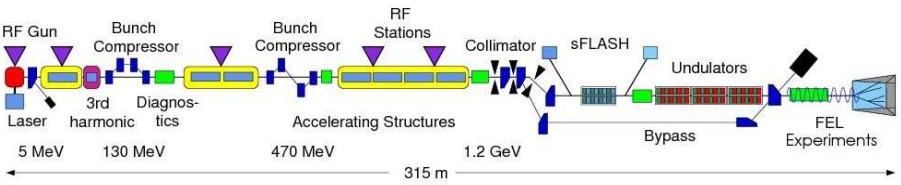

Figure 3.6: A schematic layout of the FLASH FEL in Hamburg. Figure adapted from [4]. The purple triangles correspond to the RF stations used to power the accelerating modules (light blue squares) and the RF gun. In addition, between the segments, quadrupoles (green squares/rectangles) are placed in order to achieve beam focusing and also serve as diagnostic tools. The bunch compression takes place by means of the magnetic chicanes (navy blue squares). A collimator (black triangles and navy blue wedges) is used in order to remove electron beam halo, thus preventing radiation damage in the permanent magnets of the undulator (green and red rectangles).

3.6 The photo-injector

The photo-injector has to meet some demanding requirements that are crucial for initiating the SASE process. Specifically, the electron bunch needs to be confined to a small space, have a high current density and a narrow energy distribution. A radio frequency (RF) electron gun is able to satisfy the above stated requirements as Pellegrini first suggested in 1992 [56, 57]. The process is driven by a solid state laser ($Nd:YLF$) that irradiates the cathode to produce photo-electrons. A thin layer of Cs_2Te covers the molybdenum cathode. The result is $5-10$ % efficiency of the photoelectron emission process. The duration of the laser pulse is relatively long ($10ps$) to avoid instabilities associated with a high charge density.

At that stage, each electron bunch carries a charge between $0.5nC$ and $1nC$ and a current of 50 A. Right after its formation the electron bunch undergoes acceleration by an RF electric field of roughly $60MV/m$. Furthermore, in order to preserve a small beam cross section a magnetic solenoid field is superimposed and forces the electrons to move along helical trajectories around the magnetic field lines.

The photo-injector incorporates the acceleration stage to minimize the space charge effect in the bunch. The rapid acceleration to relativistic energies is only possible by means of the RF field, opposite to the dc fields of the conventional cathodes. When the electrons get to the relativistic regime, the attractive forces between parallel currents [4], partially compensate for the repulsion between the electrons in the bunch.

3.7 The linear accelerator

The electron bunches leave the photo-injector having acquired an energy of $5MeV$ and a current of approximately 50 A. However further acceleration is required in order to reach the XUV/X-ray region. Hence a linear accelerator (linac) follows after the photo-injector. The accelerator at FLASH consists of six $12.2m$ long acceleration modules. Each of them contains eight superconducting niobium cavities and every cavity consists of nine cells as one can see in Figure 3.7.

The length of the cells is selected in order to ensure that the direction of the electric field reverses when the electron bunch propagates into the neighboring cell. The system utilizes super-fluid helium for RF module cooling. In addition one should notice that the UV laser of the photo-injector is precisely synchronized to the RF frequency of the accelerator.

[4] In that case, electrons propagating in the same direction, create parallel currents. As is known from classical electromagnetism such currents exert attractive magnetic forces on each other.

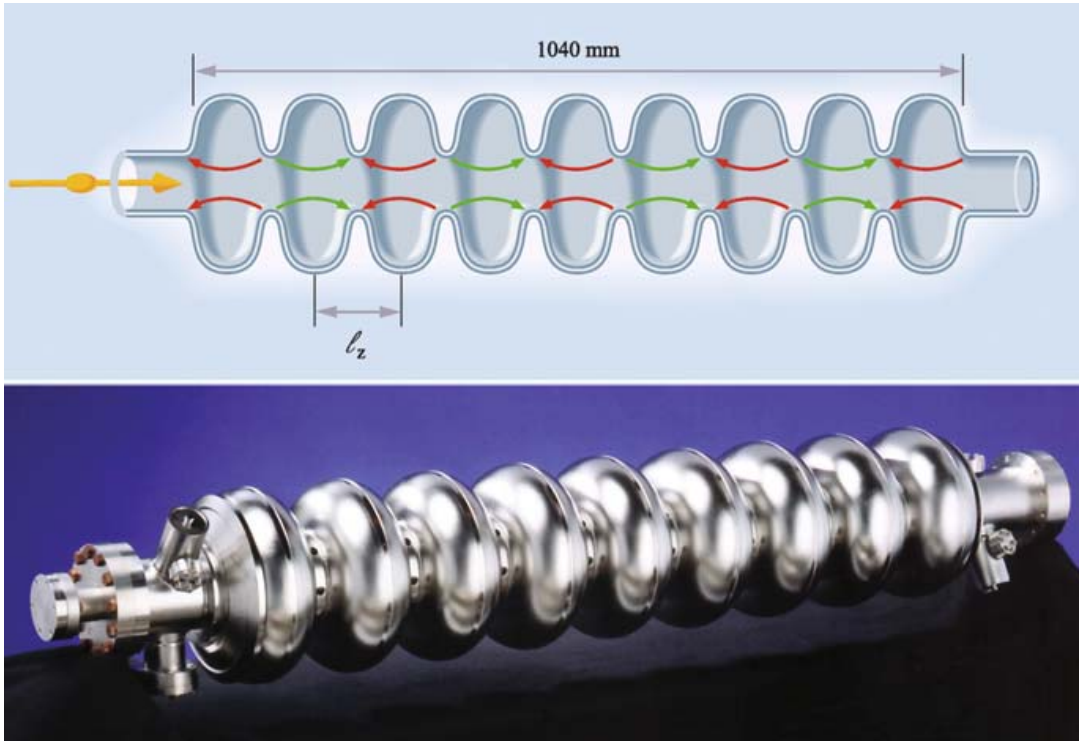

Figure 3.7: The cells of the TESLA cavity in FLASH [58]. The system utilizes super-fluid helium for RF module cooling.

3.8 The bunch compressor

For efficient SASE, there is a need for high peak current and low energy spread of the electron beam that drives the FEL process [59]. In the photocathode, picosecond electron bunches with currents on the order of several tens of A are generated. Thus, in order to acquire high peak currents on the order of several kA, longitudinal compression is required. Additionally, the electron bunches generated in the RF photocathode also exhibit an initial energy spread, due to the inherently stochastic nature of the thermionic emission. Then, the accelerator modules introduce a further energy spread in the electron bunch. This can be understood as follows. The leading electrons of the bunch that arrive first, undergo an energy decrease, whereas the trailing electrons undergo an energy increase due to the slope of the sinusoidal magnetic field in the RF accelerator modules. In order to achieve longitudinal compression, a magnetic chicane that consisting of four rectangular magnetic dipoles is used. Due to these arrangements, the more energetic electrons travel along longer paths compared to the less energetic ones. Hence, the electrons at the tail of the bunch catch up with those at the leading edge of the bunch.

The aforementioned process compensates for the longitudinal stretch of the bunch. However, there are still some minor side effects that influence the shape of the electron bunch. More to the point, when the bunch travels along the curved trajectory in the chicane it emits synchrotron radiation. In the so called coherent synchrotron radiation (CSR) effect, radiation coming from the bunch tail catches up with the head

of the electron bunch, and changes the energy of the electrons there. Furthermore, space charge effects increase the bunch length and the energy spread. Despite the existence of the side effects, the final outcome is an electron bunch with a narrow leading spike that contains $10 - 20$ percent of the total charge and a peak current of more than $1000A$, while the tail of the bunch extends up to few picoseconds. We note that the compression takes place in two stages, first at $130MeV$ and then at $470MeV$ in the case of the FLASH FEL.

3.9 The undulator

The next main component of the FLASH FEL is a planar arrangement of magnets with alternating polarity, the so-called undulator chain. The length of the undulator chain is $30m$. It has FE pole shoes while the permanent magnets in between, are made of $NdFeB$.

In order to achieve the aforementioned microbunching effect, we need to ensure that energy transfers from the electrons to the light field. This implies the existence of resonance conditions. Indeed, the undulator selects certain resonant wavelengths of the radiation which is emitted by the oscillating electrons. The resonance condition is given by :

$$\lambda_{FEL} = \frac{\lambda_u}{2\gamma^2}\left(1 + \frac{K^2}{2}\right) \tag{3.13}$$

where λ_U is the undulator period of $27mm$, $K = \frac{eB_u\lambda_u}{2\pi cm_e}$ is the so-called undulator parameter and $\gamma = \frac{E}{m_e c^2}$ is the well-known relativistic factor. One easily notices that the resonance wavelengths are the same as those generated by the undulator (see equation 3.6, for the on-axis condition $\theta = 0$). Furthermore, one sees that the wavelength can be tuned by varying the undulator period, magnetic field strength or electron bunch energy.

3.10 Properties of the FEL radiation

The key point behind the FEL radiation is its stochastic nature since the amplification process starts from noise. In the cathode, the photoelectron emission is a random process that produces a bunch of electrons where the charge density fluctuates both temporally and spatially. As a result, lasing occurs at a different point in the undulator for each electron bunch. In both the temporal and spectral domain the FEL radiation exhibits a spiky structure (see Figure 3.8) with random phase relations between the spikes. This spiky structure can be attributed to independent wave-packets emitted from different regions of the electron bunch. As can be seen in the same figure, a similar spiky structure is also true for the spectral domain. The number of spikes in the spectral and temporal domain are roughly the same but

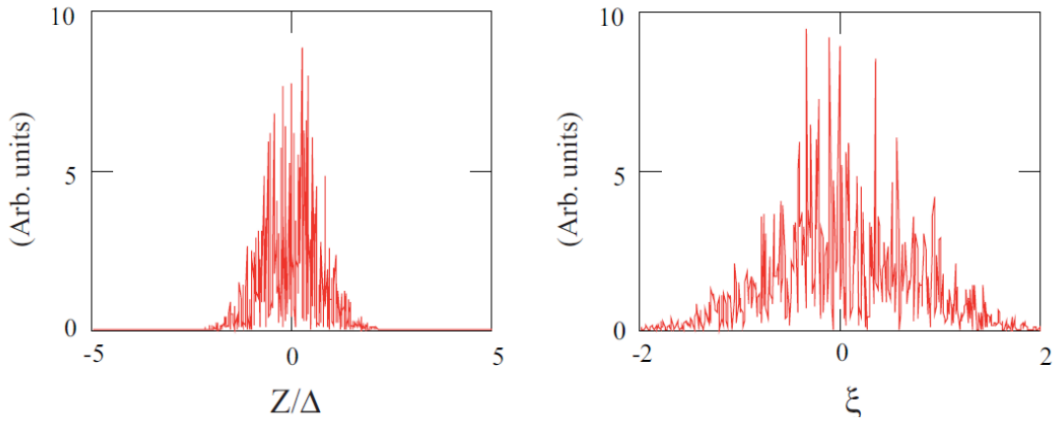

Figure 3.8: FEL radiation in the temporal (left) and spectral (right) domains. Figure adapted from [5].

there is not a one on one correspondence. In addition, each temporal spike exhibits the full bandwidth of the envelope.

The coherence in the longitudinal direction is attributed to slippage effects and in the direction transverse to the diffraction effects. In addition, the spiky structure implies a partial temporal coherence, with the coherence time, τ_c being about the duration of each spike. This duration is much shorter compared to the pulse duration T, which can be estimated by the frequency width $\Delta\omega$ of the spikes and it is on the order of tens of femtoseconds similar to the duration of the electron bunch. Now, if one assumes a flat-top bunch of duration T, the total number of modes included in the FEL pulse can be estimated as:

$$M = \frac{T}{\tau_c} \tag{3.14}$$

From the above discussion, we can see that the longitudinal coherence of the FELs is rather poor (coherence time $\approx 1fs$ for FLASH FEL), especially when compared to solid state lasers (i.e. coherence time $\approx 3ns$ for Nd:YAG laser). On the other hand they exhibit a high degree of transverse coherence since the fundamental transverse mode is dominant. It is also worth noting that the FEL radiation is fully polarized. The structure of the FLASH 1 FEL [60] operating at at a macropulse repetition frequency of $5Hz$ is depicted in figure 3.9. In this case, a macrobunch has 10 micropulses, the number of which is variable, while the same is true for the macropulse repetition frequency which can be set in the $1 - 10Hz$ range. Each macropulse can contain up to 500 microbunches. The repetition rates in FELs are mainly limited by the thermal load on the accelerating structures.

To summarize, a wavelength versus electron energy plot of several FEL facilities ranging from the X-ray spectral region to the mid infrared (MIR) is presented in Figure 3.10. For that reason we used the minimum output wavelength and the maximum electron energy for each facility according to references [47, 61].

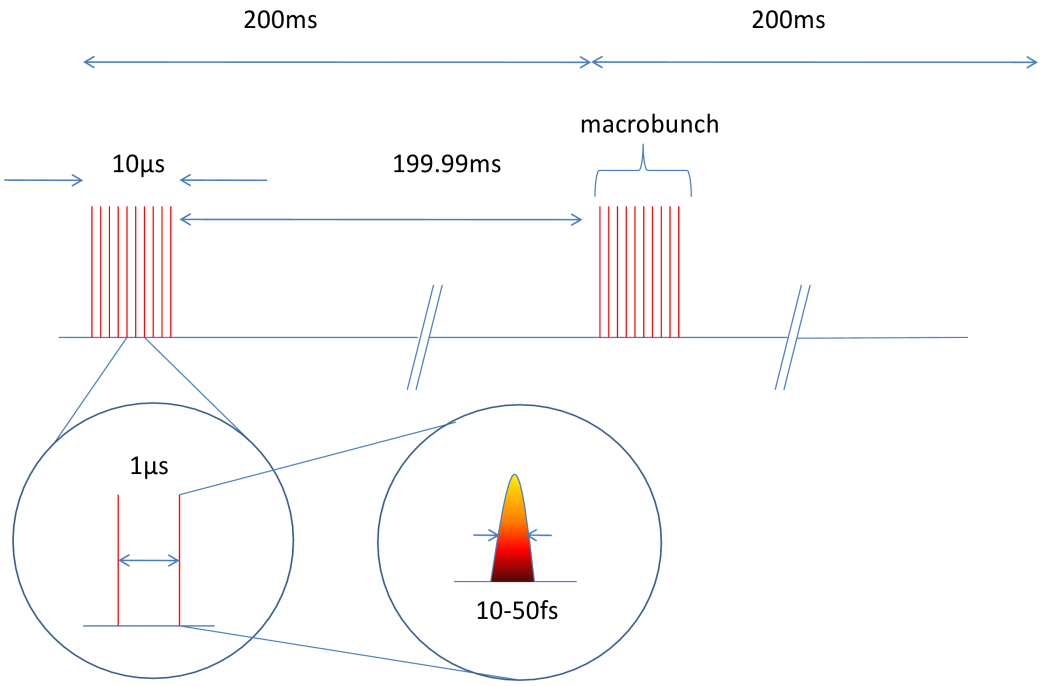

Figure 3.9: The FLASH 1 FEL pulse structure [60], operating at a macropulse repetition frequency of 5Hz.

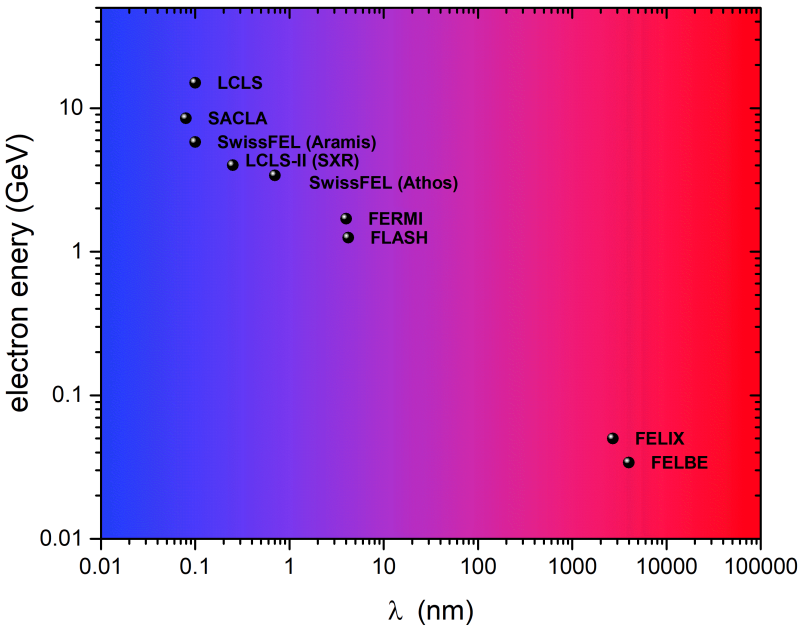

Figure 3.10: Maximum electron energy versus minimum output wavelength for a non-exhaustive list of FEL facilities [47, 61].

3.11 Table-top extreme ultraviolet/soft X-ray laser produced plasma source

Laser driven plasmas, could in principle serve as an active medium for lasing in the extreme ultraviolet (EUV) or the soft X-ray (SXR) region of the spectrum. Indeed, laser produced plasmas (LPP) were the first gain media which were used to implement and demonstrate soft X-ray lasing [62, 63]. Intense emission in such a short wavelength range requires plasma temperatures of several tens of electron volts for the recombination scheme [64, 65] to several hundreds of electron volts for the collision scheme [66]. This condition can be met at high power laser facilities by forming high energy density laser produced plasmas on solid targets [67, 68]. This scheme, comprises a single pass amplifier of the spontaneous XUV or soft X-ray emission radiated by the plasma which is in turn pumped by the laser. Despite the desirable parameters of the aforementioned sources, access to them is usually limited.

Alternatively, table-top XUV and Soft X-ray sources based on commercially available Nd:YAG lasers, can be realized but at the expense of output power and coherence. Thus, taking advantage of resonant emission in high Z elements such as Sn ($4d-4f$) or Gd ($4p-4d$), LPP sources, radiating at around 13.5 nm and 6.7 nm, were successfully demonstrated [69, 70]. The abovementioned sources pose as a low cost, table-top alternative option to the high power laser based EUV/SXR sources. However they suffer from a significant disadvantage: the presence of ionic debris, due to the choice of a solid target as a light emitting medium.

3.11.1 Sources based on gas puff targets

An approach applied to overcome the debris issue, uses a gas puff target [71, 72] instead of a solid target. In this scheme, a gas (atomic or molecular) is injected into the vicinity of the laser focus under high pressure. By means of the gas puff target approach, the generation of soft X-ray (SXR) radiation in the $1-22$ nm wavelength range was demonstrated [73]. The gas puff target setup allows for operation at repetition rates of up to 10 Hz. These desirable features were confirmed in experiments where high power lasers were used to deliver LPP sources based on a gas puff target [74]. On the other hand, this arrangement exhibits a non-negligible disadvantage, that is the degradation of the nozzle by plasma after a long period of operation.

As a clear next step in the development of gas puff targets, a double gas puff target was used as the medium to generate radiation in the EUV/SXR spectral region [75]. In this geometry, a low Z gas is used to confine a high Z target. Thus, it is possible to produce a gas puff target with high gas density at a larger distance from the nozzle preventing the degradation induced by the generated plasma. By using the double gas puff target, a higher SXR/EUV generation efficiency, compared to the single gas puff target, was achieved. In a recent experiment a conversion efficiency as high as $\sim$ 0.42 percent was achieved for a wavelength of 13.5 nm, using a Xe/He

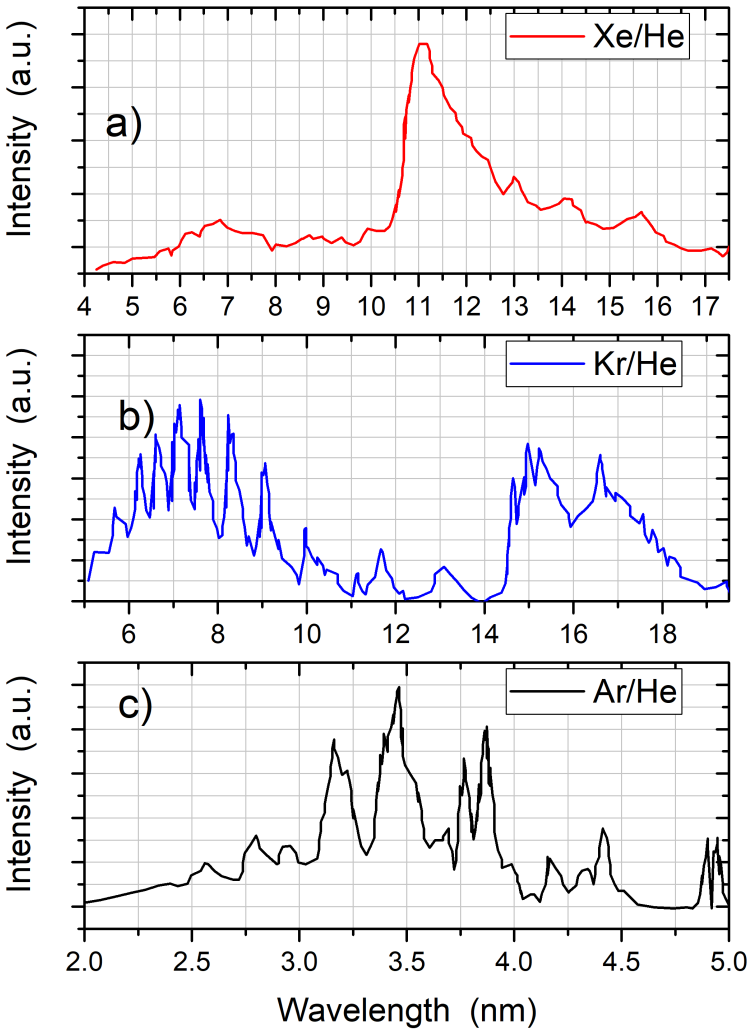

Figure 3.11: Emission spectra obtained for LPP sources based on the double gas puff target geometry. Three different gases a) xenon, b) krypton, c) argon were used as inner targets while helium was the confining outer gas (courtesy of A.Bartnik)

double gas puff target [76]. Examples of emission spectra covering the EUV/SXR spectral region are shown in Figure 3.11. The spectra were obtained for different inner gases (Xe, Kr, Ar) while using He as the outer gas in the double gas puff target, for confinement. The LPP sources should be considered as point sources and as such, their emission spans a 4π solid angle. Hence the radiated intensity scales as $\frac{1}{r^2}$, where r describes the radial distance from the point source.

By means of the double stream gas puff target approach, radiation fluence on the order of 1 J/cm^2 was reached. A non exhaustive list of applications of this table-top source includes the creation and investigation of XUV photoionized plasmas [77], XUV microscopy [78] or near edge X-ray fine structure (NEXAFS) spectroscopy [79] for material science and soft X-ray dosimetry which is relevant to the field of radiobiology [80].

3.12 Summary

To summarize, this chapter concerns a number of laser based XUV and SXR sources. Specifically, it introduced the principles of operation behind the free electron lasers (FEL's), where emphasis was put on the micro-bunching process and the SASE mechanism. The emphasis was placed on the FLASH FEL facility at which our experiments were carried out. A detailed description of the main parts of FLASH, and the properties of the emitted radiation was provided. Subsequently, attention was turned to LPP laser sources, which constitute an alternative method for generation of EUV and/or soft X-ray radiation. In that case the double stream gas puff target scheme, used in our experiments was elaborated on.

Chapter 4

VUV ionization of Kr

When electromagnetic radiation of sufficiently high frequency is absorbed by an atom, one or more electrons are liberated. This so-called photoelectic effect was first observed by Hertz in 1887 [9]. Atomic photo-ionization is undoubtedly the most fundamental process pertaining to intense laser-matter interactions. Despite having been studied in depth over the passage of time, a lot of its fundamental properties remain inaccessible up to now. The short-wavelength of the FEL radiation permits the study of inner shell (even core shell) atomic photoionization at high intensities which is not accessible by means of the conventional solid state lasers, emitting at significantly lower photon energies (see Figure 4.1).

Inner shell and core level atomic and molecular photoionization has been exhaustively studied at synchrotron facilities [81, 82], over the last few decades. However, as already mentioned in the previous chapter, FELs exhibit significantly higher brightness compared to the third-generation synchrotrons and the laser based XUV and/or SXR sources. Hence they give rise to nonlinear processes such as multiphoton absorption [1], that are well beyond the limits of synchrotrons. The aforementioned FEL characteristics make it the most favorable source for the investigation of the fundamental nonlinear processes atomic and molecular physics.

The first AMO experiments at the FLASH facility, focused on multiphoton ionization of atoms and simple diatomic molecules irradiated by FEL pulses. In these experiments noble gases or diatomic gases were used as targets and the information behind the physical process was extracted by applying time of flight (TOF) spectroscopy to the product ions. Hence, in 2005 Wabnitz and his coworkers [84] observed the multiple ionization of Xe and Ar irradiated by VUV radiation at 98 nm, and they attributed the appearance of highly charged ions (Xe^{6+},Ar^{4+}) to sequential multiphoton processes. In a similar experiment Sorokin and his coworkers [85] selected the FLASH photon energies at 42.8 and 38.4 eV just above and below the threshold for sequential two-photon double ionization of Ne via Ne^{+} at 41.0 eV. Their observations also supported the dominance of the sequential nature of two-photon double

[1] It was the german physicsist Maria Goppert Mayer that first investigated the possibility of a two-photon absorption process in 1931 [83]

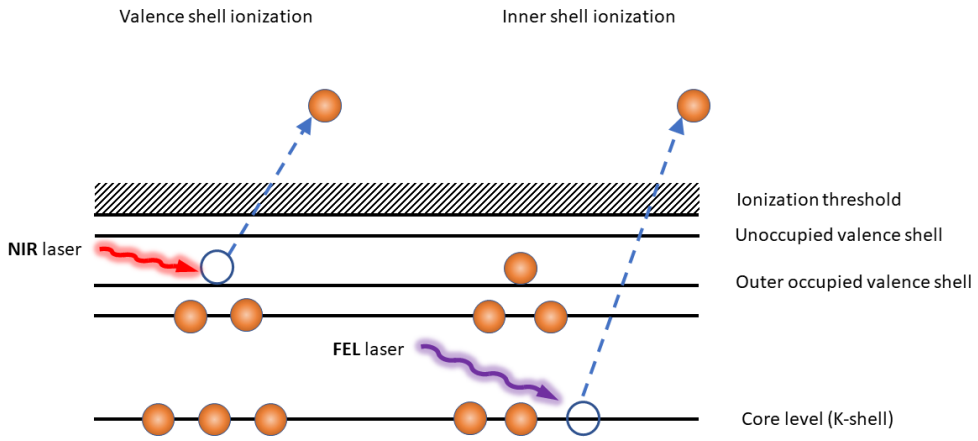

Figure 4.1: Different ionization scenarios: when a NIR laser field irradiates a small quantum system (atom and/or molecule) it induces valence shell ionization. On the other hand a short wavelength FEL photon can access the core level electrons.

ionization in short wavelength laser fields. In addition, Moshammer et. al [86] used the Heidelberg reaction microscope (REMI) [87] to investigate the ionization of Ne and Ar irradiated by FLASH operating at a wavelength of 32 nm. Their findings indicated the dominance of the nonsequential mechanism in this case.

Furthermore, ionization of Xe was investigated upon irradiation by FLASH pulses at a wavelength of 13.3 nm. This photon energy region, is of particular interest for Xe since it includes the $4d \longrightarrow \epsilon f$ giant resonance. With the aid of this strong XUV field, Sorokin et.al. [88] observed an unexpectedly high degree of ionization up to a charge state of Xe^{21+}. This rather unusual finding was further examined in a comparative study on the ionization of Kr, Xe, Ne and Ar at 13.5 nm [89]. The results, further confirmed the significantly higher degree of ionization for Xenon as opposed to the other rare gases. Concerning the molecular ionization, early attempts [90, 91] focused on N_2 since it has already been extensively studied with synchrotrons [92].

Similar experiments took place at other FEL facilities like Linear Coherent Light Source (LCLS) [93] where atomic photoionization was investigated in the X-ray region [94, 95] and Riken/Spring-8 SCSS [96] where lower photon energies where used for the study of the photoionization process [97, 98].

In order to complement the aforementioned studies, experiments involving time of flight photoelectron spectroscopy were undertaken to take advantage of the very useful (electronic) structural information carried by the electrons [99, 100].

It is well known that the ionization of atoms in the IR spectral region may follow

Table 4.1: Atomic photo-ionization for different photon energies. As the photon energy is increased, the multiphoton mechanism becomes the dominant process.

$\lambda(nm)$	Photon Energy (eV)	Intensity (W/cm^2) (where $U_p = \omega\hbar$)
800	1.55	$2.60\ 10^{13}$
40	31	$2.10\ 10^{17}$
1	1240	$1.33\ 10^{22}$

three different scenarios: multi-photon, tunneling and field ionization. The classification into one of the three cases is possible by means of the so-called γ parameter developed by Keldysh in the 60's [101]. The parameter can be expressed as

$$\gamma = \sqrt{\frac{I_p}{2U_p}} \tag{4.1}$$

where I_p is the ionization potential and

$$U_p = 9.310^{-14} I\left(W/cm^2\right) \lambda^2\left(\mu m^2\right) \tag{4.2}$$

is the cycle averaged energy that a free electron acquires in the presence of the laser field commonly called as the ponderomotive energy. Now we can distinguish between three different cases : when $\gamma \gg 1$ we are in the multi-photon regime, if $\gamma \simeq 1$ ionization proceeds via tunneling while for $\gamma \ll 1$ field ionization takes place. It is clear that, for a given atom, as the intensity is increased we are shifting towards field ionization.

The Keldysh parameter poses as a good first approach for treating the nonlinear processes in the low frequency region. On the other hand, the high energy of the FEL photons equals or even exceeds the atomic ionization potential, thus making the aforementioned classification inaccurate [102]. A more suitable criterion is to compare the FEL photon energy to the ponderomotive potential. If the energy of the FEL photon is greater than the ponderomotive potential, the process should be treated in the framework of the perturbation theory. The situation is exemplified in Table 4.1.

From the discussion one reaches the very important conclusion that for FEL laser sources: *The single and multiphoton ionization (MPI) are the dominant processes and involve just one or a few photons, i.e., MPI in XUV and X-ray laser fields is a low order process.*

4.1 Two-photon double-ionization

One of the simplest and most fundamental nonlinear processes is atomic two photon double ionization (TPDI). This process is considered a very important tool for

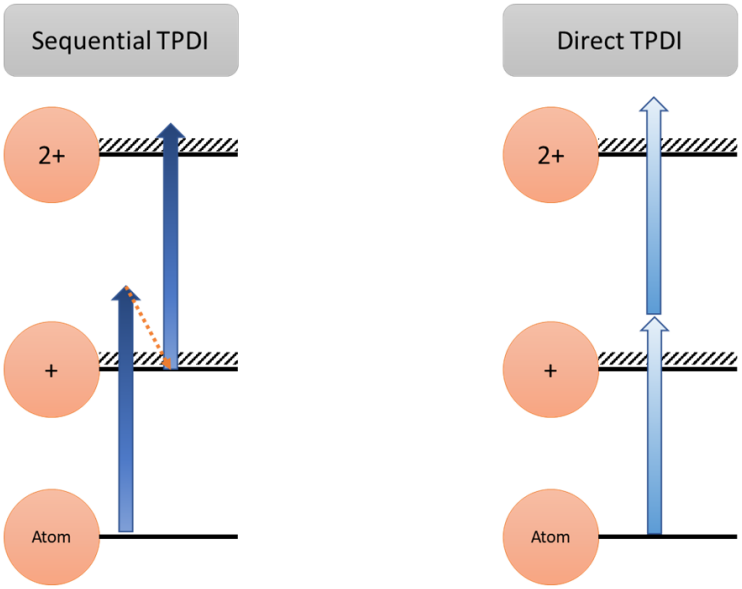

Figure 4.2: Sequential versus direct two photon double ionization (TPDI) processes for atoms irradiated by XUV or soft X-ray FEL photons.

the characterization of sources in the EUV region and as such it has attracted a lot of attention over the past few years. Thus, in addition to the above mentioned experiments, persistent theoretical work [103, 104] has been carried out to establish the framework required to elucidate the nature of the process.

In order to gain a deeper understanding, we should distinguish between the two mechanisms within the two photon double ionization (TPDI) process: the direct and sequential ionization pathways. In direct two photon direct ionization (TPDI), the electrons are emitted simultaneously and due to the conservation of energy, they share the energy provided by the absorption of the two photons. On the other hand, the sequential process proceeds via an intermediate ionic state. Now the energy of the first electron is the difference between the photon energy and the ionization potential of the atom while for the second electron it is the difference between the photon energy and the binding energy of the intermediate ionic state. When the photon energy is larger than the ionization potential of the singly charged ion, the sequential TPDI process dominates. On the other hand the direct process is favored when this is not the case, but twice the photon energy exceeds the sum of the ionization potentials for the neutral and the singly charged ion as seen in Figure 4.2.

Single-photon ionization of Kr atoms [105, 106] and the Kr^{+} [107] and Kr^{2+} [108] ions has been studied extensively at synchrotron sources. Furthermore, the process of resonant two-photon inner shell excitation has been observed by absorption of two 46 eV FEL photons [109]. However there are still plenty of unexplored aspects to be illuminated in the case of TPDI of Kr atoms as we will see later in this chapter.

Several experiments investigated the photo-electron angular distributions (PADs) in

the case of the sequential three-photon triple ionization of Ne [110] at 90.5 eV , the doubly resonant three-photon double ionization of argon at 21.3 and 21.45 eV [111] and the two-photon sequential double ionization of xenon at 23 and 24.3 eV [112]. However, a study involving PADs of the heavier Kr was only recently available [113]. In that work, measurements were taken for five FLASH photon energies ranging from 38 eV to 91 eV.

Although the total ionization cross section is a useful quantity, it contains contributions from several subshells of the atom. Thus, information about the subshell dependent photoionization can be obtained by the so called partial ionization cross section. If one takes into consideration dipole terms in the non relativistic light matter interaction, the partial ionization cross section is given by:

$$\sigma_{if} = \frac{4\pi^2 \alpha a_0^2}{3} h\nu |\langle f| \sum_j r_j |i\rangle|^2 \tag{4.3}$$

where α denotes the fine structure constant, a_0 is the Bohr radius and $h\nu$ the photon energy in Ry.

Angle resolved measurements are of particular interest, since they provide information about the differential partial cross section hence unveiling the angular dependence of the ionization process. The differential partial cross section is commonly expanded in terms of Legendre polynomials (partial wave components) as:

$$\frac{d\sigma_{if}}{d\Omega} = \frac{\sigma_{if}}{4\pi} \sum_{i=0}^{\infty} a_i P_i(cos\theta) \tag{4.4}$$

where the angle θ corresponds to the angle determined by the direction of the photoelectron velocity and the polarization vector of the incident radiation. For ionization by absorption of one photon, it holds that $a_i = 0$ for $i > 2$. Also $a_1 = 0$ since the electron emission should be symmetric along the axis of light polarization. In order for the partial differential cross section to have a physical meaning, the anisotropy parameter is restricted to the $[-1, 2]$ range of values. After expanding in terms of Legendre polynomials, the formula for the photoelectron angular distribution is given by [114] :

$$\frac{d\sigma(E)}{d\omega} = \frac{\sigma(E)}{4\pi} \left(1 + \beta_2(E) * P_2(cos\theta)\right) \tag{4.5}$$

Two-dimensional angular distributions for different β parameters are shown in Figure 4.3, along with the three-dimensional distributions for the same anisotropy parameters.

For sequential TPDI the process takes place in two distinct steps. In the first step an FEL photon ionizes the neutral atom to form a singly charged ion, as the first

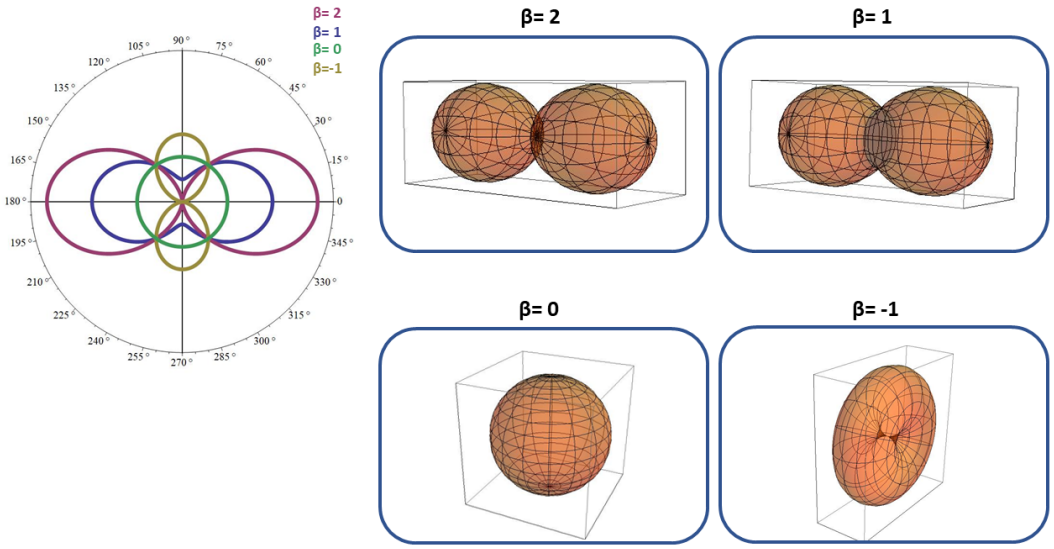

Figure 4.3: Angular distributions for different β parameters ($\beta = -1, 0, 1, 2$) in two and three dimensions.

electron is removed. In a further step, a second electron is liberated by absorption of another FEL photon from the same pulse, leading to a doubly charged ion (see Figure 4.4). In this process, the neutral atom is considered to be unpolarized, while the first ionization step often leads to a polarized intermediate state of the singly charged ion. Specifically, when a hole is created in a p-shell or a d-shell, the result is a polarized intermediate. On the other hand, when the hole is created in a s-shell, the intermediate state is upolarized. The polarization state of the intermediate state is particularly important, since it introduces new features to the process. If one assumes, a single and unpolarized intermediate state, then the first and second emitted electrons are not correlated. Since the intermediate ionic state is upolarized, it has no memory about the direction into which the first electron is emitted. Hence the emission direction of the second electron is independent on the direction of first one. This situation is described in the bibliography as a lack of "true" angular correlation [115, 116]. In the opposite case, where the intermediate state is polarized, the angular distribution of the second electron will depend on this polarization. Thus the two electrons will be correlated and "true" angular correlations are present. Now, the process cannot be described as a product of the two cross sections for the first and second step but should also contain an extra term corresponding to the alignment of the intermediate ionic state.

The angular distribution of the emitted photoelectrons is now given by [117]:

$$\frac{d\sigma(E)}{d\omega} = \frac{\sigma(E)}{4\pi}\left(1 + \beta_2(E) * P_2(cos\theta) + \beta_4(E) * P_4(cos\theta)\right) \tag{4.6}$$

where β_2 and β_4 are the anisotropy parameters multiplied by the second and fourth

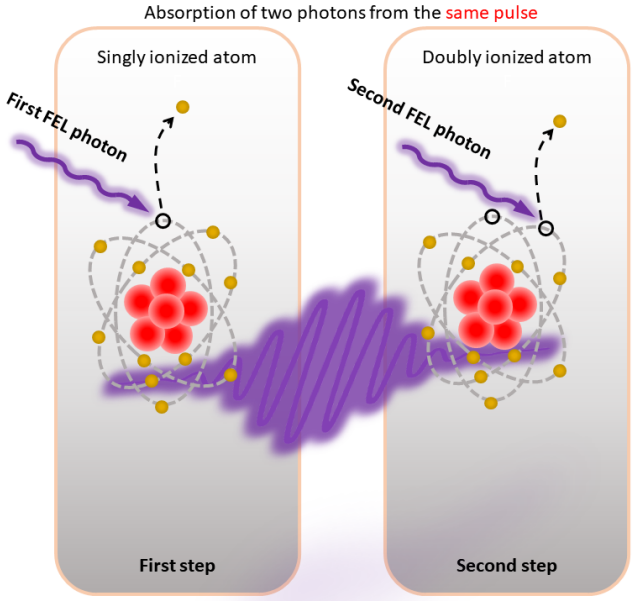

Figure 4.4: A schematic representation of the two-photon double-ionization scenario. This process takes place in two distinct steps.

order Legendre polynomials respectively. The angle θ corresponds to the angle defined by the direction of the photoelectron velocity and the polarization vector of the FEL radiation. The term proportional to fourth order Legendre polynomial is present because two photons are absorbed in this ionization process each of them contributing one unit of angular momentum to the system. In Figure 4.5 angular distributions are presented for different combinations of β_2 and β_4 parameters.

Another subtle issue, refers to the coherent excitation of the intermediate states. Previous studies have suggested that the angular correlation function is very sensitive to the coherent population of the intermediate fine-structure states. However for the Kr^+ $4p^5$ $^2P_{3/2,1/2}$ spin orbit doublet, the energy splitting corresponds to a coherence time [118] of approximately 6 fs. Thus, according to the conditions of our

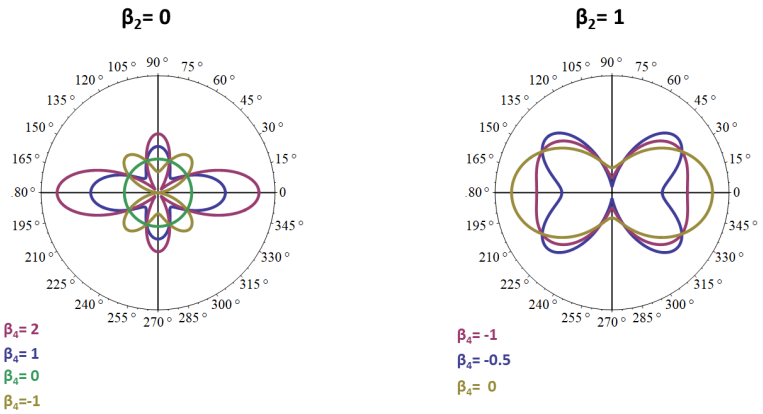

Figure 4.5: Angular distributions for different combinations of β_2 ($\beta_2 = 0, 1$) and β_4 ($\beta_2 = -1, 0, 1, 2$) parameters.

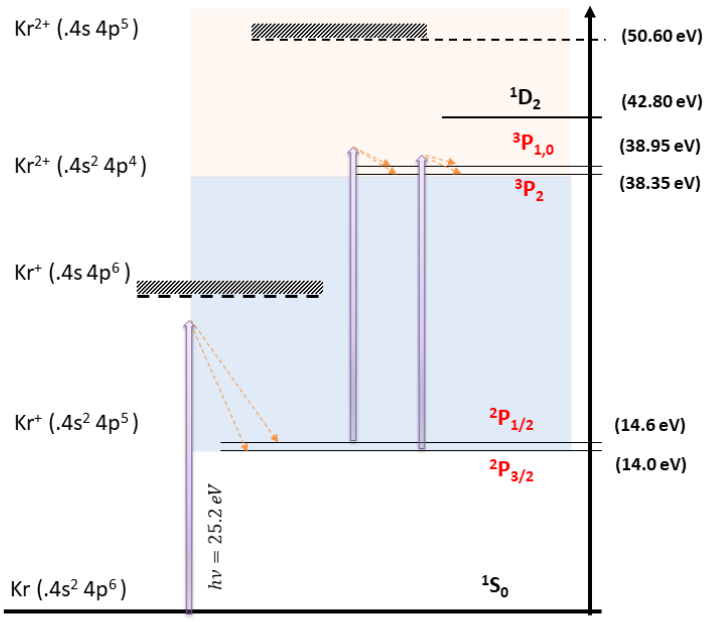

Figure 4.6: Partial energy level diagram corresponding to the conditions chosen in our experiment. In that case, a 4p electron departs at the first step and a 4s electron at the second step of the ionization process.

experiment, an incoherent excitation of the intermediate state can be assumed. Furthermore, it should be mentioned that there have been recent theoretical studies where the contribution of non-dipole effects to the TPDI process has been estimated [119, 120]. For the first ionization step $\beta_4 \equiv 0$ thus, the formula for the photoelectron angular distribution becomes

$$\frac{d\sigma(E)}{d\omega} = \frac{\sigma(E)}{4\pi}\left(1 + \beta_2(E) * P_2(cos\theta)\right) \tag{4.7}$$

In our case, when the Kr atom absorbs a $25.2eV$ photon, one $4p$ electron is emitted and the singly charged krypton ends up in one of the $4p^5\ ^2P_{3/2,1/2}$ spin orbit doublet split states as the intermediate step. In the second ionization step, one more electron is emitted and the Kr^{2+} ion ends up in one of the $4p^4\ ^3P_{2,1,0}$ triplet state components. This is the only energetically available pathway, since there is not enough energy available to reach the $^1D_2$ or the $^1S_0$ state. The energy diagram corresponding to the conditions present in our experiment is shown in Figure 4.6.

4.2 Experiment

In order to record the angular distributions for the emitted photoelectrons we employed Velocity Map Imaging (VMI) electron spectroscopy [121]. The experiment

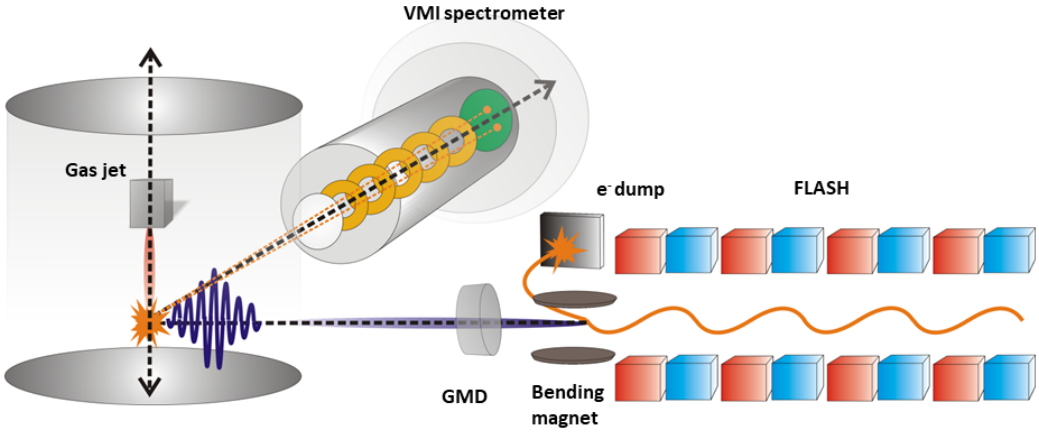

Figure 4.7: A simplified schematic diagram of the experimental setup in the CFEL-ASG Multipurpose (CAMP) chamber. The angle-resolved spectra were recorded by means of a VMI spectrometer. Other important parts are the GMD detector, used to estimate the FEL intensity, and the gas jet via which the krypton is injected to the interaction region.

took place in the CFEL-ASG Multi-purpose (CAMP) chamber [122] installed at the end-station on beamline BL1 at FLASH. The chamber houses a double-sided (electron and ion imaging) VMI spectrometer as depicted in Figure 4.7

For the angular detection of the electrons, we used a microchannel plate (MCP) of $80mm$ diameter (RoentDek DLD80,RoentDek HEX80) with a phosphor screen output (Photonis APD 2 PS 75/32/25/8 I 60:1) combined with a CCD camera operating at a frame readout rate of 10 frames per second (fps). This setup offers detection of electrons in a full 4π solid angle and the VMI provides an electron energy resolution of approximately $0.3eV$. The FEL pulse energies are measured using a homemade gas monitor detector [123] (GMD) developed and installed at the beamline. In that instrument, linear photoionization of a noble gas (Xe) at very low density is applied to estimate the FEL pulse energy on a single shot basis. The photoelectrons and photoions are accelerated in opposite directions by a homogeneous electric field. Then, two Faraday cups are used to measure the large number of photoions and photoelectrons ($10^6 - 10^9$ particles) without risking saturation. This configuration offers the main advantage of being almost transparent due to the very low pressure of the noble gas 10^{-5} mbar. As seen in Figure 4.8a the measurements provided by the GMD indicate pulse energies ranging between $6\mu J$and $10\mu J$. Furthermore, in order to achieve the intensities required for this kind of experiment a pair of nickel-coated KB [124] mirrors are mounted in front of the CAMP chamber at a grazing incidence angle of 3 degrees. Taking into consideration the transmission of nickel-coated KB mirrors (≈ 0.5 according to Figure 4.8b), one estimates between $3\mu J$and $5\mu J$ for the FEL pulse energies at focus.

In addition, a reasonable estimate of a maximum focal spot diameter of $20\mu m$, results in intensities present in our experiments that vary between $2 \times 10^{12} W/cm^2$ and

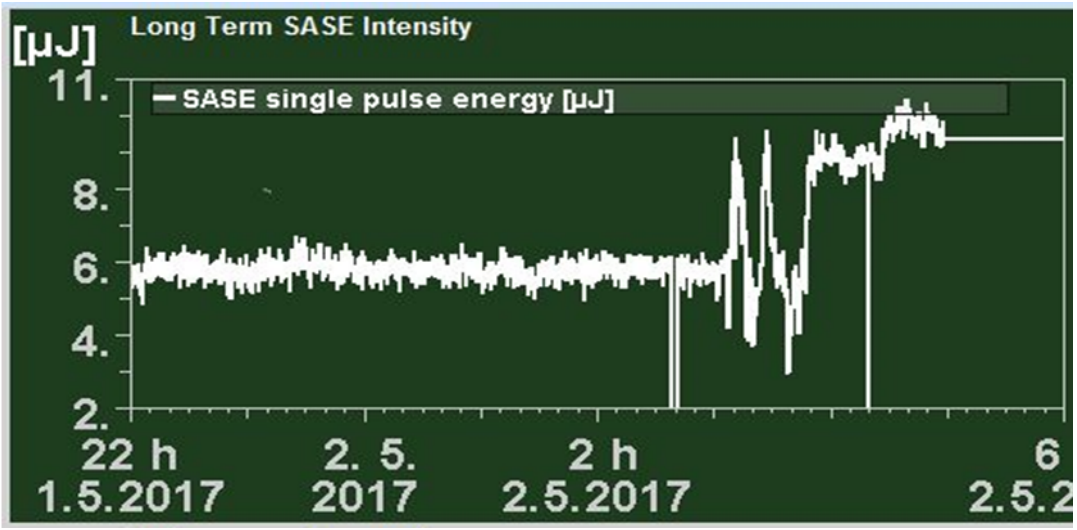

(a)

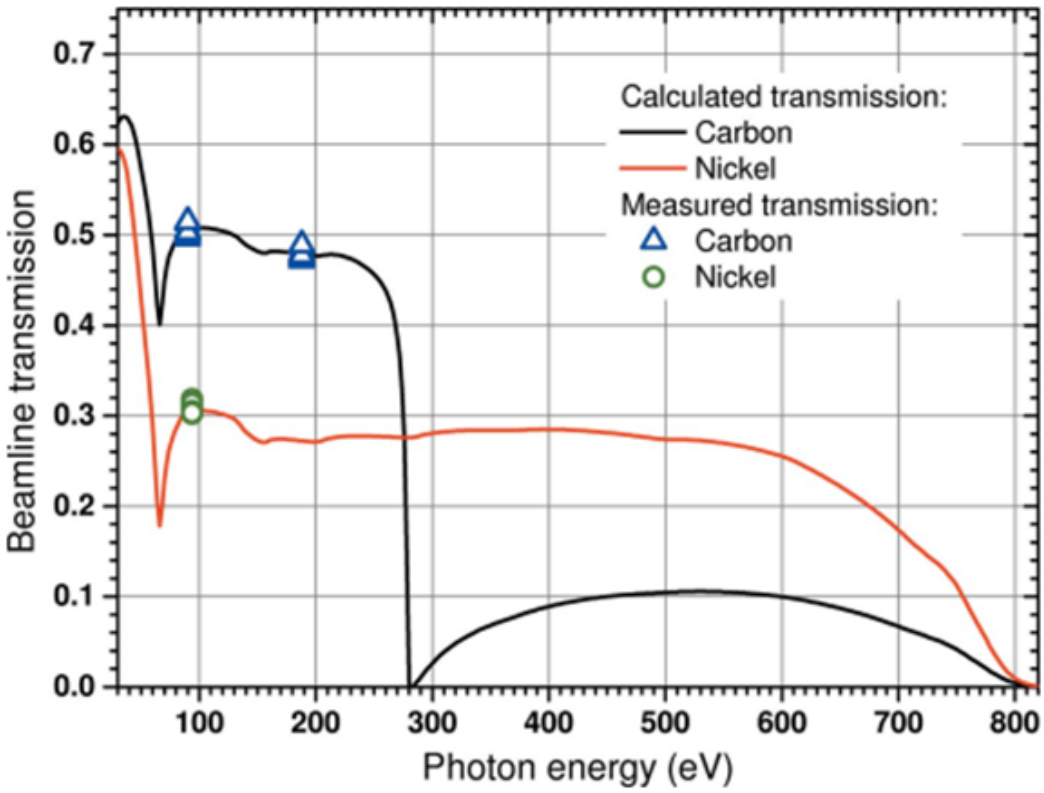

(b)

Figure 4.8: (a) FEL pulse energy measurements acquired by means of the GMD detector. (b) Transmission curve of the nickel-coated KB mirrors. Adapted from reference [125].

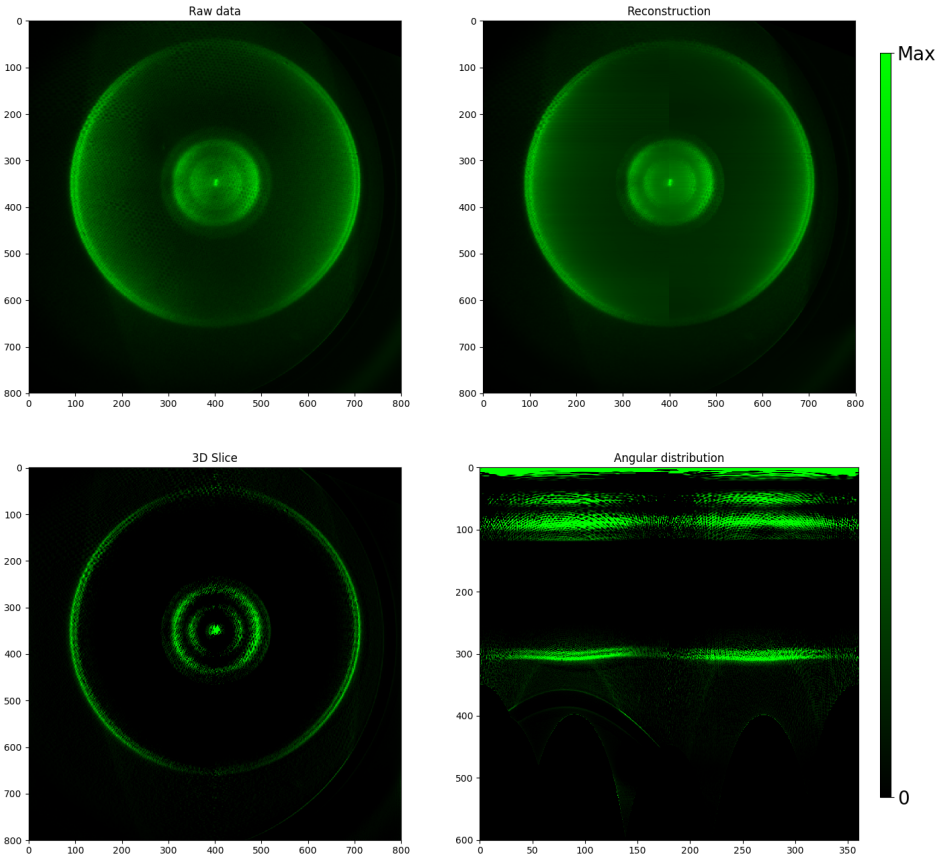

Figure 4.9: The raw VMI data (top left), the reconstructed image (top right), a 3D slice (bottom left) and the angular distribution (bottom right) for the sum of 100,000 single shot recordings.

$5 \times 10^{12} W/cm^2$. The photon energy was set at $25.2eV$ with a FWHM of $0.4eV$. The pulse duration was on the order of $80fs$ with a pulse-to-pulse fluctuation between $60fs$ and $100fs$ due to the SASE related inherent instability. An example of the VMI spectra acquired is presented in Figure 4.9 where we sum all of the $100,000$ raw images recorded. In the same picture we show the corresponding reconstructed image, a 3D slice through the reconstruction and the angle resolved electron spectrum in 2D.

4.3 Results and discussion

In order to investigate the dependence of the asymmetry parameters on the FEL intensity, we divided the raw VMI images according to FEL pulse energy into 5 equal intervals ranging from the lowest 20 percent to the highest 20 percent band of energies. Then, the angular distribution of the emitted photoelectrons was measured

and the β-parameters were extracted for the different FEL pulse energies. As stated earlier, the photon energy was set at 25.2 eV, slightly above the $4p$ ionization threshold for Kr^+ (24.36 eV) making the photo-ionization process less complicated due to the small number of open channels. After absorption of the first FEL photon, the singly charged ion can end up in one of the spin-orbit components of the ^2P state. Subsequently, one more FEL photon is absorbed to leave the Kr^{2+} ion in one of the components of the triplet $^3P_{2,1,0}$ state.

4.4 Angle-averaged photoelectron spectra

In Figure 4.10 we present the intensity dependent angle-averaged photoelectron spectra for three intensity bins. As can be seen, our experimental resolution allows for distinguishing between the $^2P_{3/2}$ and $^2P_{1/2}$ components in the first ionization step. The $^2P_{3/2}$ are strongest, which is to be expected due to the higher cross section as compared to the $^2P_{1/2}$ component in this photon energy range [126]. This is confirmed by Figure 4.11 which summarizes the integrated intensity dependent, angle averaged photo electron signal for all the channels open in our experiment. Furthermore, it can be noticed that the integrated area associated with the first step components reduces with increasing FEL intensity. This behaviour correlates with the gradual increase observed in the signal for all the second step components at higher FEL intensities. In addition, the photoelectron peak at $\approx$ 0.85 eV incorporates contributions from both the $Kr^+ : 4s^2 4p^5\ ^2P_{1/2} \longrightarrow Kr^{2+} : 4s^2 4p^4\ ^3P_{1,0}$ and the $Kr^+ : 4s^2 4p^5\ ^2P_{3/2} \longrightarrow Kr^{2+} : 4s^2 4p^4\ ^3P_2$ transitions, resulting in a higher integrated signal compared to the other two components of the second ionization step.

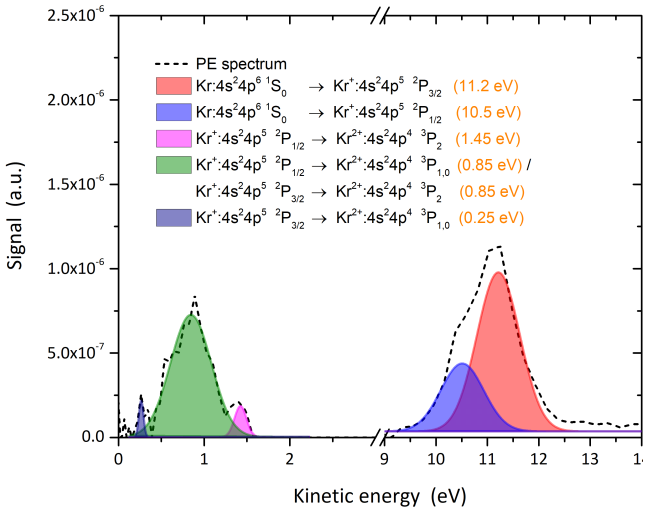

(a)

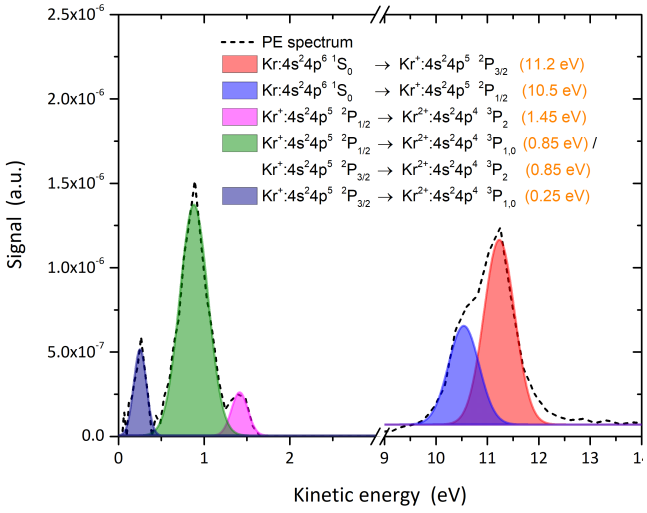

(b)

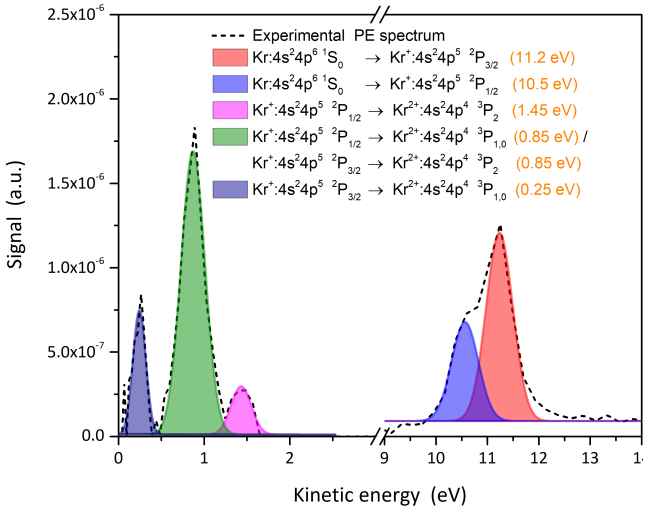

(c)

Figure 4.10: (a) Angle-averaged photoelectron spectrum for an FEL intensity of $5 \times 10^{11}\ W/cm^2$. (b) Similarly for $2.5 \times 10^{12}\ W/cm^2$ and (c) $4.5 \times 10^{12}\ W/cm^2$.

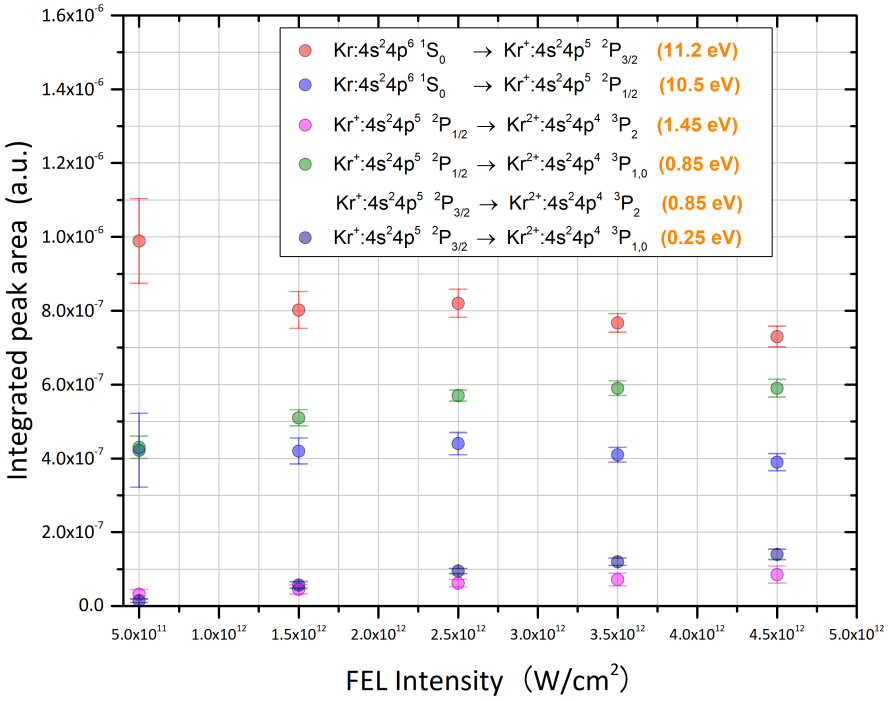

Figure 4.11: The integrated angle averaged photoelectron signal as a function of the FEL intensity, for all five bins.

4.5 Angle-resolved photoelectron spectra for the first ionization step

The angular distributions for the first step of the sequential process are shown in Figure 4.12 for three different FEL intensities. As can be seen, the distributions for both components peak in the direction of the FEL polarization, and they exhibit a minimum perpendicularly to this direction. Using equation 4.6 we extracted the anisotropy parameters, tabulated in Tables 4.2 and 4.3 for the $^2P_{3/2}$ and $^2P_{1/2}$ components respectively. The extracted values for the anisotropy parameters are in reasonable agreement with values previously reported in the bibliography. More specifically for a photon energy of 26.86 eV, Dehmer and his coworkers [127] reported values of 1.50 and 1.60 for $^2P_{1/2}$ and $^2P_{3/2}$ components respectively. More recent calculations performed by Fritzsche et. al. [128] resulted in an anisotropy parameter of roughly 1.4 for a photon energy of 25 eV. This theoretical work was carried out without spin-orbit splitting accounted for.

In Figure 4.13 we present the intensity dependence of the extracted anisotropy parameters for both open channels involved in the first step of the sequential process. In that case, we observe that the β_4 values are negative for both components and have almost the same values. Regarding the β_2 values, they overlap for the highest

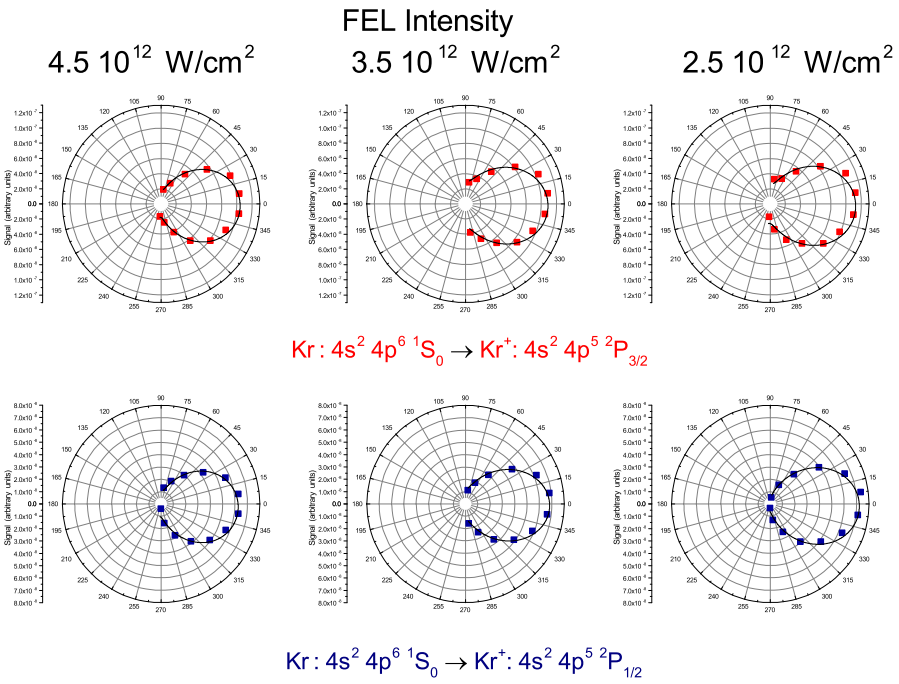

Figure 4.12: Angular distributions for the two open channels of the first step and for three different FEL intensities.

Table 4.2: Anisotropy parameters for the $^2P_{3/2}$ component of the first ionization step.

Intensity (W/cm^2)	$Kr : 4s^2 4p^6\ ^1S_0 \longrightarrow Kr^+ : 4s^2 4p^5\ ^2P_{3/2}$	
4.5×10^{12}	$\beta_2 = 1.21 \pm 0.05$	$\beta_4 = -0.11 \pm 0.04$
3.5×10^{12}	$\beta_2 = 0.94 \pm 0.07$	$\beta_4 = -0.04 \pm 0.06$
2.5×10^{12}	$\beta_2 = 1.04 \pm 0.07$	$\beta_4 = -0.07 \pm 0.07$

Table 4.3: Anisotropy parameters for the $^2P_{1/2}$ component of the first ionization step.

Intensity (W/cm^2)	$Kr : 4s^2 4p^6\ ^1S_0 \longrightarrow Kr^+ : 4s^2 4p^5\ ^2P_{1/2}$	
4.5×10^{12}	$\beta_2 = 1.21 \pm 0.08$	$\beta_4 = -0.13 \pm 0.07$
3.5×10^{12}	$\beta_2 = 1.21 \pm 0.07$	$\beta_4 = 0.00 \pm 0.06$
2.5×10^{12}	$\beta_2 = 1.50 \pm 0.08$	$\beta_4 = -0.10 \pm 0.07$

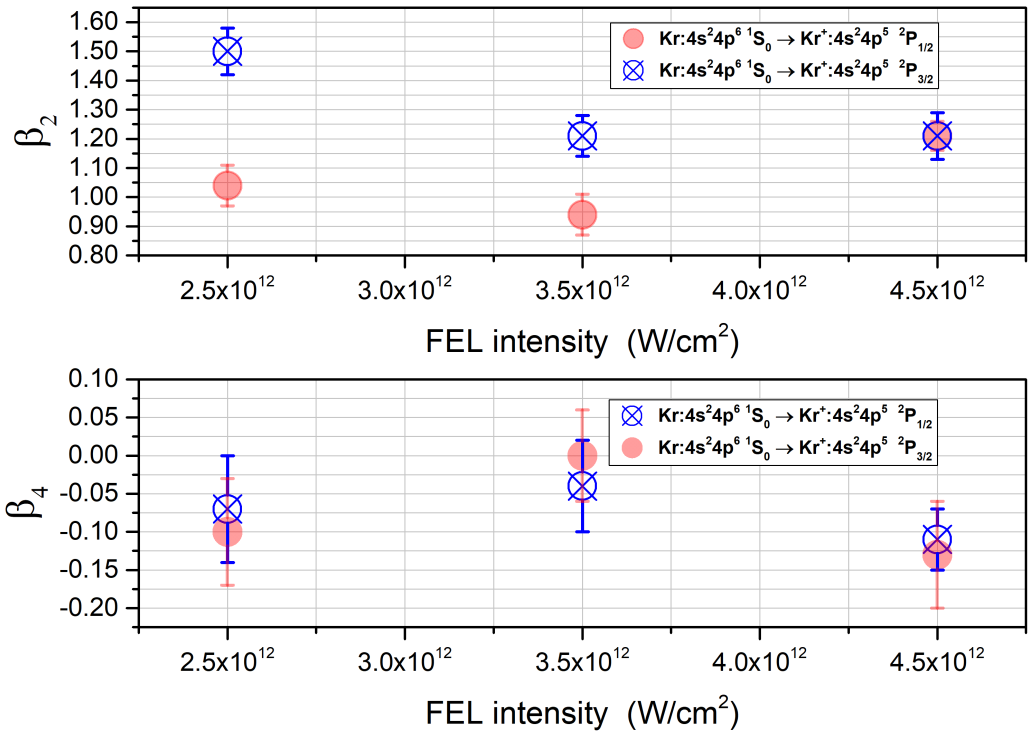

Figure 4.13: The extracted anisotropy parameters (β_2 and β_4) for the first step, as a function of the FEL intensity.

FEL intensity otherwise the $^2P_{3/2}$ component exhibits higher β_2 values.

4.6 Angle-resolved photoelectron spectra for the second ionization step

Moving on to the second step of the two photon double ionization, in Figure 4.14 we present the angular distributions for all the three open channels. Similar to the first step, the angular distributions peak in the FEL polarization direction, and they are minimized perpendicularly to this direction. Using equation 4.6 to fit the angular distribution, we extract the anisotropy parameters for each channel and for each different FEL intensity. The extracted values of β_2 and β_4 parameters are tabulated in Tables 4.4, 4.5, 4.6 for the three components of the second ionization step. Figure 4.15 shows the β parameters as a function of the FEL intensity for each open channel.

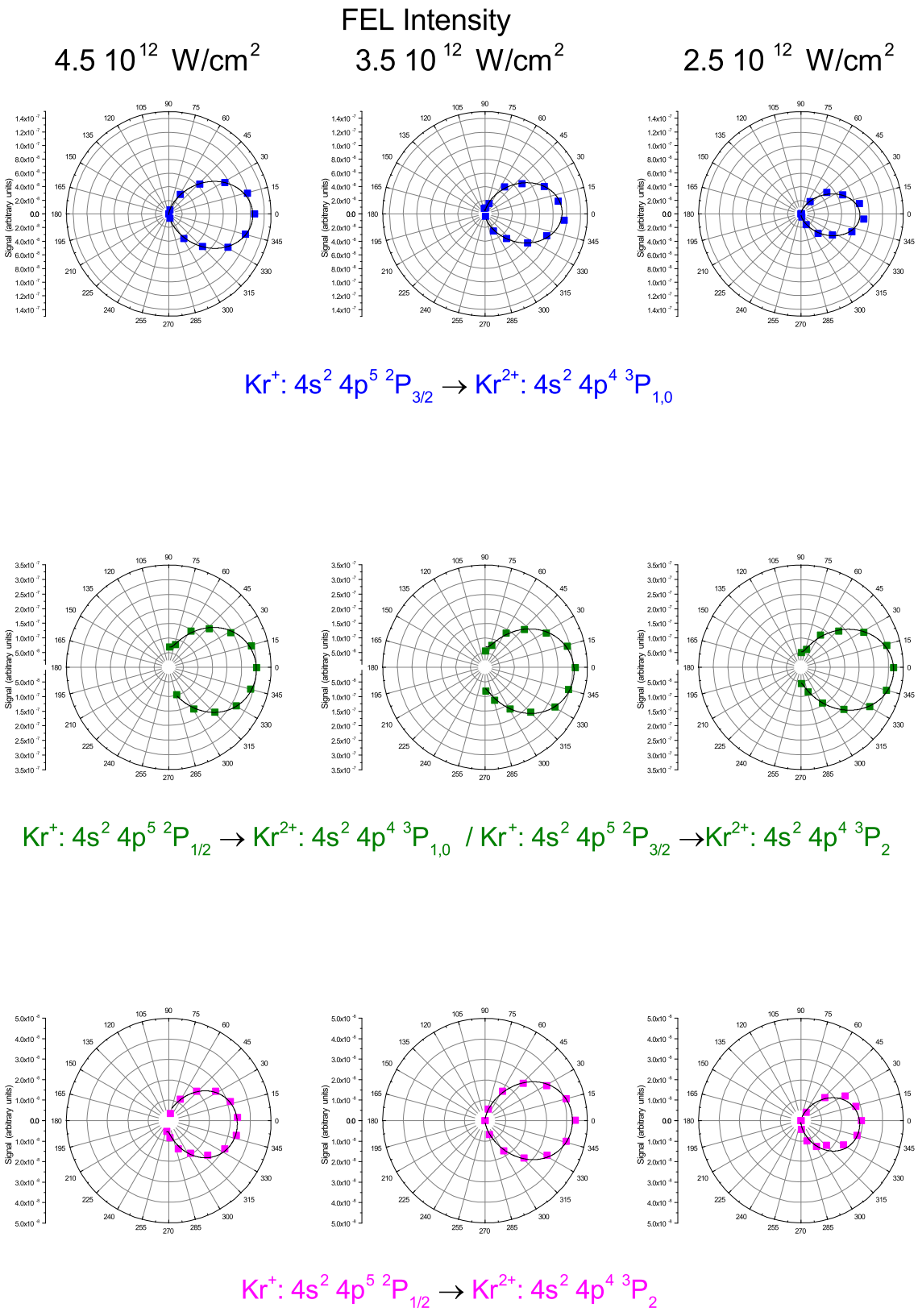

Figure 4.14: Angular distributions of the three channels open in the second step of the sequential process.

Table 4.4: Anisotropy parameters for the $^3P_2$ component of the second ionization step.

Intensity (W/cm^2)	$Kr^+ : 4s^2 4p^5\ ^2P_{1/2} \longrightarrow Kr^{2+} : 4s^2 4p^4\ ^3P_2$	
4.5×10^{12}	$\beta_2 = 1.21 \pm 0.07$	$\beta_4 = -0.20 \pm 0.06$
3.5×10^{12}	$\beta_2 = 1.70 \pm 0.06$	$\beta_4 = -0.22 \pm 0.05$
2.5×10^{12}	$\beta_2 = 1.66 \pm 0.20$	$\beta_4 = -0.24 \pm 0.16$

Table 4.5: Anisotropy parameters for the combination of $^2P_{1/2} \longrightarrow {}^3P_{1,0}$ / $^2P_{3/2} \longrightarrow {}^3P_2$ components of the second ionization step.

Intensity (W/cm^2)	$Kr^+ : 4s^2 4p^5\ ^2P_{1/2} \longrightarrow Kr^{2+} : 4s^2 4p^4\ ^3P_{1,0}$ $Kr^+ : 4s^2 4p^5\ ^2P_{3/2} \longrightarrow Kr^{2+} : 4s^2 4p^4\ ^3P_2$	
4.5×10^{12}	$\beta_2 = 1.04 \pm 0.04$	$\beta_4 = -0.12 \pm 0.03$
3.5×10^{12}	$\beta_2 = 1.03 \pm 0.03$	$\beta_4 = -0.09 \pm 0.04$
2.5×10^{12}	$\beta_2 = 1.24 \pm 0.03$	$\beta_4 = -0.05 \pm 0.03$

Table 4.6: Anisotropy parameters for the $^2P_{3/2} \longrightarrow^3 P_{1,0}$ component of the second ionization step.

Intensity W/cm^2	$Kr^+ : 4s^2 4p^5\ ^2P_{3/2} \longrightarrow Kr^{2+} : 4s^2 4p^4\ ^3P_{1,0}$	
4.5×10^{12}	$\beta_2 = 2.00 \pm 0.08$	$\beta_4 = -0.08 \pm 0.07$
3.5×10^{12}	$\beta_2 = 1.77 \pm 0.08$	$\beta_4 = 0.01 \pm 0.06$
2.5×10^{12}	$\beta_2 = 2.00 \pm 0.15$	$\beta_4 = 0.21 \pm 0.12$

Previous calculations performed by Fritzsche and his coworkers [128], resulted in a $\beta_2 \approx 1.5$ for the ^3P final ionic state. These calculations were averaged over the fine structure components of the first step. By averaging the anisotropy parameters in our case, we obtain values of 1.4, 1.5 and 1.6 for FEL intensities of 4.5×10^{12}, 3.5×10^{12}, 2.5×10^{12} respectively. This indicates a reasonable agreement with the spin-orbit averaged calculations, and a pattern of decreasing β_2 parameter with increasing FEL intensity can be observed.

Referring to the same theoretical work, a $\beta_4 \approx -0.1$ was reported for the spin-orbit averaged case. Again by performing a simple averaging in our results, we obtain β_4 values of -0.13, -0.10, -0.03 for FEL intensities of 4.5×10^{12}, 3.5×10^{12}, 2.5×10^{12} respectively.

Our spin-orbit averaged anisotropy parameters seem to be in agreement with the previously reported theoretical work. However, since our experiment allows for distinguishing between the different spin-orbit components in both the first and second ionization steps, further calculations are required to form a plausible explanation of

the experimental findings. Such theoretical work is currently being carried out by Grum-Grzhimailo and his coworkers in order to allow for a quantitative explanation of the observations.

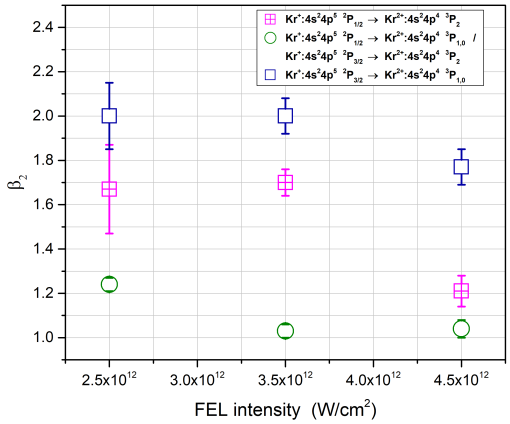

(a)

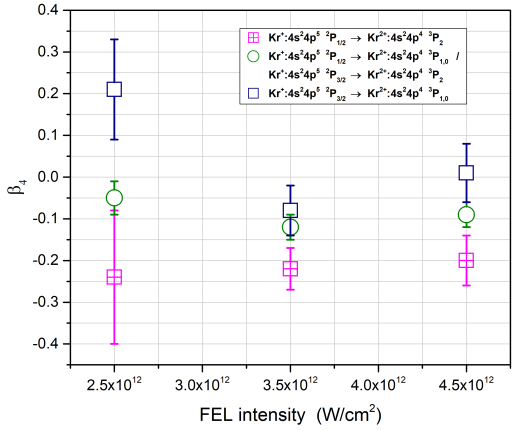

(b)

Figure 4.15: Anisotropy parameters for the open channels pertaining to the second step of the two-photon double ionization (a) The β_2 anisotropy parameter for three different FEL intensities. (b) The β_4 anisotropy parameter for the same three FEL intensities.

4.7 Summary

To summarize, in this chapter we reported experimental results concerning the two photon double ionization of Kr irradiated by FEL pulses at 25.2 eV. Our findings exhibit reasonable agreement with previously reported theoretical calculations, when the spin-orbit averaged case is considered. Theoretical work is currently being undertaken in order to obtain insight into the spin-orbit split state dependent characteristics of the sequential two photon ionization process.

Chapter 5

Low temperature photoionized plasmas

X-ray absorption spectroscopy is the lens through which we obtain information on molecular structure. Indeed, the atomic specificity manifested in the K-edge absorption spectra of metals in the hard X-ray region, carries valuable information on their electronic structure and the local coordination environment. For example, L-edges of the 3d transition metals (Mn, Fe, Co, Ni, Cu, Zn) exhibiting catalytic properties, lie in the soft X-ray (SXR) region ($0.4 \sim 1\ keV$) and can be probed via the $2p^6 3d^n \longrightarrow 2p^5 3d^{n+1}$ transition (see review [129]). Of particular importance is the spectral region ranging from the carbon K-shell absorption edge ($284.2\ eV$) to the the oxygen K-shell absorption edge ($543.1\ eV$). In this spectral region, carbon, oxygen and nitrogen in cell tissues exhibit strong absorption whereas the neighboring water environment is transparent allowing for high-contrast biological imaging.

To date, large scale facilities such as third generation synchrotrons or free electron lasers (FELs) are the primary sources of SXR radiation. More specifically, progress on the free electron lasers (FEL) technology, has resulted in soft X-ray (SXR) pulses of high brightness and ultrashort duration [93]. Having highlighted the undeniable advantages provided by the FEL sources, one should also consider the drawback of limited accessibility for external users. Alternatively, emission of radiation in the water-window region can be produced by table-top sources based on the high harmonic generation (HHG) process [130, 131], but at the expense of conversion efficiency.

Following a different approach, SXR radiation can be generated by laser produced plasma (LPP) sources. This cost-effective scheme implemented in our experiment is based on focusing the output of a Q-switched Nd:YAG laser into a double stream gas puff target, serving as an active medium for the generation of radiation in the water-window region [75]. In this geometry, a low Z gas is used to confine a high Z target gas, allowing for the formation of a gas puff target with high density at a larger distance from the nozzle. This approach, led to a conversion efficiency as high as ~ 0.42 percent for a wavelength of $13.5\ nm$ [76].

Previously reported studies have demonstrated the feasibility of creating and/or probing low temperature photoionised plasmas with XUV and SXR radiation from gas puff based LPP sources. Emission studies in the range of $10 - 20\ nm$ were performed in Ne [132], irradiated by EUV photons (centered around 11 nm) generated by the Kr/Xe double gas puff target. The same experiment was repeated using the Xe/Ne double gas puff target to record emission spectra of Ne in the UV/VIS region [133]. Similar spectroscopic investigations were conducted in He [134] and Kr [77], where emission spectroscopy was complemented by absorption measurements. The aforementioned studies were expanded to include molecular plasmas, namely N_2 [135] and SF_6 [136] for which emission spectra were recorded in the VUV and UV/VIS range. In addition, temporal measurements of the emission from ionic atomic and molecular species were reported [137].

Low temperature photoionized plasmas constitute a very unique state of matter. Neutral atoms and molecules, radicals, ions and electrons are present when radiation in the soft X-ray region is focused into a dense gas medium. Contrary to the case of plasma formation directly by the optical laser, the SXR photon energy is high enough to ensure the release of core and valence electrons. Consequently, lower intensities are required for plasma creation, resulting in thermal electron temperatures on the order of 1 to 2 eV [136]. The domain of low temperature plasmas is particularly interdisciplinary and brings together several different research fields, extending from atomic and molecular physics, material and surface science, chemistry, to even biology and medicine (see review [138]). In addition, photoionized plasmas are commonly encountered in astrophysics (see for example [139]). A typical example concerns plasmas generated in irradiated accretion disks around compact astrophysical objects such as neutron stars, black holes, or white dwarfs.

This chapter is dedicated to soft X-ray absorption measurements on CH_4 and CO_2 neutral or 'not ionized' gases and photoionized plasmas. Carbon dioxide is a major constituent of the terrestrial group (Mercury, Venus, Earth and Mars) whose atmospheric composition is by its very nature oxidizing (CO_2, O_2) whereas methane is abundant in the Jovian group (Jupiter, Saturn, Uranus and Neptune) whose atmospheric composition is reducing (H_2, CH_4, NH_3). Thus, photoabsorption studies on methane and carbon dioxide are very important for the field of astrophysical photochemistry.

5.1 Photoabsorption of molecules in the soft X-ray region

The inner (or even core) shell photoabsorption spectrum of molecules exhibits a structure which is remarkably rich [1] as may be seen in Figure 5.1. This is indeed a manifestation of the complicated electronic structure of molecules. When a soft

[1] Valence shell spectra are more complicated due to the delocalized nature of the valence electrons. In that case electron-electron correlations, screening effects and continuum-continuum coupling between ionization channels add up to form a particularly rich spectrum.

X-ray photon irradiates a molecule, the core orbitals come into play. Contrary to the valence orbitals, the core orbitals do not contribute to interatomic bonds since they are localized on each atomic site. Hence by tuning the SXR photon energy, site selectivity is feasible. The SXR photoabsorption process, involves a transition of a core electron to a valence and/or Rydberg unoccupied orbital. For K-shell excitation, the initial $1s$ state is of σ symmetry. Thus, dipole transitions are allowed for final states of σ or π symmetry, requiring the participation of an atomic p-orbital component in the final state. Characteristic is the presence of resonances in core-shell photoabsorption spectra in molecules. For low-z molecules, the π^*[2] antibonding orbital lies below the $1s$ ionization threshold. Thus $1s \longrightarrow \pi^*$ transitions give rise to a resonance peak in the low energy side of the spectrum. A so-called π^* resonance is only observed in molecules with a π bond. At higher energies of the spectrum, above the $1s$ ionization threshold, another type of resonance is observed. The so-named σ^* resonance arises from the transition of a $1s$ electron to a σ^* antibonding orbital. Despite lying above the ionization potential, this excited state survives against an instantaneous decay due to the centrifugal barrier in the shape of the molecular potential (see Figure 5.1). The height and shape of this barrier is dependent on the angular momentum of the final state. Thus, in the case of a σ^* shape resonance, specific components of the wavefunction are trapped along the internuclear axis. Alternative viewpoints, argued against the need for a potential barrier in order to form a plausible explanation of this continuum resonance. More specifically, Natoli [140] suggested that the resonance could be viewed as a result of multiple scattering of the electron by the atomic centers comprising the molecule. On the other hand, Sheehy and coworkers [141] described the resonance as a two-step one-electron process, involving the excitation of the K-shell electron in a virtual molecular orbital of σ^* symmetry followed by a photoelectron emission step. Independently of the framework chosen to interpret its origin, the high probability of decay of the quasibound state to continuum states results in a broader peak compared to the π^* resonance.

The energy range between the σ^* and π^* resonance, is spanned by Rydberg and/or mixed valence/Rydberg resonances. These features correspond to excitations of the core electrons to Rydberg and, in the presence of hydrogen atoms, to hydrogen derived orbitals mixed with Rydberg orbitals of the same symmetry[3]. These resonances are more intense in the carbon K-shell region compared to the oxygen K-edge. This is due to the decreased size of the $1s$ orbital in the latter case, resulting in a smaller spatial overlap. The aforementioned resonances, can be classified as one electron processes. Signatures of many electron processes such as shake-up or shake-off effects are absent in the spectral region below the molecular ionization potential. However, they might be observed in the spectral region above the molecular ionization potential.

[2]Henceforth the asterisk will be used as to denote an unoccupied molecular orbital.
[3]This mixing of the orbitals is possible for methane.

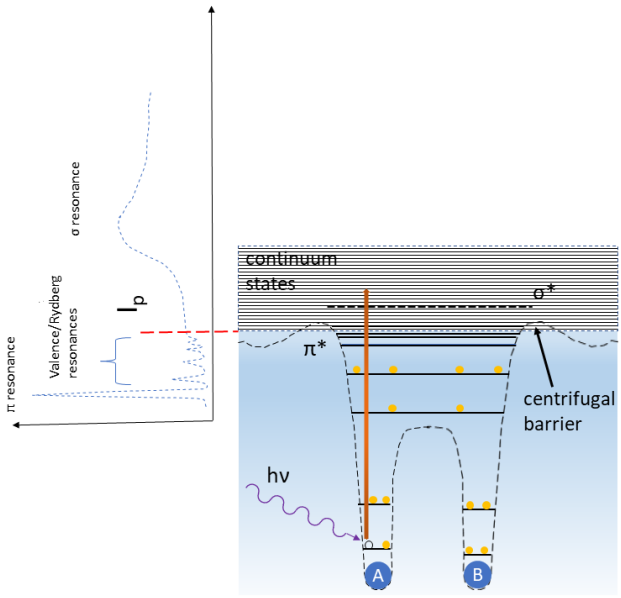

Figure 5.1: A schematic representation of the molecular potential for a diatomic molecule together with the corresponding K-shell x-ray absorption spectrum.

It is known that molecules lose their integrity after releasing their electrons. Thus, subsequent to the core electron excitation or ionization, molecular dissociation as a consequence of the relaxation process in the quantum system follows. The vast majority of fragmentation processes are governed by chemical forces, due to the remaining valence electron in the molecular ion. The only exception being the Coulomb explosion process whose mechanism is purely electrostatic. In Figure 5.2 we present a non exhaustive scheme involving the possible dissociation pathways for a triatomic molecule, following a core ionization step on one site. As seen in Figure 5.2 atomic and/or molecular ions are produced as a consequence of the molecular disintegration upon photoabsorption.

Since ions represent a major constituent of matter in the universe, they are in the spotlight due to their role in gas-phase chemistry of extraterrestrial space [142]. Ions are produced when synchrotron radiation emitted by stellar mass black holes or neutron stars create photoionized intestellar plasmas. With the aid of grating spectrographs on the Chandra and XMM-Neuton satellites, investigations of such photoionized plasmas in the soft X-ray region have become feasible. Thus acquisition of spectroscopic data in atomic and molecular ions is still a priority for researchers (see for example [143]).

From an experimentalist's standpoint, photoabsorption studies on atomic ions have been performed at synchrotrons using the merged beam technique [144]. In this arrangement monochromatized synchrotron radiation is merged with ions produced by a surface ionization source. This experimental approach has been widely applied in facilities such as Daresbury (UK) [145] and the Photon Factory [146] in Japan.

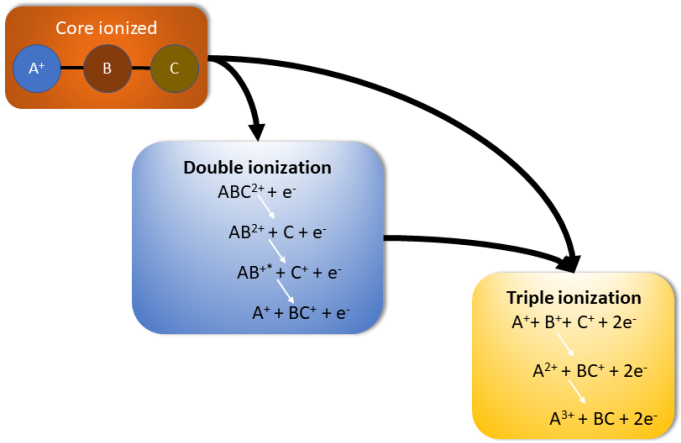

Figure 5.2: Possible dissociation processes following core hole creation in a triatomic molecule composed of three different atomic species. The scheme is restricted to double and triple ionization of the parent molecule. Higher degrees of ionization are also possible.

These early experiments, suffered from weak signal rates due to the low density of ionic species. The advent of third generation light sources paved the way for the permanent incorporation of merged beam setups at endstations in several facilities such at ALS [147], SOLEIL [148] and PETRA III [149].

Analogous photoabsorption studies in ionic species have been conducted by means of the dual laser plasma (DLP) technique [150]. The backlighting source is plasma emission, generated when high power laser pulses are focused onto solid targets. Pioneering work [151] carried out by Carillon and coworkers reported XUV absorption measurements in Al, using the DLP technique. The development of a DLP source covering the X-ray spectral range, allowed for an absorption study on the Al K-shell [152]. DLP has been proven a very useful tool for investigation of atomic ions [153], however DLP measurements in molecular species are rare in the literature [154, 155]. As high-temperature plasmas are generated in this technique, electron collisions contribute to the fragmentation process. In addition, molecular ions in excited states are expected to deexcite after the photodissociation of the parent molecule, long before the arrival of the time-delayed backlighting radiation. Thus photoabsorption studies of molecular ions in excited states seem challenging for the DLP scheme. However, the aforementioned difficulties are not present in the double gas puff target technique used here.

5.2 Experiment

The experimental setup is schematically depicted in Figure 5.3a together with some photographs of the setup in Figure 5.3b. The laser pulses were delivered by a commercial table top NL129 (EKSPLA) $Nd : YAG$ laser system emitting radiation at a wavelength of 1064 nm and a repetition rate of 10 Hz. The pulse energy was measured to be $\simeq 6.7\ J$ and a pulse duration measurement of $\simeq 1.6\ ns$ was obtained with the aid of a photodiode (see Figure 5.4).

A 10 cm focal length lens was used to focus the laser beam into a double stream gas puff target in order to generate the plasma. This gas puff target consists of two concentric nozzles: the inner nozzle has a diameter of $\simeq 0.4\ mm$ and the outer nozzle is ring-shaped with a diameter of $\simeq 0.7 - 1.5\ mm$. The two nozzles are driven independently by two electromagnetic actuators. The foundational idea behind this arrangement is that a low Z gas is used for confinement of a high Z gas. In our experiment we used two different inner gases, Kr and a mixture of Kr/Xe (90/10), while maintaining He as the outer gas. A representative emission spectrum for krypton and krypton/xenon (90/10) mix can be seen in Figure 5.5. It exhibits some discrete and strong emission features in the 300 - 350 eV photon energy range. For higher photon energies the spectrum is continuum-like, especially above 425 eV. As seen the emission spectral pattern is very similar for both the gas species used in the soft X-ray source. The molecular gases to be irradiated by the SXR radiation from the double gas puff plasma source are then injected into the vicinity of the LPP source by means of an additional valve $\simeq 2\ mm$ in diameter. In order to evacuate the two parts of the chamber we applied differential pumping, reaching a base pressure of $\simeq 10^{-4}\ mbar$. The radiation emitted by the LPP source can fulfill a two-fold role: first, it induces photoionization of the molecular gases and second, the continuous part serves as a backlighter for the photoionized plasmas.

The absorption spectra were recorded via a home-made spectrograph comprising a grazing incidence optical mount equipped with a Harada type grating as seen in Figure 5.6, (Hitachi High Technologies America Inc., Baltimore, MD, USA) [156, 157] with 2400 lines per mm, and a wavelength range extending from 1 nm to 5 nm. The most important technical characteristics of the grating are summarized in Table 5.1. For the detection of the spectra a back-illuminated CCD camera (Greateyes GmbH, Berlin, Germany) was placed after the diffraction grating. The camera has a chip with 2052×2046 pixels, the size of each pixel was $13 \times 13\ \mu m^2$. Throughout the experimental process, the chip was cooled down to $-40\ ^0\ C$ to reduce its internal noise and background.

In order to enhance the SXR emission, we optimized the performance of our source by varying several parameters. Firstly the gas puff target was arranged to be triggered before the arrival of the laser pulse. Two parameters were tweaked for each valve, the first one was the delay time to the laser pulse with respect to the instant of

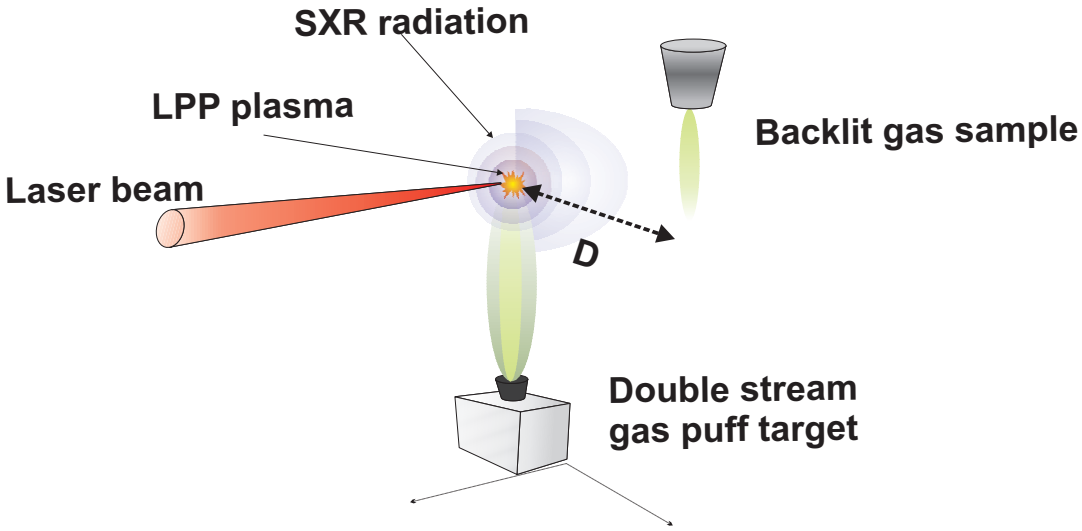

(a)

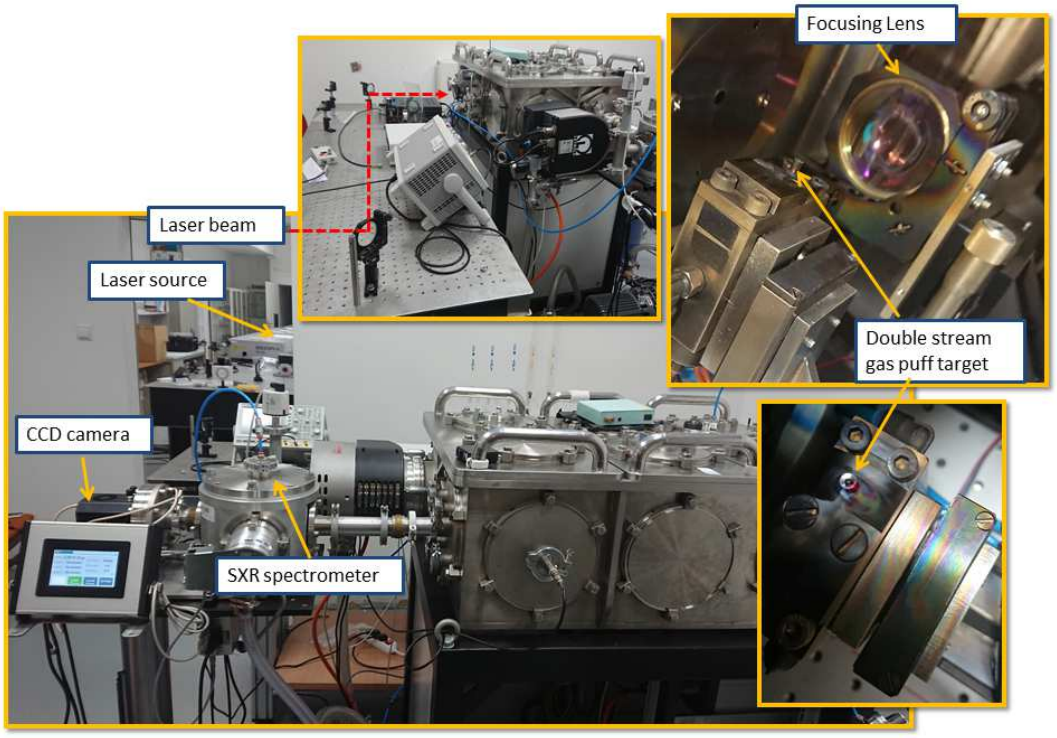

(b)

Figure 5.3: (a) Schematic diagram of the setup. The laser beam is focused onto the double stream gas puff target to generate soft X-ray radiation. The emitted radiation is then used to perform absorption measurements on a molecular gas target located at a distance (D) away from the source. (b) Photographs of the experimental setup.

Table 5.1: Tabulated main technical characteristics of the spectrometer grating

Grooves per mm	α (Degs)	β_1/β_2 (Degs)	$r/r^{'}$ (mm)	L (mm)	λ range (nm)
2400	88.7	-85.8/-81.0	237.0/235.3	20	1-5

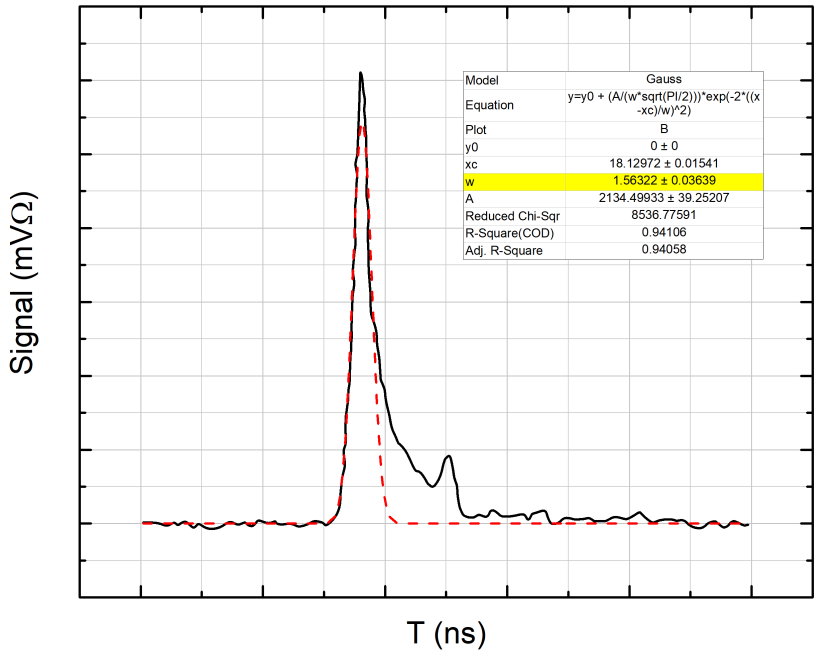

Figure 5.4: The time duration of the laser pulse. Assuming a Gaussian profile, the duration is estimated to be $\simeq 1.6\ ns$.

Table 5.2: Tabulated optimum experimental parameters

Gas species	T_{Delay} (μs)	Operating backing pressure (bars)
Kr	750	9
Kr/Xe	700	9
CO_2	500	4
CH_4	800	1
He	700	6

arrival of the valve trigger pulse and the second was the duration of the valve opening. In our case the duration of the valve opening was set at its maximum value as ($D = 1ms - T_{Delay}$), where D is the distance between the molecular sample under investigation and the double stream gas puff target. Hence the laser pulse delay times were optimized for both the inner and the outer gases of the double stream gas puff target and the optimum parameters are tabulated in Table 5.2. In addition the optimum operating backing pressures were determined by previous experience. More information regarding the timing and synchronization can be found in references [158, 79]. In addition, a more detailed description of this optimization process is presented in Appendix B.

Before proceeding to the experimental measurements, the wavelength calibration of the SXR spectrometer was performed. To do so, the emission spectrum of a gas

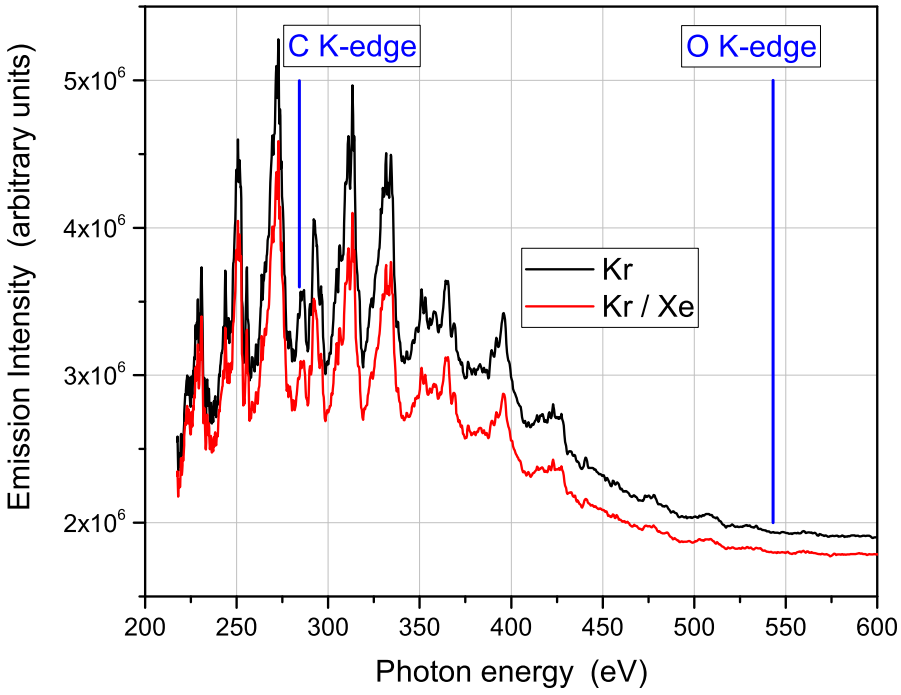

Figure 5.5: Emission spectrum including the spectral region between carbon and oxygen K-edge, for Kr and Kr/Xe (90/10) mixtures in the double stream gas puff source

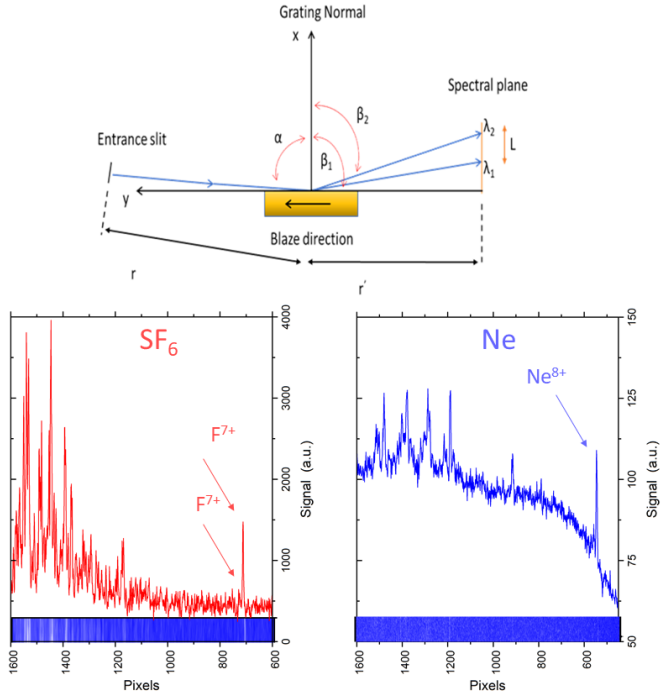

Figure 5.6: A Harada type grating, used in the home-made spectrograph in our setup. Atomic (Ne) and molecular gases (SF_6) were used to perform the wavelength calibration.

mixture composed of $N_2 : O_2 : Ar$ $(1 : 1 : 1)$ was used, in order to identify several emission lines as seen in Figure 5.7a. Hence, several lines associated with atomic ions were identified in the molecular plasma [159]. Specifically, for Ar^{8+} two lines were identified at 252.1 eV and at 254.5 eV, for N^{5+} two lines at 430.9 eV and 498.2 eV, and for O^{6+} one line at 574.0 eV. The spectral data were fitted to a quadratic equation (see Figure 5.7b), leading to the relationship below between the CCD pixel number and the corresponding photon energy (in eV):

$$y(x) = 2.69 \times 10^{-7}x^2 - 5.50 \times 10^{-3}x + 241.96 \tag{5.1}$$

where y is the photon energy in eV and x denotes the pixel index in the image recorded by the CCD camera.

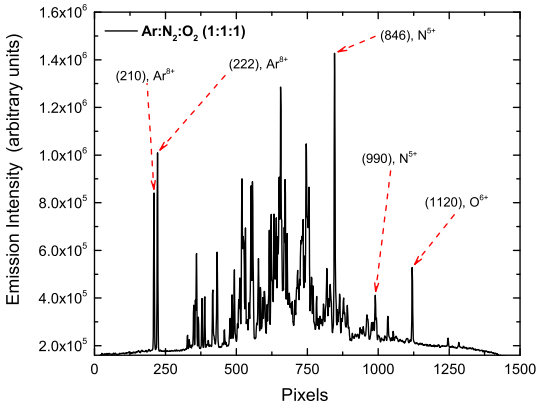

(a)

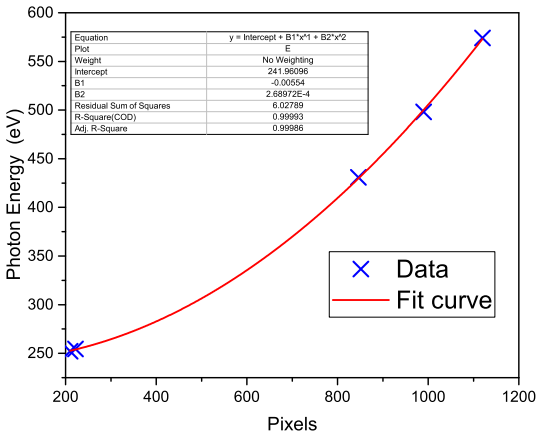

(b)

Figure 5.7: (a) Soft X-ray emission spectrum of the $N_2 : O_2 : Ar$ $(1 : 1 : 1)$ gas mixture. (b) the calibration curve of the spectrometer.

Then, the SXR emission spectra of Ne and SF_6 were recorded, as presented in Figure 5.8. From this spectrum, two emission lines for F^{7+} at 738.1 eV and at 723.0 eV, and a line of Ne^{8+} at 918.5 eV were identified. The resolving power of the spectrometer, with a 12 μm slit was determined by the isolated line at 281.5 eV, associated with the

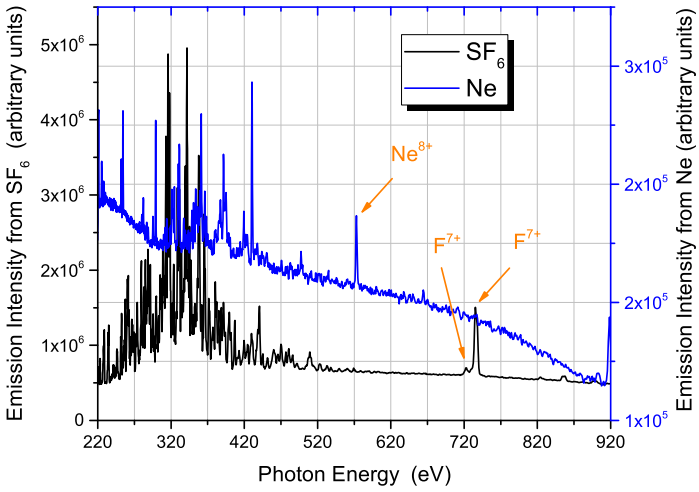

Figure 5.8: Soft X-ray emission spectrum of Ne and SF_6.

$2s^2 2p^2 3d - 2s^2 2p^3$ transition of S^{9+} ions in the SF_6 plasma. The FWHM for this line was measured as approximately 0.3 eV resulting in $\frac{E}{\Delta E} \simeq 900$.

5.3 Results and discussion

The soft X-ray absorption measurements were performed at two different distances, denoted as $D = 2\ mm$ and $D = 6\ mm$, between the double stream gas puff target and the single stream gas puff target under investigation. In addition, the sample gas target was moved several tens of centimeters away ($\approx$ 350 mm) to record the absorption spectrum of the so called 'not ionized' sample. Each spectrum represents the average of 10 laser shots and 10 such 10-shot averages were recorded.

5.4 Measurements on the carbon k-edge

In Figure 5.9a we present the soft X-ray absorption spectrum of carbon dioxide together with the relative oscillator strength for the same molecule obtained from the *Gas Phase Core Excitation Database [6]*. In this case the distance between the two valves was ca. 350 mm and one sees that the spectrum contains only absorption features due to the neutral 'not ionized' CO_2 molecule. From this spectrum, it was possible to identify several absorption features in agreement with previously reported absorption measurements performed at synchrotron facilities [160, 161, 162]. The $2\sigma_g(C1s)$ orbital in carbon dioxide is nondegenerate and of gerade symmetry, since the carbon atom lies on the center of the molecule. Thus $u \longrightarrow u$ transitions are dipole-allowed. Dipole forbidden transitions to Rydberg states ($1s \longrightarrow 3s, 4s$) can be observed as a consequence of the vibronic coupling.

Let us now turn our attention to the 'not ionized' CH_4. As before, the absorption spectrum closely resembles the absorption of the neutral methane as shown in Figure 5.9b. Several absorption features were identified in accordance with the previously reported synchrotron studies [163, 164, 165, 166]. Again a dipole forbidden transition ($1a_1 \longrightarrow 3sa_1$) is observed due to the Herzberg-Teller vibronic coupling. This dipole forbidden transition is weak compared to the ($1a_1 \longrightarrow 3pt_2$) transition to the first p-Rydberg orbital. The absorption spectra shown in Figure 5.9 were acquired using the krypton/xenon mixture as the medium to generate the soft X-ray radiation.

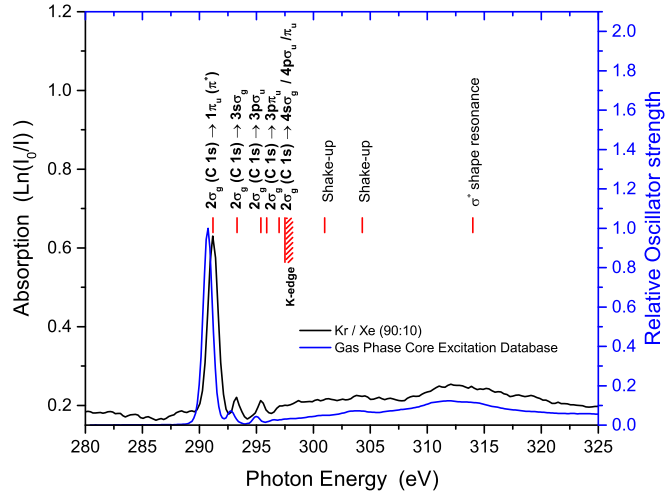

(a)

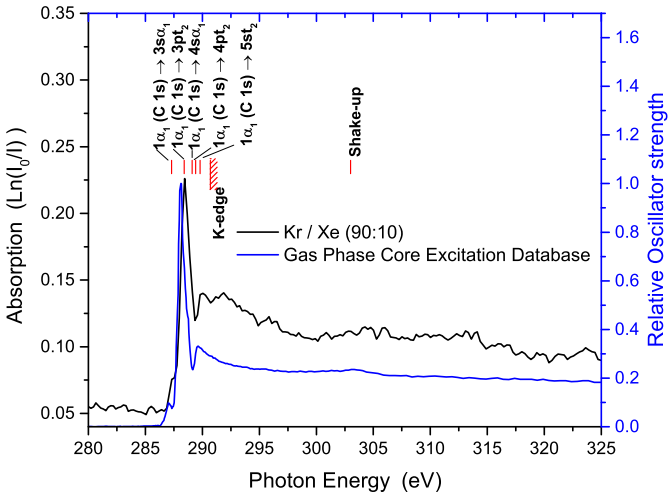

(b)

Figure 5.9: Experimental SXR absorption of the 'not ionized' (a) carbon dioxide and (b) methane plotted together with the normalized oscillator strength adapted from [6]. A gas mixture of xenon/krypton (90/10) was used as the medium to generate the soft X-ray radiation.

In Figure 5.10a and Figure 5.10c absorption measurements are presented for CO_2 and CH_4 respectively using the Kr/Xe gas target SXR source. The spectra shown are for SXR source to sample distances "D" of 2 mm, 6 mm and $\approx$ 350 mm. Several new features arise in the low energy region of the spectrum below the main absorption peak for both target molecules for distances of 2 mm and 6 mm between the SXR source and the sample gases. This pattern is also present when *Kr* alone is used as the inner gas for the SXR source as can be seen in Figure 5.10b and Figure 5.10d. The two different media (Kr and Kr/Xe) were used in the LPP source, in order to confirm the absence of artifacts in our spectrum stemming from the source itself.

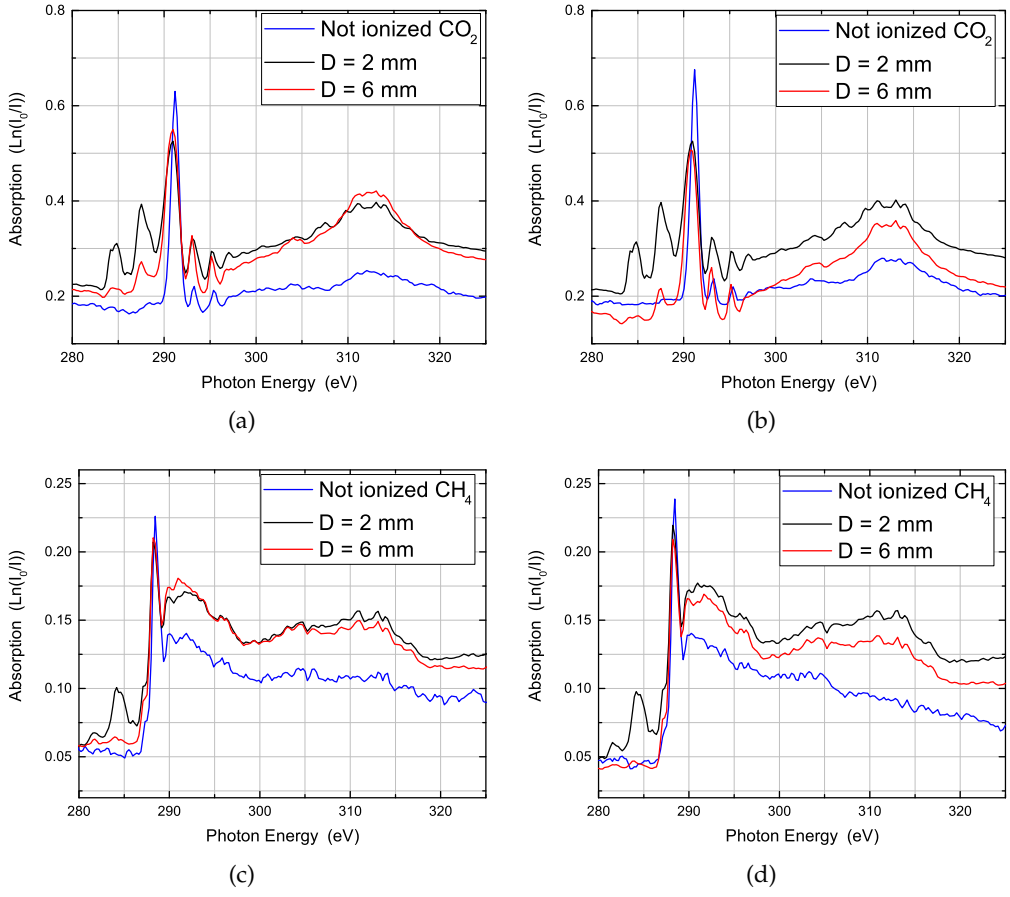

Figure 5.10: Absorption measurements in the vicinity of the carbon K-edge in CO_2 for three distances between the sample gas and the LPP soft X-ray source (a) using the Kr/Xe mixture and (b) using Kr in the double stream gas puff target. Corresponding spectra for methane (c) using the Kr/Xe mixture as the inner gas and (d) using Kr as the inner gas, in the double stream gas puff target.

The additional features observed should be attributed to molecular and atomic species, produced by photochemical events taking place in the photoionized molecular plasma. In order to confirm this assumption we used the Cowan suite of atomic structure codes to perform calculations. In addition, we used spectral data from the *Gas Phase Core Excitation Database [6].*

The features in the soft X-ray absorption spectrum of methane (Figure 5.11a) can be attributed to the CH_3 radical and the C atom. Specifically, the CH_3 radical might account for the structure at $\simeq 281 - 283\ eV$. This should involve an excitation of one core electron to the outer valence orbital. As previously reported [167] this transition is associated with the so-called 'umbrella motion' of the methyl radical. Similarly, absorption from atomic carbon could result in the features at $\simeq 284 - 286\ eV$. The presence of the methyl radical is not surprising as the predominant dissociation pathway for methane is $CH_4 + h\nu \longrightarrow CH_3^+ + H^+$ following a double ionization process in the SXR region where the photon energy is high enough to remove two electrons from the valence orbital ($1t_2$). Neutral carbon can also be formed via a many-body fragmentation process of the methane dication [168]. The two most energetically favoured pathways include a three body fragmentation of methane: $CH_4 + h\nu \longrightarrow C + H_3^+ + H^+$ or $CH_4 + h\nu \longrightarrow C + H_2^+ + H_2^+$.

In Figure 5.11b we present the normalized oscillator strength of CO obtained from the *Gas Phase Core Excitation Database [6]*, together with calculations performed by means of the Cowan code for the C atom and C^+ ion in the spectral region below 290 eV. As can be seen, the broad structure above $\simeq 287\ eV$ should be attributed to CO and C^+ whereas absorption from atomic carbon could result in the features at $\simeq 284 - 286\ eV$. The presence of CO in the absorption spectrum is a signature of the $CO_2^+ \longrightarrow CO + O^+$ dissociation pathway following the removal of an inner valence $4\sigma_g$ electron [169]. Similar to the case of methane, the presence of C and C^+ should be attributed to many-body fragmentation processes. Such a pathway, has been observed when carbon dioxide was irradiated by synchrotron radiation, tuned to wavelengths around the oxygen or carbon K-edge [170]. In that case, a triple ionization followed by the $CO_2^{3+} \longrightarrow C^+ + O^+ + O^+$ dissociation pathway was suggested as the plausible explanation for the C^+ signal. In addition, a more recent study at the ALS supported the $CO_2^{2+} \longrightarrow C^+ + O^+ + O$ pathway [171]. Undoubtedly, the most striking observation in our study, is the presence of states with an L-shell vacancy (core hole) in the C^+ ions. These states are then probed by a further photoabsorption step. The negligible time delay between the creation of the photoionized plasma and the absorption measurement along with the very short duration of the XUV pulse ensure that such states could only be created by photons from the laser plasma source and not particles which would reach the sample gas long after the XUV probe pulse has terminated. The aforementioned transitions, lying in the low energy region for both molecules, are tabulated in Table 5.3.

In relation to the effect of the source to sample separation, the SXR source can be considered as a point source, and thus its intensity scales as $\frac{1}{r^2}$. Hence when we move the gas target several tens of cm's away from the source, the SXR intensity

Table 5.3: Tabulated transitions for the CO_2 and CH_4 plasmas, including transitions in CH_3^+, CO, C, C^+ species.

Photon Energy (eV)	Molecular/Atomic species	Assignment
281.8	CH_3^+	$(1a_1^{'})(C1s) \longrightarrow (1a_2^{''})\ (0-0)$
282.2	CH_3^+	$(1a_1^{'})(C1s) \longrightarrow (1a_2^{''})\ (1-0)$
284.2	CI	$1s^2 2s^2 2p^2(^1S)^3P \longrightarrow 1s^1 2s^2 2p^3(^4S)^3S$
284.3	CI	$1s^2 2s^2 2p^2(^1S)^3P \longrightarrow 1s^1 2s^2 2p^3(^2D)^3D$
284.5	CI	$1s^2 2s^2 2p^2(^1S)^1D \longrightarrow 1s^1 2s^2 2p^3(^2D)^1D$
285.9	CI	$1s^2 2s^2 2p^2(^1S)^3P \longrightarrow 1s^1 2s^2 2p^3(^2P)^3P$
286.2	CI	$1s^2 2s^2 2p^2(^1S)^1D \longrightarrow 1s^1 2s^2 2p^3(^2P)^1P$
287.1	CII	$1s^2 2s^1 2p^2(^4S)^4S \longrightarrow 1s^1 2s^1 2p^3(^3P)^4P$
287.2	CII	$1s^2 2s^1 2p^2(^2P)^2P \longrightarrow 1s^1 2s^1 2p^3(^1S)^2S$
287.4	CII	$1s^2 2s^1 2p^2(^2D)^2D \longrightarrow 1s^1 2s^1 2p^3(^3P)^2P$
287.7	CII	$1s^2 2s^1 2p^2(^2D)^2D \longrightarrow 1s^1 2s^1 2p^3(^1D)^2D$
287.8	CII	$1s^2 2s^2 2p^1(^1S)^2P \longrightarrow 1s^1 2s^2 2p^2(^1D)^2D$
287.9	CII	$1s^2 2s^2 2p^1(^1S)^2P \longrightarrow 1s^1 2s^2 2p^2(^3P)^2P$
288.2	CII	$1s^2 2s^1 2p^2(^2D)^4D \longrightarrow 1s^1 2s^1 2p^3(^3P)^4P$
287.4	CO	$2\sigma(C1s) \longrightarrow 1\pi_u$, *$\pi$ resonance*

at the gas sample location drops significantly and the degree of photoionization becomes negligible. In order to estimate the degree of photoionization at short distances between the SXR source and the molecular sample we make use of the Beer-Lambert law. Specifically, the signal presented in each photoabsorption spectrum corresponds to the quantity $Ln\frac{I_0}{I}$, which equals the total photoabsorption cross section of the molecule under investigation multiplied by the column density (NL) in cm^{-2}. Thus the integrated signal of the main carbon 1s absorption peak should be representative of the number of ('not ionized', i.e., neutral) molecular absorbers. In the case of higher laser powers, this signal is decreased, due to the decrease in the number density of neutral absorbers by the ionization that occurs as the SXR pulse passes through the methane or carbon dioxide gas. The relative decrease is hence indicative of the degree of photoionization. Using this argument for a distance $D = 2$ mm between the SXR source and the molecular target, we estimate values of 30 % and 15 % for the degree of photoionization of CO_2 and CH_4 photoionized plasmas respectively.

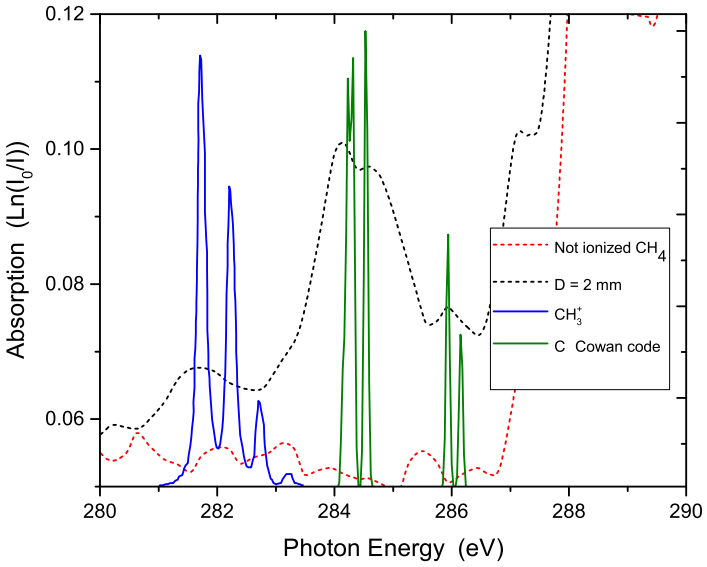

(a)

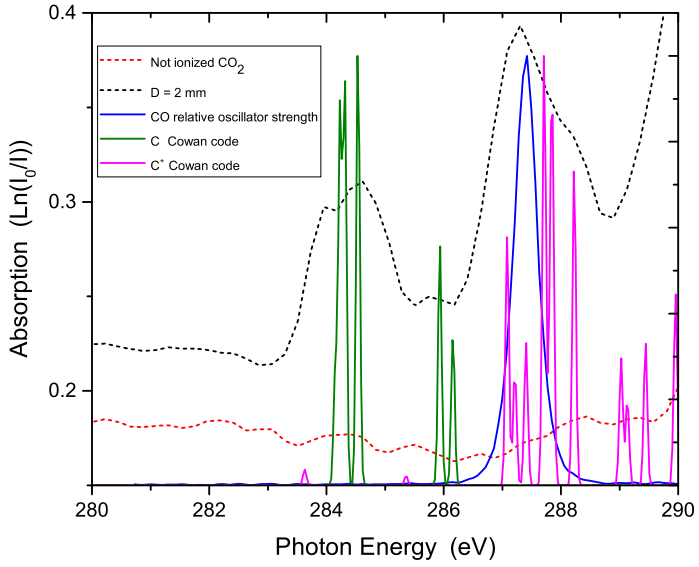

(b)

Figure 5.11: Experimental SXR absorption of the neutral or 'not ionized' (a) carbon dioxide and (b) methane, in the vicinity of the carbon K-edge plotted together with the normalized oscillator strength adapted from [6]. In addition, the corresponding SXR absorption spectra for a distance $D = 2\ mm$ between the sample gas and the LPP soft X-ray source are shown. A gas mixture of xenon/krypton (90/10) was used as the medium to generate the soft X-ray radiation.

5.5 Measurements on the oxygen k-edge

Figure 5.12 shows the absorption spectrum of the neutral (or 'not ionized') carbon dioxide in the vicinity of the oxygen K-edge along with the oscillator strength for the same molecule, acquired from the *Gas Phase Core Excitation Database [6]*. The close resemblance of the two curves precludes the presence of any molecular and/or atomic species other that CO_2. A comparison with previously reported synchrotron measurements [160, 172] yields the identification of several absorption features below the ionization threshold. More specifically, we observe transitions from the nearly degenerate $(1\sigma_g,\ 1\sigma_u)(O(1s))$ pair of orbitals to several final states of gerade and/or ungerade symmetry. One may also notice the weaker peaks corresponding to valence/Rydberg resonances as compared to the carbon K-edge due to the decreased size of the $1s$ orbital.

Upon decreasing the distance between the Kr/Xe double stream gas puff target and the CO_2 sample down to $D = 6\ mm$ and subsequently to $D = 2\ mm$, new features appear to the low energy region of the spectrum as presented in Figure 5.13b. Prominent also is the feature in the low energy side of the main absorption line at around 535 eV. Analogous spectral patterns, may be observed in Figure 5.13a for the Kr double stream gas puff target for the soft X-ray source. Consequently, source-related spectral artifacts could not be held responsible for the aforementioned features.

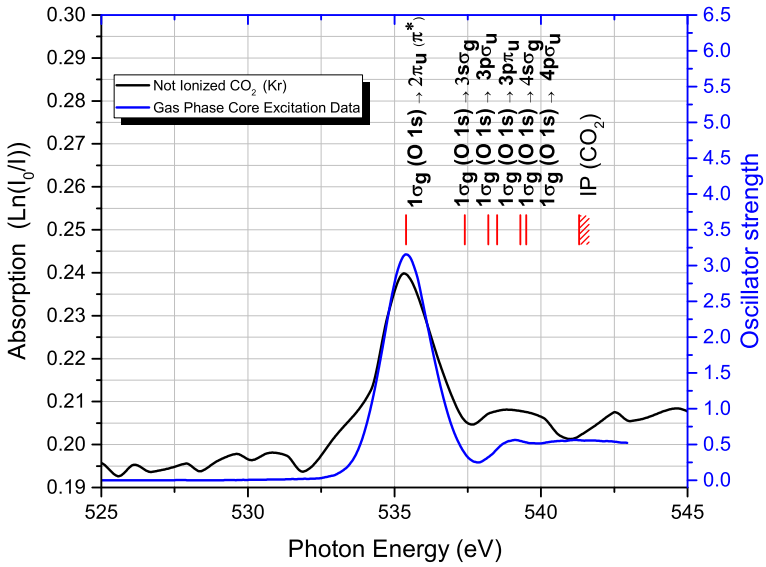

Figure 5.12: Photoabsorption spectrum of the 'not ionized' or neutral CO_2 sample gas in the oxygen K-edge spectral region, shown together with the oscillator strength for the carbon dioxide molecule. Krypton gas was used in the soft X-ray source.

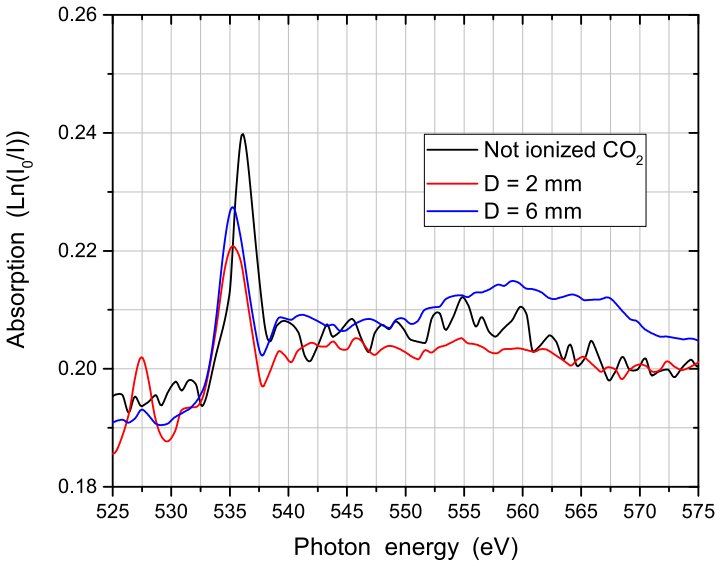

(a)

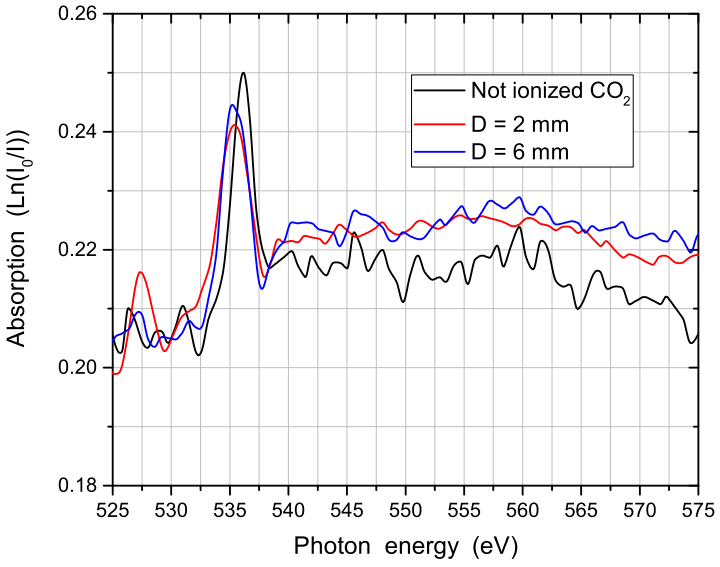

(b)

Figure 5.13: Absorption spectra in the vicinity of the oxygen K-edge in CO_2 for three different distances with respect to the LPP soft X-ray source (a) using Kr and (b) using the Kr/Xe mixture in the double stream gas puff target.

The features in the low energy region of the spectrum indicate the presence of various molecular and/or atomic species, in addition to original neutral CO_2 gas sample in the photoionized plasma. Hence the question remains open regarding the identification of the species in our spectra. In fact, the reaction pathways could provide

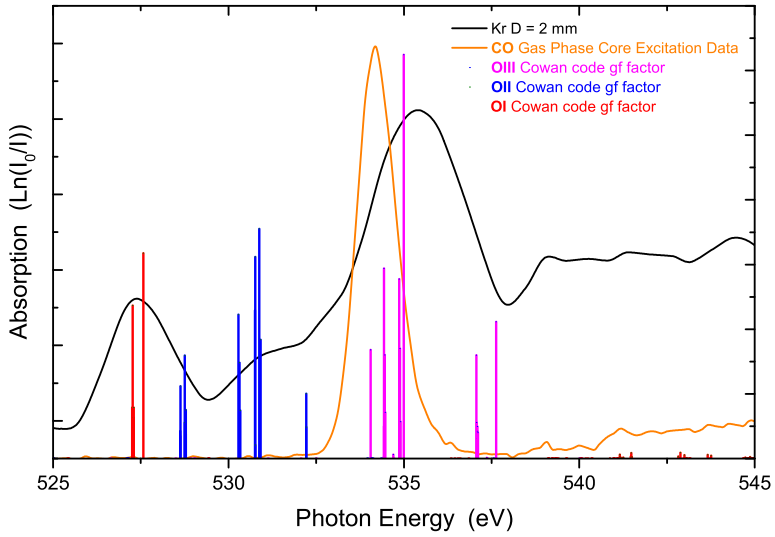

Figure 5.14: Absorption spectrum of CO_2 in the vicinity of the oxygen K-edge for a distance of 2 mm with respect to the LPP soft X-ray source using the Kr/Xe mixture, plotted together with Cowan code calculations [7, 8] for the O, O^+ and O^{2+} species. In addition, oscillator strength data of the CO molecule acquired from the Gas Phase Core Excitation Database are shown [6]. The spectral features in the low photon energy region of the photoabsorption spectrum of the ionized carbon dioxide plasma can be attributed to these species.

valuable information: the $CO_2^+ \longrightarrow CO + O^+$ dissociation pathway following the removal of an inner valence $4\sigma_g$ electron [169] could result in CO and O^+ signals in our absorption spectra. In addition, a recent study at the ALS source [171] supports the $CO_2^{2+} \longrightarrow C^+ + O^+ + O$ pathway, whereas O^{2+} fragments were also observed [173].

According to the above-mentioned reaction pathways the O atom, O^+, O^{2+} ions and CO molecular ion are the main products of the CO_2 fragmentation in the photoionized plasma. Thus, signatures of these fragments are likely to be observed. In order to verify them Figure 5.14 shows the absorption spectrum of the photoionized carbon dioxide plasma together with calculations performed by means of the Cowan code [7, 8, 174] for the O atom and O^+, O^{2+} ions. In this case, the experimental data are compared with the weighted oscillator strengths (g_f factors). The most important of these transitions are tabulated in Table 5.4. In addition, the transition $1\sigma(O(1s)) \longrightarrow 2\pi$ in a CO fragment, should contribute to the spectrum particularly in the spectral region around 535 eV [160].

Using these results, the absorption features in the low energy spectral region could unambiguously be attributed to $1s^2 2s^2 2p^4 \rightarrow 1s^1 2s^2 2p^5$ transition array in neutral oxygen, the $1s^2 2s^2 2p^3 \rightarrow 1s^1 2s^2 2p^4$ transitions in O^+ and the $1s^2 2s^2 2p^2 \rightarrow 1s^1 2s^2 2p^3$

Table 5.4: Tabulated transitions for the CO_2 plasma, including transitions in O, O^+, O^{2+} species.

Photon Energy (eV)	Atomic species	Assignment
527.3	OI	$1s^2 2s^2 2p^4 (^1S)^3P \longrightarrow 1s^1 2s^2 2p^5 (^2S)^3P$
527.6	OI	$1s^2 2s^2 2p^4 (^1S)^1D \longrightarrow 1s^1 2s^2 2p^5 (^2S)^1P$
530.3	OII	$1s^2 2s^2 2p^3 (^1S)^4S \longrightarrow 1s^1 2s^2 2p^4 (^3P)^4P$
530.8	OII	$1s^2 2s^2 2p^3 (^1S)^2D \longrightarrow 1s^1 2s^2 2p^4 (^1D)^2D$
530.9	OII	$1s^2 2s^2 2p^3 (^1S)^2D \longrightarrow 1s^1 2s^2 2p^4 (^3P)^2P$
534.4	$OIII$	$1s^2 2s^2 2p^2 (^1S)^3P \longrightarrow 1s^1 2s^2 2p^3 (^2D)^3D$
534.9	$OIII$	$1s^2 2s^2 2p^2 (^1S)^3P \longrightarrow 1s^1 2s^2 2p^3 (^4S)^3S$
535.0	$OIII$	$1s^2 2s^2 2p^2 (^1S)^1D \longrightarrow 1s^1 2s^2 2p^3 (^2D)^1D$
537.6	$OIII$	$1s^2 2s^2 2p^2 (^1S)^1D \longrightarrow 1s^1 2s^2 2p^3 (^2P)^1P$

transitions in O^{2+} fragments. Hence our findings suggest the presence of $1s \rightarrow 2p$ excitations in oxygen species produced as carbon dioxide fragments upon soft X-ray photoabsorption. The role of $1s \rightarrow 2p$ autoionizing resonance in the O^+ spectrum has been highlighted in a previous study at Spring-8 [175]. In our case, the $1s \longrightarrow 2p$ excitation in O^{2+}, along with the $1\sigma(O(1s)) \longrightarrow 2\pi$ excitation in CO could also explain the shift and spectral broadening observed for the main absorption feature at short distances between the SXR source and the CO_2 gas target. Following the same arguments as in the carbon K-edge case, we estimate the degree of ionization at $D = 2\ mm$ as being approximately 20 % when Kr or Kr/Xe (90/10) mixture is used in the SXR source respectively.

5.6 Summary

To conclude, in this chapter soft X-ray photoabsorption measurements around carbon and oxygen K-edges in CO_2 and CH_4 gas targets were reported. The measurements revealed significant differences in the spectra of neutral ('not ionized') molecules, compared to the photoionized plasmas. Specifically, signatures of C^+, C^{2+}, O^+, O^{2+} in the soft X-ray spectra of carbon dioxide and methane photoionized plasmas respectively were revealed. These observations were supported by calculations performed by means of the Cowan suite of atomic structure codes. Such astrophysically important ions have been extensively studied in the EUV range [176, 177, 178, 179] by means of either the DLP or the synchrotron - ion merged beam technique, however only a few studies have been reported in the soft X-ray spectral region [180, 181].

Chapter 6

Molecules irradiated by intense laser fields ($\omega/2\omega$)

6.1 Molecules in Intense laser fields

Molecular spectroscopy has been a field of active research for the last two centuries. In 1834 D.Brewster observed the absorption spectrum of NO_2 illuminated by sunlight which was dispersed by a prism [182]. Later on, in 1887, Rowland's pioneering work resulted in optical diffraction gratings with enhanced capabilities allowing for measurements with significantly enhanced spectral resolution [183]. Thus characteristic spectra of several, mainly small, molecules were acquired. However it soon became obvious that experimental techniques such as absorption and emission spectroscopy in combination with incoherent light sources, available at that time, were insufficient to ensure further progress in molecular spectroscopy. It was the invention of the laser, in 1960, that heralded a new era allowing for spectroscopy with unprecedented high resolution.

Given their well defined wavelength, lasers were initially used to reveal the electronic structure of small quantum systems. Consequently, they were used to stimulate transitions between atomic states having narrow bandwidths. In addition, dye lasers were extensively used for probing molecular structure due to their wavelength tunability. When one refers to spectroscopic applications, lasers could be considered as a perturbation allowing for the characterization of the field-free properties of the system under inspection.

Over the passage of time, laser technology progressed significantly resulting in shortening of the pulse duration by several orders of magnitude as can be seen in Figure 6.1. In fact, the field termed 'ultrafast' optics refers to laser pulses whose duration is on the same order as the vibrational period ($\simeq 10^{-14}s$) of lighter molecules such as H_2. In that case, high peak power densities became available due to the efficient concentration of (even low) pulse energies into a very short interval of time.

The advent of the ultrafast era was accompanied by a change in the use of lasers. Now, instead of being the spectroscopic tool for observing the structural properties

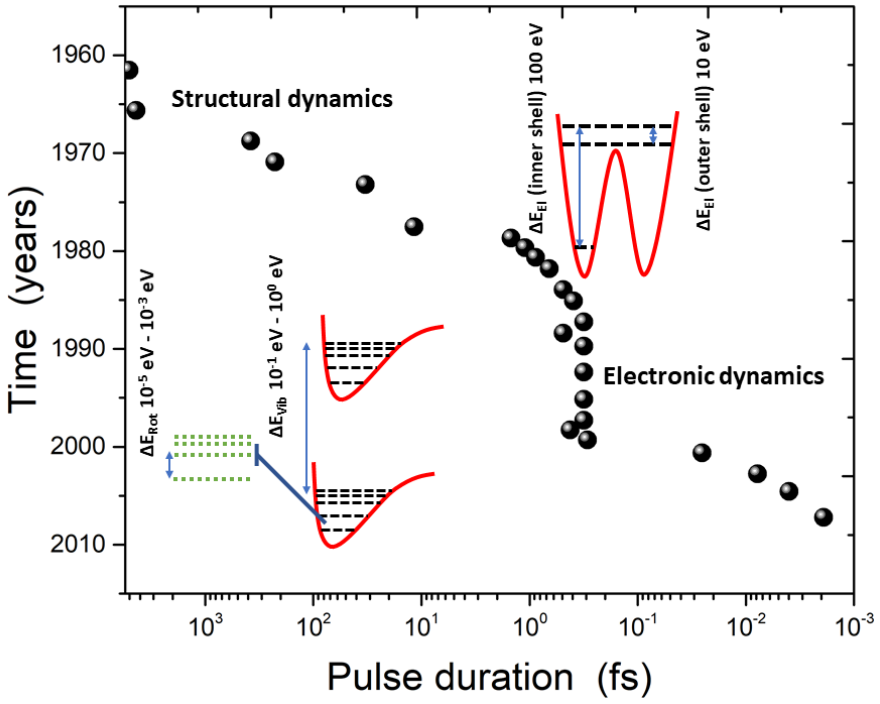

Figure 6.1: Evolution of the shortest attainable pulse duration over the passage of time.

of the small quantum systems, it permitted one to not just study, but, and importantly, to also , influence their dynamics. For example current applications of ultrafast lasers include the preparation of Rydberg atoms, coherent control and the steering of photo-processes including ionization and chemical reactions [184, 185].

According to quantum mechanics, for a particle in a superposition of two quantum states, an initial state of energy E_i and a final one of energy E_f, the solution of the Schrodinger equation leads to an oscillatory behavior with a period $T_{osc} = \frac{2\pi\hbar}{\Delta E}$, where $\Delta E = E_f - E_i$. Thus, a larger energy separation between the energy states leads to a faster motion of the particle. Given that the energy separation is determined by the spatial confinement of the system, the rapidity of the transition is also related to the spatial extension of the system. In the case of molecules structural dynamics such as molecular rotations or vibrations occur on much longer timescales compared to electronic dynamics which are more confined in space (see Figure 6.1). Hence, ultra-short pulse durations on the femto- and attosecond timescales are essential for elucidating electronic dynamics in molecules compared to vibrational and/or rotational excitations.

Small quantum systems are likely to survive the steep rise of intensity in the case of ultrafast laser fields thus allowing for the observation of highly charged ions. On the other hand when the temporal gradient on the leading edge of the laser pulse is less steep, saturation effects dominate. This is the reason for observing the I_2^{3+} ions upon irradiation by ultrafast laser fields in contrast to laser fields of nanosecond duration

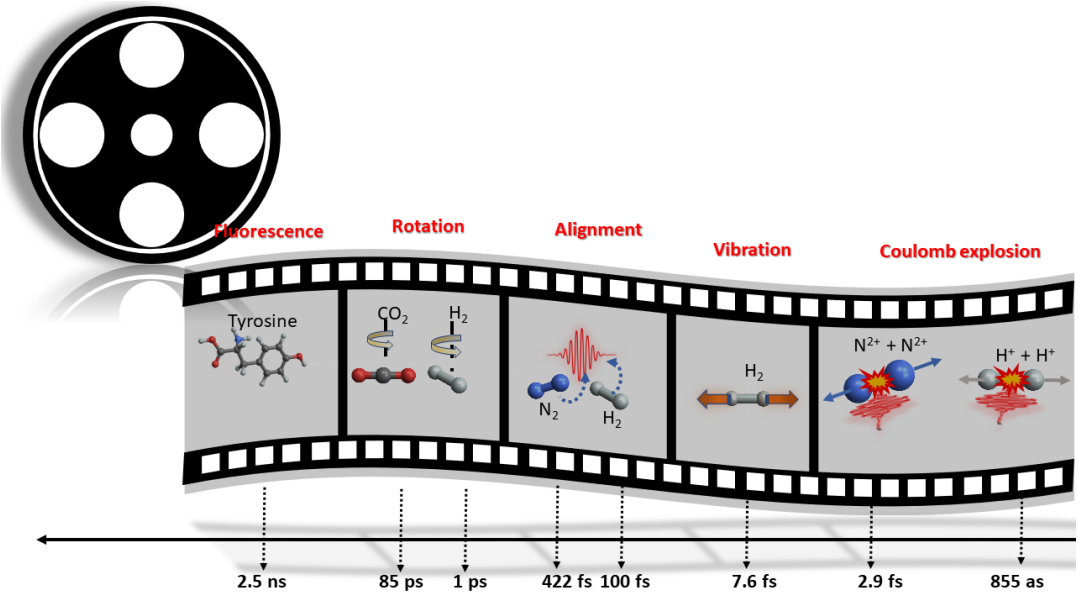

Figure 6.2: Characteristic timescales of the most fundamental physical processes observed when molecules are irradiated by ultrashort laser pulses.

where only lowly charged molecular ions can be formed [186].

Figure 6.2 attempts to elucidate the characteristic timescales involved in the interaction of small molecules with ultrafast laser pulses. We can see that the fluorescence of a heavy molecule like Tyrosine lasts approximately 2.5 ns, the field free rotational period for a linear triatomic molecule (CO_2) is approximately 85 ps whereas for a lighter H_2 molecule it is below 1 ps.

When molecules are irradiated by laser fields, they tend to align along the direction of the laser polarization. In that case, the laser field exerts a torsion on the molecule. This field induced motion exists on a timescale of hundreds of femtoseconds. Concerning the molecular vibrations, they take place within tens of femtoseconds. The fragmentation process is the fastest one, since it is governed by the Coulomb repulsion. Thus assuming a pure Coulomb repulsion, the characteristic time for dissociation of $N_2^{4+} \longrightarrow N^{2+} + N^{2+}$ is 2.9 fs and the corresponding time for the Coulomb explosion of $H_2^{2+} \longrightarrow H^+ + H^+$ is 855 attoseconds.

6.2 Experimental setup

The laser installed in the SQS laboratory at the European XFEL GmbH is a Ti:sapphire system incorporating two amplification stages. This arrangement provided high average power (10 W) along with pulses of ultrafast duration ($\sim$ 35 fs measured with a FROG autocorrelator) at a repetition rate of 3 KHz. The wavelength is centered at 800 nm. A long focal length 1400 mm lens, followed by a 500 mm gold coated, toroidal mirror, were used to focus the laser beam down to 50 μm beam waist in

the interaction region. The laser was incident on the focusing mirror at angle of approximately $\sim$ 72 *degrees*. In order to facilitate intensity dependent measurements, an attenuator was used. It comprised a half wave plate followed by two polarizers set at an angle of incidence of $\sim$ 72 Degrees. Initially, the laser field is polarized in the horizontal direction. However, it acquires a vertical component after passing through the half waveplate. Then, the vertical component is reflected by the two polarizers whereas the horizontal component is transmitted and blocked by a beam block placed right after the attenuator. Thus, the laser intensity was controlled by rotating the half wave plate in order to increase/decrease the vertical component field strength. The gas target was injected by means of a effusive gas needle. The chamber was pumped down to a base pressure of 1×10^{-9} *mbar*. A typical operating pressure was on the order of 1×10^{-8} *mbar*, low enough to minimize any contribution to the signals coming from space charge effects in the interaction region.

6.2.1 The time of flight (TOF) spectrometer

The measurements presented in this chapter, were taken using the TOF spectrometer housed in the SQS chamber (see Figure 6.3). According to the underlying principle of TOF spectroscopy, a particle's time of flight over a fixed and well defined distance is representative of the mass to charge ratio for this charged particle. As can be seen in Figure 6.3, the spectrometer used in our experiments, follows the Wiley-McLaren design [187] with the addition of an electrostatic lens. This so called Einzel lens is mainly added so that the spectrometer can also operate as an electron TOF. Furthermore in Figure 6.3, one also notices a VMI spectrometer on the other end of the vacuum chamber. Thus, in this arrangement, the VMI repeller serves as the TOF extractor and the VMI extractor as the TOF repeller. The alignment of the focus position with respect to the entrance slit of the spectrometer was achieved by means of a YAG screen moved into the interaction region. The resolution of the TOF spectrometer is high enough to distinguish between the different mass isotopes of Xe atoms as seen in Figure 6.4.

For the $\frac{m}{z}$ to TOF calibration of the instrument we used several known peaks (Xe^+, Xe^{2+}, N_2^+, H_2O^+). The $\frac{m}{z}$ values of these peaks are plotted against the square of their experimental times of flight in Figure 6.5. Then in order to calibrate the instrument we perform a least squares fitting with a relationship of the form :

$$\frac{m}{z} = A \times T^2 + B \tag{6.1}$$

In Figure 6.5 one sees the extracted values for the slope and intercept, together with data points obtained by simulations using SIMION commercial software [188]. The results suggest that the experimental values are in good agreement with the values generated by the simulation.

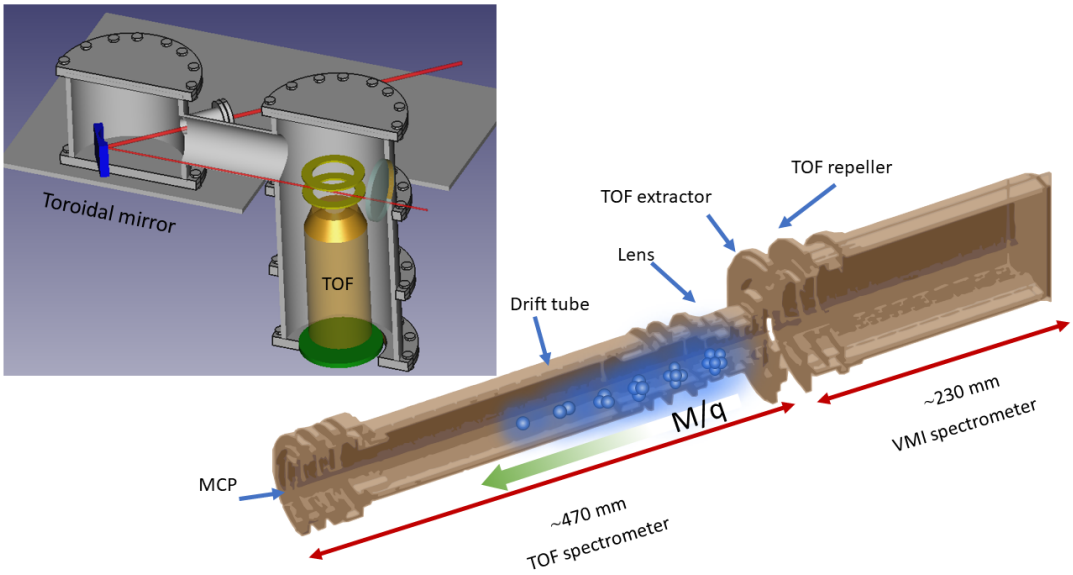

Figure 6.3: A three-dimensional representation of the experimental setup, together with a schematic of the TOF spectrometer.

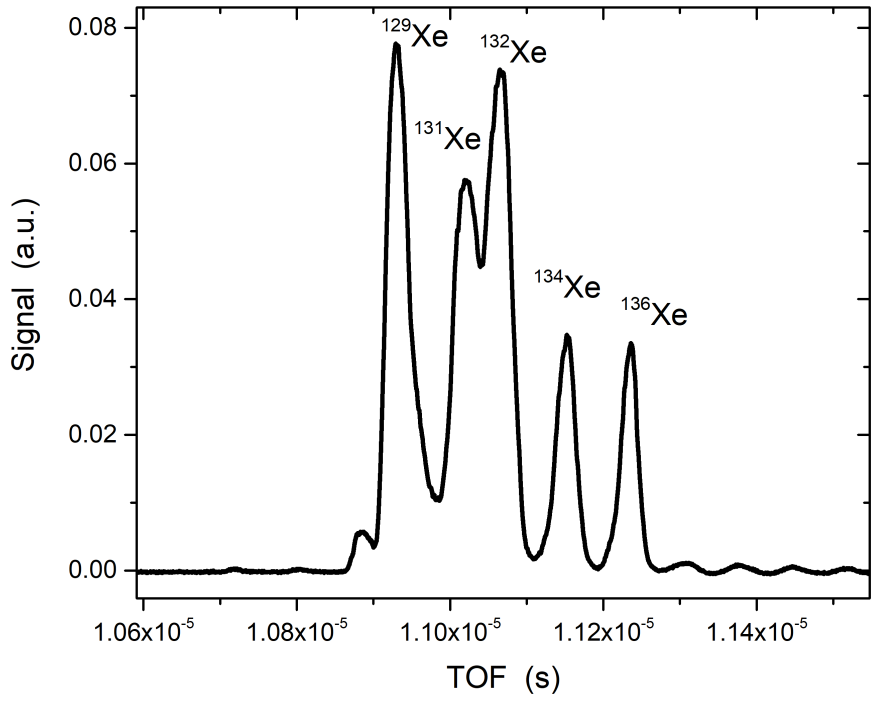

Figure 6.4: TOF spectrum in the region of the Xe isotopes, used for the calibration of the spectrometer.

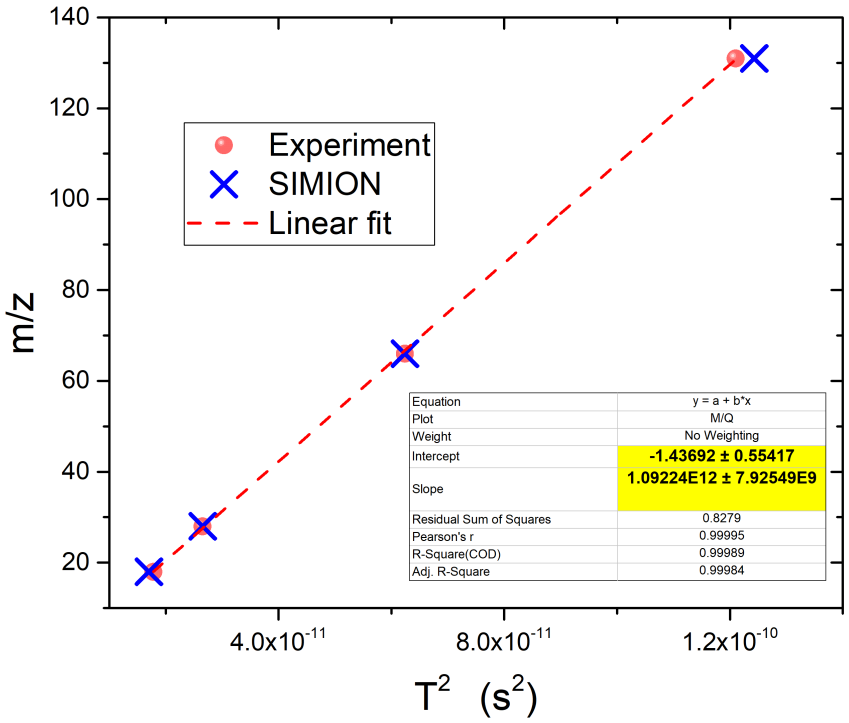

Figure 6.5: Experimental points together with SIMION simulations and the fit curve used for calibration of the spectrometer.

6.3 Second harmonic generation

Experiments undertaken as part of this thesis included the irradiation of molecules by the second harmonic of the fundamental laser pulse, generated via a second order nonlinear process. First demonstrated by Franken and his coworkers [189], the second harmonic generation process is based on the nonlinear response of matter upon the presence of intense laser fields. Opposite to conventional light sources, the relationship between polarization and the applied electric field deviates from linearity for the case of lasers. In that case, the induced polarization is expressed as a power series with respect to the laser field:

$$P = \epsilon_0 \left(\chi_1 \times E(t) + \chi_2 \times E(t)^2 + \chi_3 \times E(t)^3 + ...\right) \tag{6.2}$$

where χ_1 is the linear susceptibility and χ_2, χ_3 are the second and third order nonlinear coefficients respectively. Let us now neglect all the terms except for the second one. Assuming an incident electric field of frequency ω described by the expression :

$$E(t) = E_0 \times e^{(-i\omega t)} + E_0^* \times e^{(i\omega t)} \tag{6.3}$$

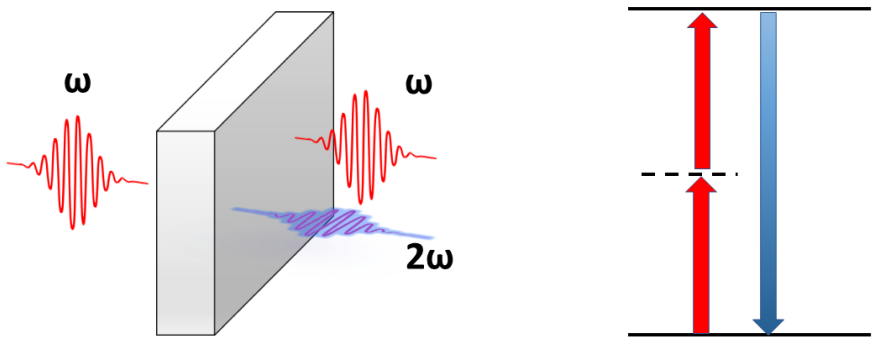

Figure 6.6: Second harmonic generation by means of a Type I Barium Borate (BBO) crystal.

substituting equation 6.3 to equation 6.2 one gets :

$$P = 2\epsilon_0\chi_2 E_0 E_0^* + 2\epsilon_0\chi_2 E_0^2 e^{(-2i\omega t)} + 2\epsilon_0\chi_2 (E_0^*)^2 e^{(2i\omega t)} \tag{6.4}$$

From equation 6.4, one sees that the first term corresponds to a DC field (known as optical rectification) whereas the other two terms correspond to a field oscillating with twice the fundamental frequency (2ω). Thus, the fundamental laser field, forces a number of dipoles to oscillate at 2ω. Alternatively, from a photon standpoint, the aforementioned process can be described as an absorption of two photons of the fundamental frequency (by means of a virtual state), followed by the emission of a second harmonic photon as seen in Figure 6.6.

In order to achieve efficient generation of the second harmonic radiation, these dipoles should oscillate in phase leading to a phased array of radiating antennas resulting in constructive interference. The required condition is that the sum of the fundamental and the second harmonic wavevectors is zero. This so called phase matching condition can be achieved by making use of birefringent crystals. Phase matching conditions can be established by tuning the angle formed between the direction of propagation and one of the principal axes of the medium. In our experiments a Type I Barium Borate (BBO) crystal was used, resulting in a second harmonic radiation polarized perpendicular to the fundamental frequency.

6.4 Results and discussion

Methane is considered a benchmark molecule since it is the simplest member of the hydrocarbon family. Thus it is not surprising that it has attracted a lot of interest from many scientific viewpoints. First, from an environmental scientist's viewpoint, methane is important being a significant contributor to the greenhouse effect. Furthermore, it is a very distinctive compound for astronomers: Titan is the largest moon of Saturn and the only known moon with a significant atmosphere. It is also the second most abundant compound in Titan's atmosphere. In that case, complex hydrocarbons are formed in Titan's upper atmosphere in reactions coming from the breakup of methane by the Sun's ultraviolet light. It follows that a deep understanding of the most fundamental processes such as the ionization/dissociation of methane is pursued as a basis to illustrate more complex phenomena associated with this molecule (e.g. structural change of the singly ionized methane compared to the neutral precursor [190]).

Previous studies on methane ionization in laser fields of nanosecond duration [191] showed an absence of the singly charged fundamental fragment CH_4^+ in the TOF spectrum. This was explained to be the result of the dissociation of CH_4^+ into the CH_3^+ and a hydrogen atom. On the other hand, when the pulse duration was reduced to 8 fs [192], all the fragment ions disappeared, except for the CH_4^+ and CH_3^+ molecular ions indicating that methane did not have enough time to dissociate after the ionization step.

6.5 Multistep dissociation of methane

Two alternative mechanisms concerning the dissociation of the CH_4 molecule have been proffered in the literature. On one hand the so called field assisted dissociation (FAD) model [193] and the quasi classical trajectory calculation, is based on the hypothesis that the potential energy curves along the C-H bond are preferentially distorted by the laser field in such a way as to favour the $CH_4^+ \longrightarrow CH_3 + H^+$ channel over the $CH_4^+ \longrightarrow CH_3^+ + H$ pathway. The same holds for the secondary dissociation channels. On the other hand, a recent experiment revealed an alternative dissociation channel [194]. More to the point, their findings suggested a stepwise dissociation process that does not lead to the generation of protons : $CH_4^+ \longrightarrow CH_3^+ + H$, $CH_3^+ \longrightarrow CH_2^+ + H$, $CH_2^+ \longrightarrow CH^+ + H$, $CH^+ \longrightarrow C^+ + H$. From a physics standpoint, the difference between the two aforementioned works is that the former dissociation occurs within the spatio-temporal influence of the laser pulse, whereas in the latter case the laser pulse is assumed to generate hot and unstable ions which subsequently dissociate. In order to figure out which of the two mechanisms is dominant under our experimental conditions, we examine the intensity dependence of the daughter ion signals as a function of the laser intensity for the two different wavelengths.

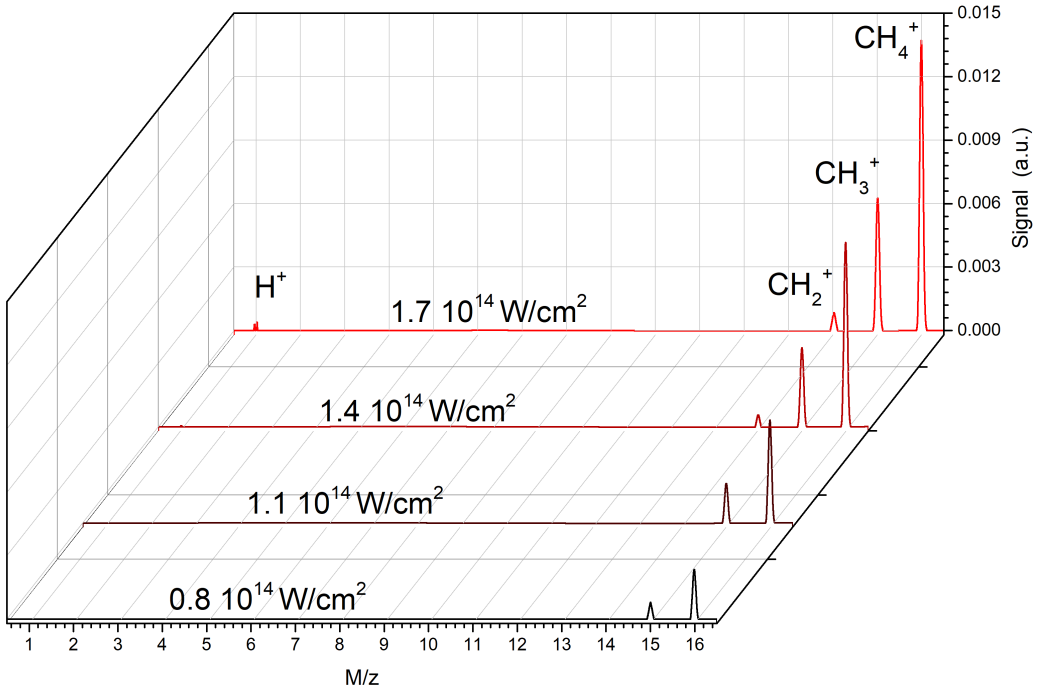

Figure 6.7: Ion TOF spectra as a function of the laser intensity for dissociation of methane irradiated by 800 nm laser pulses.

Our experimental findings for the fundamental wavelength support the presence of a step-wise dissociation process, which seems compatible to the latter mechanism. As can be seen in Figure 6.7, at low intensities we observe only the CH_4^+ and the CH_3^+ peaks. As the intensity increases the CH_2^+ peak appears without the presence of H^+ ions. This observation indicates the dominance of the $CH_n^+ \longrightarrow CH_{n-1}^+ + H$ mechanism over the $CH_n^+ \longrightarrow CH_{n-1} + H^+$ pathway. The H_2^+ peak appears at a laser intensity of $\approx 1.7\ 10^{14}\ W/cm^2$.

Figure 6.8 shows the ion TOF spectra for the second harmonic laser field (400 nm), for the same laser intensities as in the case of the fundamental wavelength. In that case the H^+ peak appears at the lowest laser intensity, together with the CH_4^+, CH_3^+ , CH_2^+ and the CH^+ peaks. This observation supports the presence of the $CH_n^+ \longrightarrow CH_{n-1} + H^+$ dissociation pathway opposite to the case of the fundamental wavelength. In addition, the CH^+ and the C^+ ions could potentially be produced via the $CH_3^+ \longrightarrow CH^+ + H_2$, $CH_2^+ \longrightarrow C^+ + H_2$ channels respectively. However, these pathways seems unfavorable for the fundamental laser field (800 nm) due to the absence of a significant H_2^+ signal. On the other hand these channels are possible in the case of the second harmonic laser field as we observe the H^+ peak at a laser intensity of $\approx 1.4\ 10^{14}\ W/cm^2$.

Figure 6.9a includes the yields for the 'heavier' molecular ions as a function of the

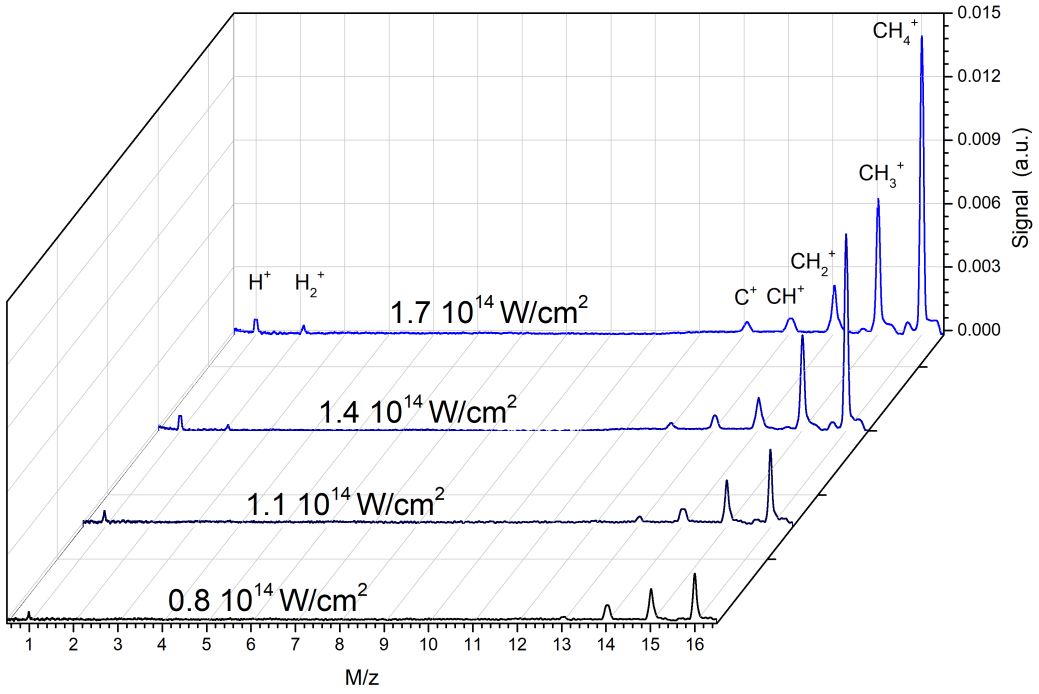

Figure 6.8: Ion TOF spectra as a function of the laser intensity for dissociation of methane irradiated by 400 nm laser pulses.

laser intensity at 800 nm. A similar plot is shown in Figure 6.9b corresponding to irradiation of methane with the second harmonic field at 400 nm. When dissociation of methane is induced by the fundamental wavelength, we observe that the formation of the CH_2^+ fragment is a bottleneck in the step-wise process. This can be reasonably attributed to the high threshold, estimated for the dissociation of the CH_3^+ ions. However this is not true for the second harmonic laser field. Now a weaker bottleneck seems to be the formation of the CH^+ ion, indicating that there should be a high threshold for the dissociation of the CH_2^+ ion in the step-wise sequence. Additionally, we notice that the CH^+ and the C^+ ions saturate under irradiation by the 400 nm laser field but not in the case of 800 nm laser field, at comparable intensities.

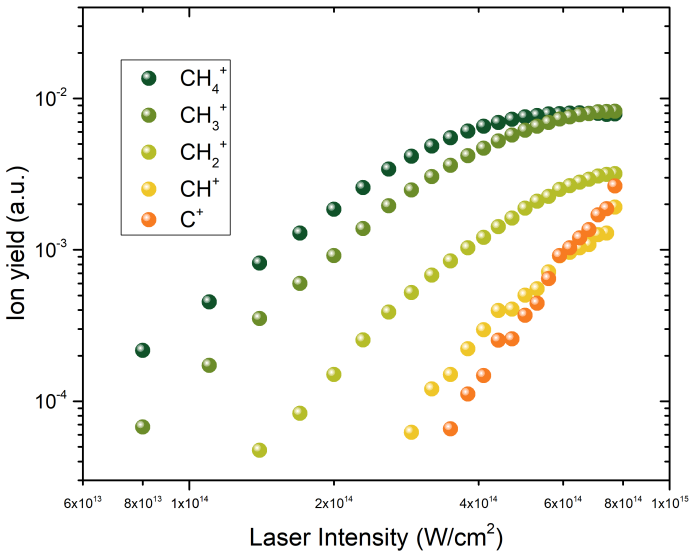

(a)

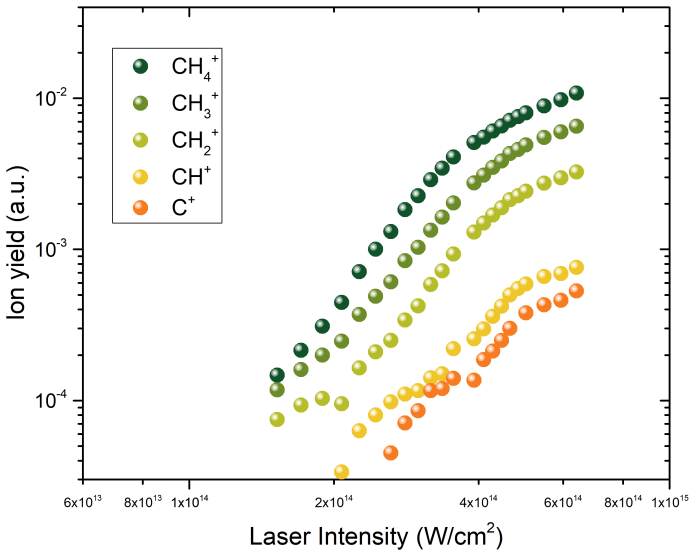

(b)

Figure 6.9: Ion yields as a function of the laser intensity for dissociation of methane irradiated by (a) 800 nm and (b) 400nm laser pulses.

6.6 Effect of laser intensity on the fragmentation mechanism

In Figures 6.10a and 6.10b we present the ion TOF spectra obtained at higher laser intensities for both the fundamental and the second harmonic laser fields. The fragmentation pattern becomes significantly different compared to what we observed at lower intensities. The most striking difference concerns the H^+ ions in the TOF spectra. Now, the H^+ signal associated to the 800 nm laser field is significantly higher compared to the case of the second harmonic field.

Importantly, Figure 6.11a shows that the H^+ fragments for the case of 800 nm laser field exhibit forward - backward peaks which are indicative of ions carrying high kinetic energy. This is a noteworthy difference compared to lower laser intensities, implying that the H^+ ions cannot be attributed to a stepwise dissociation process anymore. Instead, ions carrying significant kinetic energies should be considered as products of a Coulomb explosion process. In that case explosion of the doubly charged, unstable dications (CH_4^{2+}, CH_3^{2+}, CH_2^{2+}, CH^{2+}) should be expected to be the main source of H^+ ions. The same pattern is also observed in Figure 6.11b for the H^+ peaks in the spectrum acquired when methane is irradiated by the second harmonic field. The H^+ signal now exhibits a forward - backward structure, while the peak at the central part is still present. Such a peak, is indicative of fragments with negligible kinetic energy and it was previously associated with the $CH_n^+ \longrightarrow CH_{n-1} + H^+$ stepwise dissociation pathway which is still open at higher laser intensities.

A complete identification of the channels that give rise to the H^+ fragments is rather difficult. However, in Figures 6.12a and 6.12b we observe the presence of the CH_2^{2+} fragments in the TOF spectra. This is a clear indication that the $CH_2^{2+} \longrightarrow CH^+ + H^+$ channel contributes to the H^+ signal. The CH_3^{2+} and CH^{2+} dications are known to be very unstable species and as such they are not observed in our experimental data.

The CH_4^{2+} dication is also present in the TOF spectra for both laser wavelengths. This indicates that the $CH_4^{2+} \longrightarrow CH_2^+ + H_2^+$ channel should be open. Indeed this seems to be true for the 800 nm laser field, given that the H_2^+ peak exhibits a forward - backward structure which is compatible with the Coulbomb explosion process of the CH_4^{2+} dication. This pathway is not feasible for the 400 nm laser field, since the H_2^+ exhibits a broad structure implying that this fragment should come from a dissociation precess of a singly charged molecular ion. A possible channel that could result in H_2^+ fragments with negligible kinetic energy is $CH_4^+ \longrightarrow CH_2 + H_2^+$.

The methane dication may also follow an alternative Coulomb explosion process: $CH_4^{2+} \longrightarrow CH_3^+ + H^+$. This Coulomb explosion process would, as a matter of fact, lead to the production of H^+ ions carrying a significant amount of kinetic energy. Both the $CH_4^{2+} \longrightarrow CH_2^+ + H_2^+$ and the $CH_4^{2+} \longrightarrow CH_3^+ + H^+$ Coulomb explosions would require a significant amount of energy to doubly ionize the methane

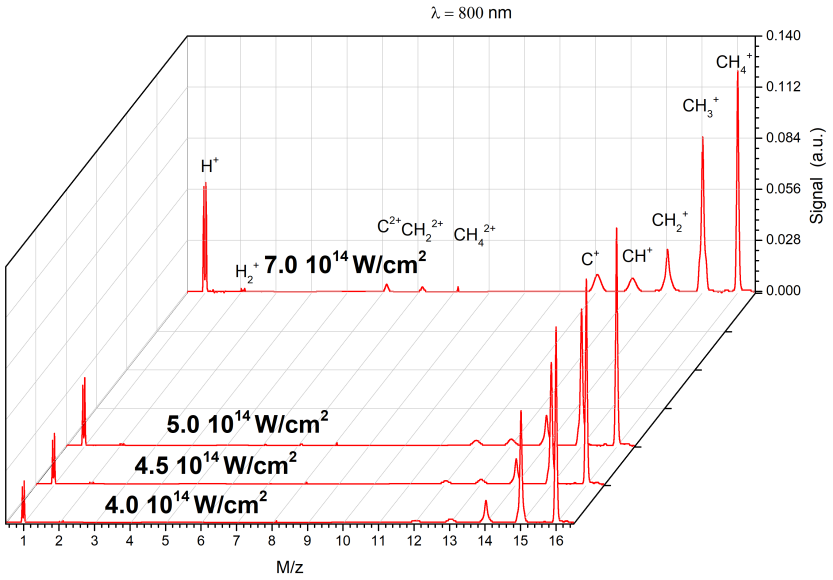

(a)

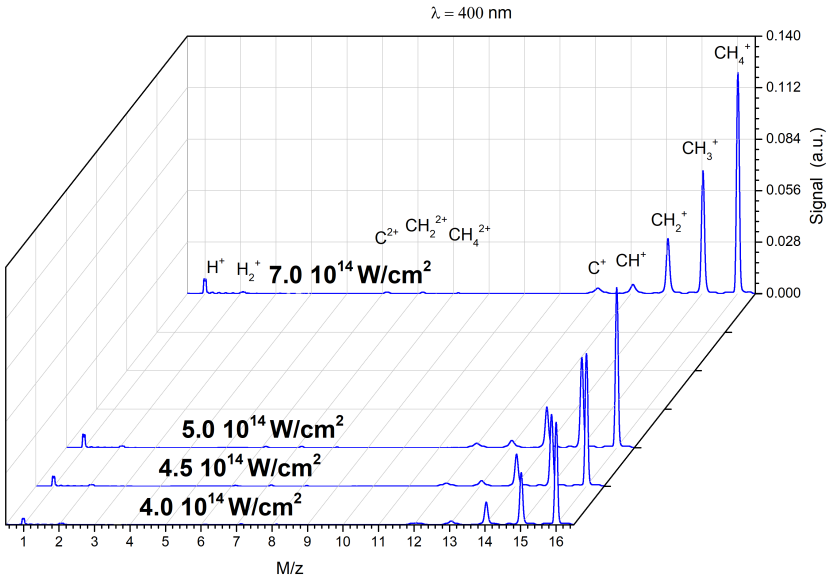

(b)

Figure 6.10: Ion TOF spectra for a set of higher laser intensities ranging from 4 10^{14} W/cm^2 to 7 10^{14} W/cm^2 . The upper panel (a) corresponds to the fragmentation of methane induced by the 800 nm laser field, whereas the bottom panel (b) refers to the fragmentation of the same molecule irradiated by the second harmonic field at a wavelength of 400 nm.

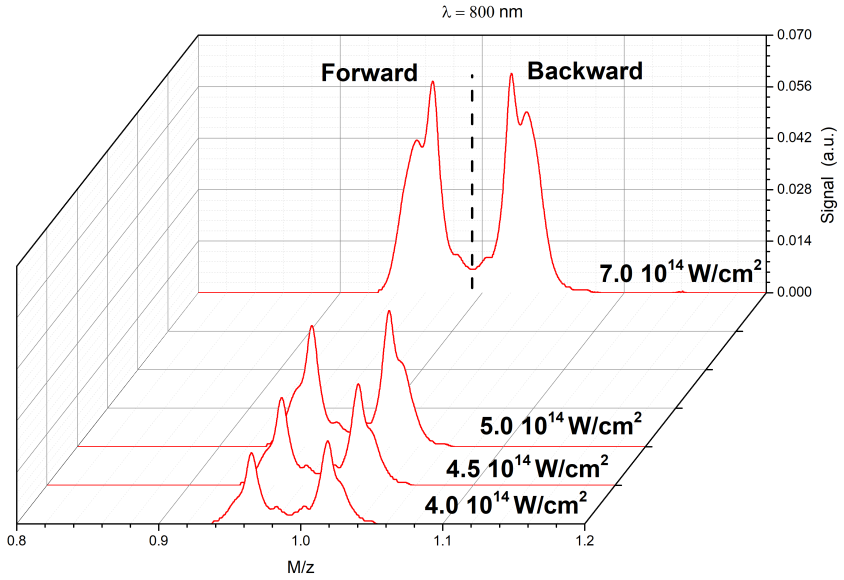

(a)

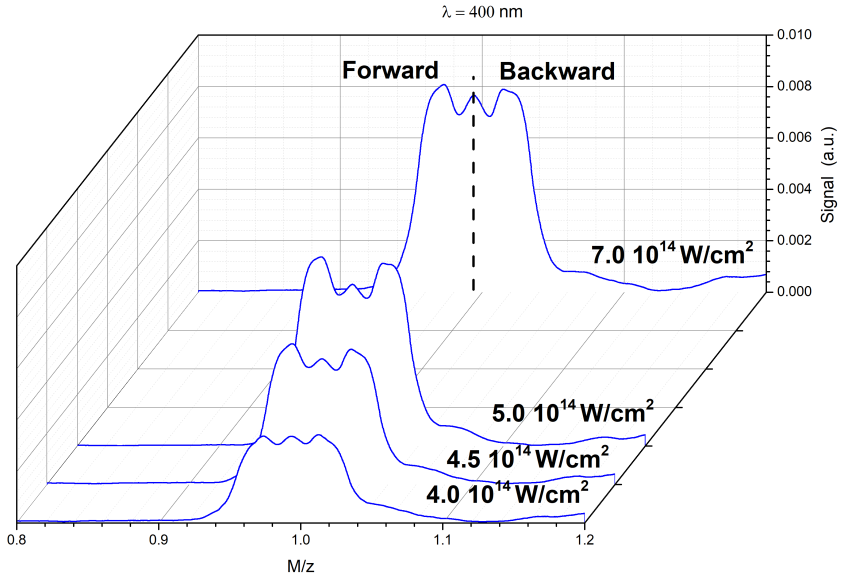

(b)

Figure 6.11: The same TOF spectra as in Figure 6.10 focused on the H^+ fragments. In that case we observe a forward - backward peak structure for both 800 nm and 400 nm laser fields. When the fundamental laser field at 800 nm is concerned, we observe three pairs of forward - backward peaks, as a result of the Coulomb explosion of unstable doubly charged ions (CH_4^{2+}, CH_3^{2+}, CH_2^{2+}, CH^{2+}). The same is true for the second harmonic field, where in addition to the central peak that was observed at lower intensities, one extra forward - backward component appears.

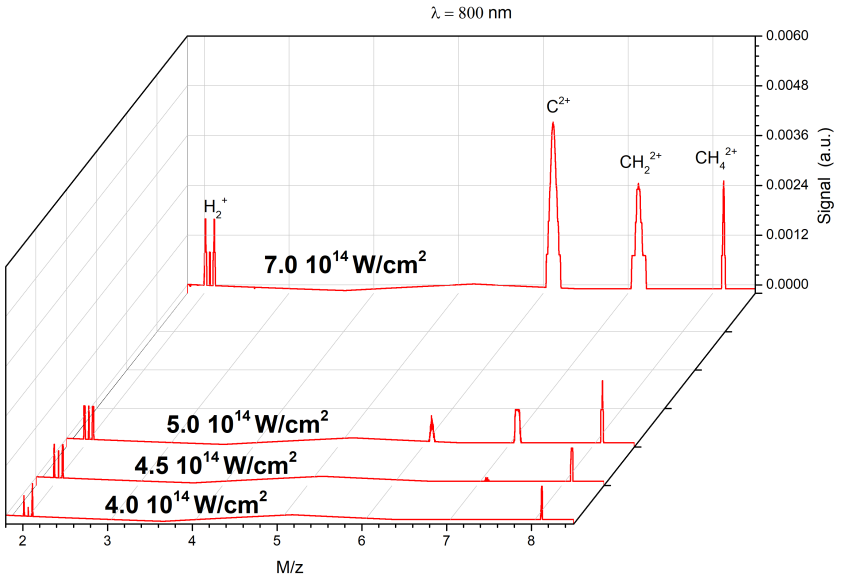

(a)

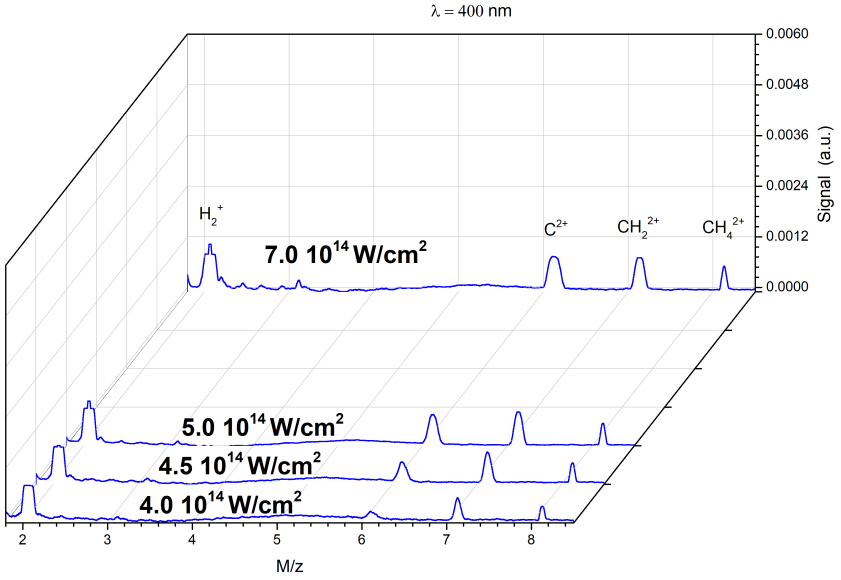

(b)

Figure 6.12: The same TOF spectra as in Figure 6.10 focused on the H_2^+, CH_4^{2+} and CH_2^{2+} fragments that were not present in the spectra for lower laser intensities. As can be seen, the H_2^+ signal exhibits a forward - backward peak structure in addition to the central peak. This structure is indicative of two different contributions to the H_2^+ fragments : the forward - backward components represent fragments with high kinetic energies coming from Coulomb explosion processes, whereas the central peak is indicative of H_2^+ fragments with a thermal energy distribution that can emerge from a stepwise process. In the case of the second harmonic laser field, only fragments with negligible kinetic energies are present in the TOF spectrum. This leads us to exclude any Coulomb explosion channels that would result in the H_2^+ fragments.

molecule. The double ionization of the precursor would however be possible via the rescattering double ionization process [195]. More specifically, in Figure 6.13 we see that the ponderomotive energy acquired by the electrons, is higher than the ionization energy needed for the double ionization of CH_4 molecule, approximately (35-40 eV [196, 197]) i.e., only for the high part of laser intensities in the case of 800 nm laser field. On the other hand, the second harmonic field is expected to significantly suppress the rescattering process. Hence, when the 800 nm laser field is concerned, we observe that the fastest H^+ peak in the spectrum appears as a shoulder at lower laser intensities (see Figure 6.11a) and becomes a separate peak at higher intensities where the ponderomotive energies are high enough to ensure rescattering double ionization of methane. As can be seen in Figure 6.11b such a peak is absent in the case of the 400 nm laser field even at the highest laser intensity since the ponderomotive energy is not enough to induce the rescattering process.

After close inspection at the H_2^+ signal for the 800 nm laser field, it is observed that in addition to the forward - backward peaks there is a central peak, indicative of fragments with a thermal velocity distribution. In Figure 6.12a we observe that the signal corresponding to the forward - backward components becomes noticeably stronger as the intensity exceeds the threshold above which the rescattering double ionization of methane is expected to be significant. On the other hand the central peak remains largely unaffected at increasing intensities confirming our assumption that this peak is not a product of the Coulomb explosion process of the methane dication.

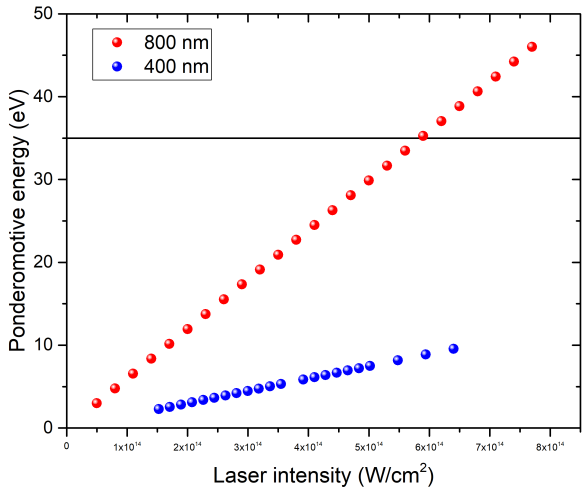

Figure 6.13: Ponderomotive energy acquired by the free electrons in the laser field for the range of laser intensities involved in our experiment. The horizontal black line corresponds to the minimum energy required for double ionization of neutral methane precursor.

6.7 Summary

To summarize, a comparative study on the fragmentation of methane induced by ultrafast laser fields of the fundamental Ti:Sapphire laser wavelength (800 nm) and its second harmonic field (400 nm) was performed. Our findings suggest significant differences in the fragmentation processes between the two laser wavelengths at lower laser intensities. More specifically, when the 800 nm laser field is used to irradiate the CH_4 molecule, the $CH_n^+ \longrightarrow CH_{n-1}^+ + H$ channel appears as the dominant dissociation pathway. On the other hand, in the case of the 400 nm field, the $CH_n^+ \longrightarrow CH_{n-1} + H^+$ mechanism prevails. At higher laser intensities, we observed forward - backward structure in the light H^+ and H_2^+ fragments in the 800 nm laser field TOF spectrum, which is representative of Coulomb explosion processes in the doubly charged dications. The same pattern is present in the case of the second harmonic radiation where a forward - backward component appears in the H^+ signal in addition to the central peak, observed at lower intensities. However the H_2^+ signal does not exhibit a forward - backward component, suggesting the absence of a Coulomb explosion process which results in H_2^+ fragments.

Chapter 7

Summary and future work

To summarize, the present work examined the interaction of atoms, molecules and photoionized plasmas with radiation emitted from different sources such as free electron lasers (FEL's), table top lasers and laser produced plasma (LPP) based sources.

Thus, Chapter 4 is concerned with two photon double ionization of Kr upon irradiation with FEL photons at 25.2 eV. Angle averaged photoelectron spectroscopy was applied to investigate the dependence of each spin-orbit component with respect to the FEL intensity. These measurements were complemented by angle resolved measurements that allowed for recording the angular distributions of the emitted photoelectrons. The anisotropy parameters (β_2, β_4) were then extracted for all the open channels. Currently, theoretical calculations are being carried out by Grum-Grzhimailo and his coworkers. Such calculations are highlighting the presence of the Rydberg autoionizing resonances in this near threshold ionization scenario. As a part of the future work, experiments where the interaction of FEL photons with small molecules will be performed.

Photoabsorption measurements in the vicinity of carbon and oxygen K-edges were performed for CO_2 and CH_4 molecule and the corresponding photoionized plasmas. These measurements are reported in Chapter 5 and the main findings include spectral signatures of molecular (CH_3^+, CO) and atomic species (C, C^+, O, O^+, O^{2+}), produced by photochemical events taking place in the photoionized plasmas. Such species were identified with the aid of calculations performed by means of Cowan code and data obtained from the Gas Phase Core Excitation database. In the future, such K-edge measurements will be expanded in order to include molecules such as OCS and CF_4 and the corresponding molecular plasmas.

A study on the ionization and dissociation of methane in ultrashort 400 nm and 800 nm laser fields is reported in Chapter 6. The findings highlighted the differences in the stepwise fragmentation patterns induced by the two wavelengths. In addition, the intensity dependence of the stepwise dissociation pathways was investigated for both wavelengths, underlining the differences between the low and the high laser intensity region. The next step aims at investigating the ionization and dissociation of methane, irradiated by the third harmonic laser field at 267 nm.

Appendix A

The VMI technique

A.1 Introduction

Originally introduced by Chandler and Houston [198], ion imaging emerged as an advance to the pioneering work of Solomon [199] for ions produced in a photo-dissociation process. In order to perform imaging, one has to use a spectrometer that follows the classic Wiley-McLaren design [187], with the major difference being the presence of a position-sensitive (PSD) detector at the end of the field-free region. The detector consists of a microchannel plate (MCP) pair, coupled to a charge coupled device (CCD) camera. When the charged particles (ions or electrons) hit the front surface of the MCP, they cause an avalanche of electrons at the back of the detector. Consequently, the electrons hit a phosphor screen that flashes. The emitted radiation is then captured by the CCD camera to produce an image.

A milestone for imaging technique, occurred when Eppink and Parker mapped particles having the same initial velocity on the same detector position [121]. In order to perform the so called "velocity mapping" they modified the electrodes of the imaging spectrometer. More specifically they substituted the grids used in the original geometry, with an electrostatic lens. In addition to the velocity mapping, they also managed to increase the resolution by removing the distortions induced by the grids. Furthermore, ions/electrons with the same initial ejection angle impact the same position on the detector, allowing for angle-dependent studies.

A schematic of a VMI spectrometer is presented in Figure A.1

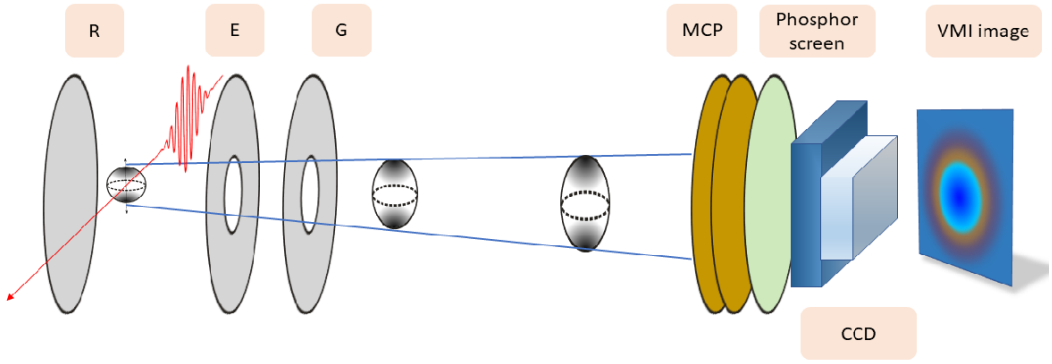

Figure A.1: The main parts of a VMI spectrometer: the electrodes include the repeller (R), the extractor (E) and a grounded electrode (G). Charged particles formed during the ionization/dissociation process are accelerated towards the position-sensitive detector. A CCD camera is used to image the light flashes generated when electrons from the MCP's hit the phosphor screen.

A.2 The Newton spheres

In the momentum space, the photoions/electrons expand on a sphere defined by the conservation of momentum. Thus, ions of the same initial velocity lie on the same surface of the sphere under VMI conditions. Furthermore, concentric spheres are formed with their radii being proportional to the velocities of the photo-ions/electrons. The spheres, so formed are called Newton spheres. The expanding Newton spheres are accelerated along the TOF axis and in the case of ionic fragments, mass-separated Newton spheres are formed. When a linearly polarized laser pulse is used, the symmetry of the velocity distribution is cylindrical around the laser polarization direction. Newton spheres are projected on the two-dimensional detector and ion-images are recorded. Because the momentum distribution is anisotropic along with the laser field, the image produced, exhibits two opposing crescent shapes.

A.3 The inversion process

After acquiring the 2-D VMI image the next step is the inversion process. It should be mentioned here that a direct inversion is possible only for systems with cylindrical symmetry. In that case, one has to apply a so called Abel transformation to retrieve a 2-D slice through the 3-D Newton sphere. The 3D velocity distribution can be obtained by applying a rotation around the cylindrical axis in the 2-D slice. Alternative approaches for recovery of the initial velocity distribution have been developed that include the onion peeling and the filtered back-projection methods. A summary of the four VMI steps is illustrated in Figure A.2.

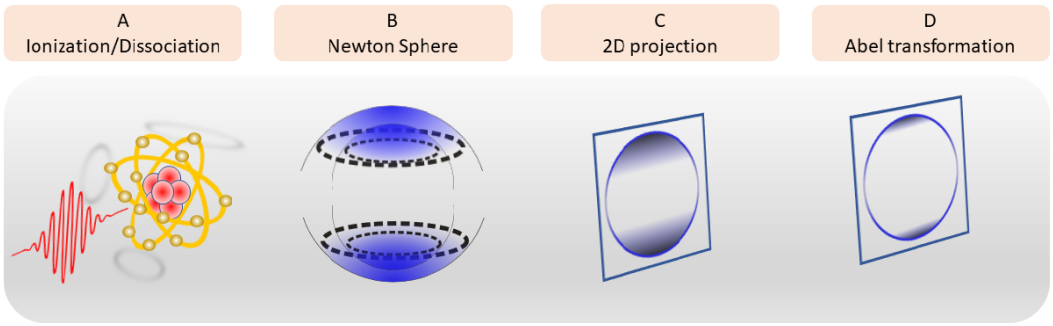

Figure A.2: The four main steps of the VMI technique: A) in first step atomic photoionization or molecular dissociation takes place B) the formation of concentric Newton spheres, for photo products (ions/electrons) of different velocity, C) 2-D projection of the initial 3-D velocity distribution and finally D) 2-D slice acquired after Abel inversion.

Alternatively, one can apply an experimental modification called slicing to avoid the mathematical recovery process in the final step. Now, one has to record only the central portion of the Newton sphere instead of collapsing the full 3-D sphere. The first demonstration of experimental slicing was achieved by Kitsopoulos and his co-workers [200]. Since then, several methods such as optical slicing and Doppler or DC slicing have been developed (for a detaileded review see [201]).

Appendix B

Optimization of the LPP SXR source

There are two parameters to be optimized for each valve, the first one is the delay time with respect to the instant of arrival of the trigger pulse and the second is the duration of the valve opening as can be seen in Figure B.1. In our case the duration of the valve opening was set at its maximum value as ($D = 1mss - T_{Delay}$). Hence the delay times were optimized for both the inner (T_{Delay1}) and the outer (T_{Delay2}) gases of the double stream gas puff target. Figure B.2 shows the results of this optimization process for the krypton/helium case that guided us to pick delay times of 750 μs and 700 μs for krypton and xenon respectively. Furthermore, the delay time for the auxiliary valve ejecting the molecular gas was also optimized. Figure B.2 indicates that a delay time of 500 μs should be chosen for the valve ejecting carbon dioxide. In a same manner a delay time of 800 μs was chosen for the case of methane. For more information regarding the timing and synchronization can be found in references [158, 79]. The backing pressures were chosen as 9 *bar* for the inner gases (krypton and krypton xenon mixture) and 6 *bar* for the helium acting as the outer gas. Regarding the target gases, the valve was pressurized at 4 *bar* for carbon dioxide and 1 *bar* for methane.

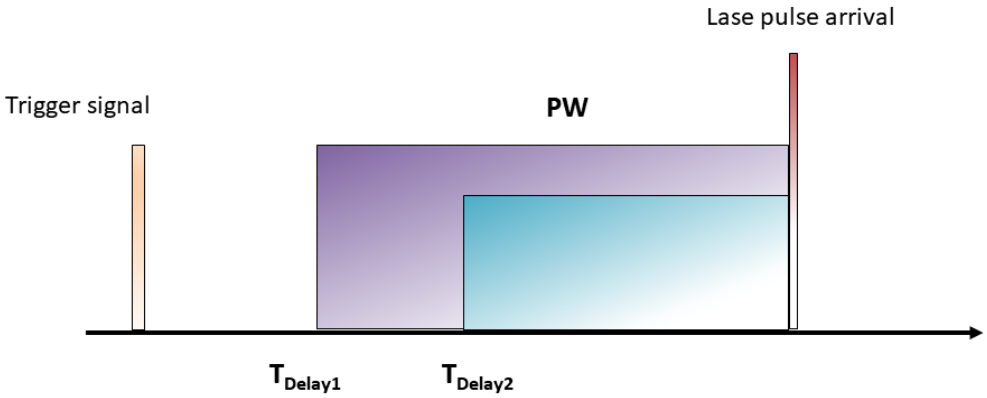

Figure B.1: Timing scheme of the double stream gas puff target.

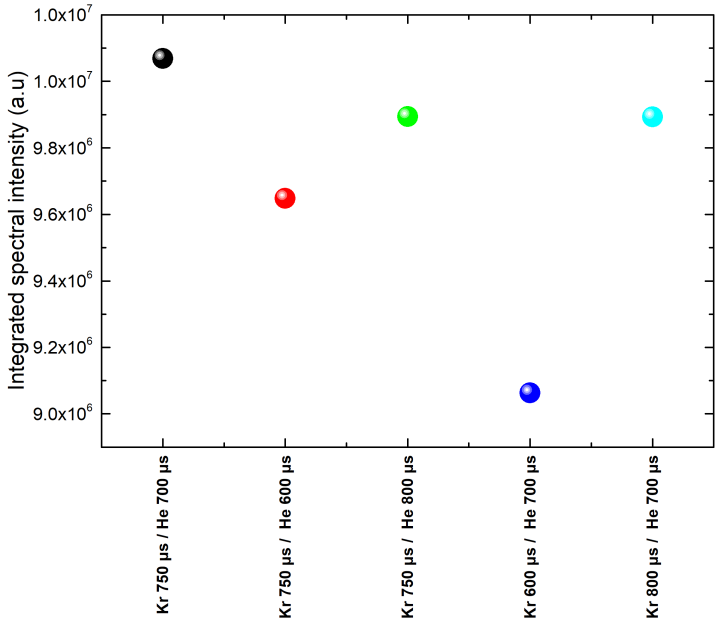

Figure B.2: Integrated spectral intensities, for different set of time delays in the case of krypton (inner gas) and helium (outer gas) gases.

Bibliography

[1] Laser safety micro-course. http://laserhelpers.kentek.com/wp-content/uploads/2014/04/Micro-Course.pdf.

[2] *Coherent micra user manual.* Coherent Inc., 5100 Patrick Henry Drive, Santa Clara, CA 95054 USA.

[3] *Coherent legend elite user manual.* Coherent Inc., 5100 Patrick Henry Drive, Santa Clara, CA 95054 USA.

[4] http://pr.desy.de.

[5] S. Varro. *Free Electron Lasers*. IntechOpen, 2012.

[6] A.P. Hitchcock and D.C. Mancini. *J. Electron. Spectrosc. Relat. Phenom.*, 67:7, 1994.

[7] R D. Cowan. *The Theory of Atomic Structure and Spectra*. Berkeley CA University of California Press, 1981.

[8] Atomic Structure Suite of Code, online at: http://aphysics2.lanl.gov/ftp/pub/cowan//, Los Alamos National Laboratory, USA (2005).

[9] H. Hertz. *Ann. Phys.*, 267:983–1000, 1887.

[10] A. Einstein. *Ann. Phys.*, 322:132–148, 1905.

[11] Arthur H. Compton. *Phys. Rev.*, 21:483–502, 1923.

[12] E. Schrödinger. *Phys. Rev.*, 28:1049–1070, 1926.

[13] W. Heisenberg. *Z. Phys.*, 43:172–198, 1927.

[14] Christian Wagner and Noreen Harned. *Nat. Photonics*, 4:24–26, 2010.

[15] Russell S. Harmon, Frank C. DeLucia, Catherine E. McManus, Nancy J. McMillan, Thomas F. Jenkins, Marianne E. Walsh, and Andrzej Miziolek. *Appl. Geochem.*, 21:730–747, 2006.

[16] L. Da Silva, J. Trebes, R. Balhorn, S. Mrowka, E. Anderson, D. Attwood, T. Barbee, J. Brase, M. Corzett, J. Gray, and Al. Et. *Science*, 258:269–271, 1992.

[17] Ivan Vartaniants. *AIP Conf. Proc.*, 1236:200–200, 2010.

[18] Raymond M. Measures. *Endeavour*, 13:108–116, 1989.

[19] A. Einstein. *Phys. Z.*, 18:121–128, 1917.

[20] T. H. Maiman. *Nature*, 187:493–494, 1960.

[21] A. Javan, W. R. Bennett, and D. R. Herriott. *Phys. Rev. Lett.*, 6:106–110, 1961.

[22] William T. Silfvast. *Laser Fundamentals*. 1997.

[23] U. Keller, G. W. 'tHooft, W. H. Knox, and J. E. Cunningham. *Opt. Lett.*, 16:1022–1024, 1991.

[24] Donna Strickland and Gerard Mourou. *Opt. Commun.*, 56:219–221, 1985.

[25] Sterling Backus, Charles G. Durfee, Margaret M. Murnane, and Henry C. Kapteyn. *Rev. Sci. Instrum.*, 69:1207–1223, 1998.

[26] Davide Castelvecchi and Elizabeth Gibney. *Nature*, 562:20–20, 2018.

[27] A. L. Schawlow and C. H. Townes. *Phys. Rev.*, 112:1940–1949, 1958.

[28] N. G. Basov and A. M. Prokhorov. *J. Exp. Theor. Phys.*, 1:184–185, 1955.

[29] Xiaolei Zhu, Xiuhua Ma, Shiguang Li, and Weibiao Chen. In *XX International Symposium on High-Power Laser Systems and Applications 2014*, volume 9255, pages 43 – 48. International Society for Optics and Photonics, SPIE, 2015.

[30] BEA Saleh and MC Teich. *Electro-Optics*, chapter 18, pages 696–736. John Wiley & Sons, Ltd, 2001.

[31] C Rullière. *Femtosecond Laser Pulses: Principles and Experiments (Second Edition)*. 2003.

[32] P. F. Moulton. *J. Opt. Soc. Am. B*, 3:125–133, 1986.

[33] *Coherent verdi user manual.* Coherent Inc., 5100 Patrick Henry Drive, Santa Clara, CA 95054 USA.

[34] R. Dabu. *Crystals*, 9:347, 2019.

[35] D. E. Spence, P. N. Kean, and W. Sibbett. *Opt. Lett.*, 16:42–44, 1991.

[36] Edmond B. Treacy. *IEEE J. Quantum Electron.*, 5:454–458, 1969.

[37] W. C. Röntgen. *Science*, 3:227–231, 1896.

[38] F. R. Elder, A. M. Gurewitsch, R. V. Langmuir, and H. C. Pollock. *Phys. Rev.*, 71:829–830, 1947.

[39] David Attwood. *Soft X-rays and Extreme Ultraviolet Radiation*. 1999.

[40] H. Motz. *J. Appl. Phys.*, 22:527–535, 1951.

[41] Gennadii N. Kulipanov. *Phys.—Usp.*, 177:384, 2007.

[42] R.M. Phillips. *IRE Trans. Electron Dev.*, 7:231–241, 1960.

[43] John M J Madey. *J. Appl. Phys.*, 42:1906–1913, 1971.

[44] D. A G Deacon, L. R. Elias, J. M J Madey, G. J. Ramian, H. A. Schwettman, and T. I. Smith. *Phys. Rev. Lett.*, 38:892–894, 1977.

[45] Luis R. Elias, William M. Fairbank, John M J Madey, H. Alan Schwettman, and Todd I. Smith. *Phys. Rev. Lett.*, 36:717–720, 1976.

[46] Joachim Ullrich, Artem Rudenko, and Robert Moshammer. *Annu. Rev. Phys. Chem.*, 63:635–660, 2012.

[47] E.A. Seddon, J.A. Clarke, D.J. Dunning, C. Masciovecchio, C.J. Milne, F. Parmigiani, D. Rugg, J.C.H. Spence, N.R. Thompson, K. Ueda, S.M. Vinko, J.S. Wark, and W. Wurth. *Rep. Prog. Phys.*, 80:115901, 2017.

[48] John N Galayda, John Arthur, Daniel F Ratner, and William E White. *J. Opt. Soc. Am. B*, 27:B106, 2010.

[49] Brian W. J. McNeil and Neil R. Thompson. *Nat. Photonics*, 4:814–821, 2010.

[50] Ya.S. Derbenev, A M Kondratenko, and E L Saldin. *Nucl. Instrum. Methods Phys. Res.*, 193:415–421, 1982.

[51] J. Andruszkow, B. Aune, V. Ayvazyan, N. Baboi, R. Bakker, V. Balakin, D. Barni, A. Bazhan, M. Bernard, A. Bosotti, J. C. Bourdon, W. Brefeld, R. Brinkmann, S. Buhler, J. P. Carneiro, M. Castellano, P. Castro, L. Catani, S. Chel, Y. Cho, S. Choroba, E. R. Colby, W. Decking, P. Den Hartog, M. Desmons, M. Dohlus, D. Edwards, H. T. Edwards, B. Faatz, J. Feldhaus, M. Ferrario, M. J. Fitch, K. Flöttmann, M. Fouaidy, A. Gamp, T. Garvey, C. Gerth, M. Geitz, E. Gluskin, V. Gretchko, U. Hahn, W. H. Hartung, D. Hubert, M. Hüning, R. Ischebek, M. Jablonka, J. M. Joly, M. Juillard, T. Junquera, P. Jurkiewicz, A. Kabel, J. Kahl, H. Kaiser, T. Kamps, V. V. Katelev, J. L. Kirchgessner, M. Körfer, L. Kravchuk, G. Kreps, J. Krzywinski, T. Lokajczyk, R. Lange, B. Leblond, M. Leenen, J. Lesrel, M. Liepe, A. Liero, T. Limberg, R. Lorenz, L. H. Hua, L. F. Hai, C. Magne, M. Maslov, G. Materlik, A. Matheisen, J. Menzel, P. Michelato, W. D. Möller, A. Mosnier, U. C. Müller, O. Napoly, A. Novokhatski, M. Omeich, H. S. Padamsee, C. Pagani, F. Peters, B. Petersen, P. Pierini, J. Pflüger, P. Piot, B. Phung Ngoc, L. Plucinski, D. Proch, K. Rehlich, S. Reiche, D. Reschke, I. Reyzl, J. Rosenzweig, J. Rossbach, S. Roth, E. L. Saldin, W. Sandner, Z. Sanok, H. Schlarb, G. Schmidt, P. Schmüser, J. R. Schneider, E. A. Schneidmiller, H. J. Schreiber, S. Schreiber, P. Schütt, J. Sekutowicz, L. Serafini, D. Sertore, S. Setzer, S. Simrock, B. Sonntag, B. Sparr, F. Stephan, V. A. Sytchev, S. Tazzari, F. Tazzioli, M. Tigner, M. Timm, M. Tonutti, E. Trakhtenberg, R. Treusch, D. Trines, V. Verzilov, T. Vielitz, V. Vogel, G. V. Walter, R. Wanzenberg, T. Weiland, H. Weise, J. Weisend, M. Wendt, M. Werner, M. M. White, I. Will, S. Wolff, M. V. Yurkov, K. Zapfe, P. Zhogolev, and F. Zhou. *Phys. Rev. Lett.*, 85:3825–3829, 2000.

[52] V Ayvazyan, N Baboi, I Bohnet, R Brinkmann, M Castellano, P Castro, L Catani, S Choroba, a Cianchi, M Dohlus, H T Edwards, B Faatz, a a Fateev, J Feldhaus, K Flöttmann, a Gamp, T Garvey, H Genz, Ch Gerth, V Gretchko, B Grigoryan, U Hahn, C Hessler, K Honkavaara, M Hüning, R Ischebeck, M Jablonka, T Kamps, M Körfer, M Krassilnikov, J Krzywinski, M Liepe, a Liero, T Limberg, H Loos, M Luong, C Magne, J Menzel, P Michelato, M Minty, U-C Müller, D Nölle, a Novokhatski, C Pagani, F Peters, J Pflüger, P Piot, L Plucinski, K Rehlich, I Reyzl, a Richter, J Rossbach, E L Saldin, W Sandner, H Schlarb, G Schmidt, P Schmüser, J R Schneider, E a Schneidmiller, H-J Schreiber, S Schreiber, D Sertore, S Setzer, S Simrock, R Sobierajski, B Sonntag, B Steeg, F Stephan, K P Sytchev, K Tiedtke, M Tonutti, R Treusch, D Trines, D Türke, V Verzilov, R Wanzenberg, T Weiland, H Weise, M Wendt, I Will, S Wolff, K Wittenburg, M V Yurkov, and K Zapfe. *Phys. Rev. Lett.*, 88:104802, 2002.

[53] V. Ayvazyan, N. Baboi, I. Bohnet, R. Brinkmann, M. Castellano, P. Castro, L. Catani, S. Choroba, A. Cianchi, M. Dohlus, H. T. Edwards, B. Faatz, A. A. Fateev, J. Feldhaus, K. Fl??ttmann, A. Gamp, T. Garvey, H. Genz, Ch Gerth, V. Gretchko, B. Grigoryan, U. Hahn, C. Hessler, K. Honkavaara, M. H??ning, R. Ischebeck, M. Jablonka, T. Kamps, M. K??rfer, M. Krassilnikov, J. Krzywinski, M. Liepe, A. Liero, T. Limberg, H. Loos, M. Luong, C. Magne, J. Menzel, P. Michelato, M. Minty, U. C. M??ller, D. N??lle, A. Novokhatski, C. Pagani, F. Peters, J. Pfl??ger, P. Piot, L. Plucinski, K. Rehlich, I. Reyzl, A. Richter, J. Rossbach, E. L. Saldin, W. Sandner, H. Schlarb, G. Schmidt, P. Schm??ser, J. R. Schneider, E. A. Schneidmiller, H. J. Schreiber, S. Schreiber, D. Sertore, S. Setzer, S. Simrock, R. Sobierajski, B. Sonntag, B. Steeg, F. Stephan, K. P. Sytchev, K. Tiedtke, M. Tonutti, R. Treusch, D. Trines, D. T??rke, V. Verzilov, R. Wanzenberg, T. Weiland, H. Weise, M. Wendt, T. Wilhein, I. Will, K. Wittenburg, S. Wolff, M. V. Yurkov, and K. Zapfe. *Eur. Phys. J. D*, 20:149–156, 2002.

[54] V. Ayvazyan, N. Baboi, J. B??hr, V. Balandin, B. Beutner, A. Brandt, I. Bohnet, A. Bolzmann, R. Brinkmann, O. I. Brovko, J. P. Carneiro, S. Casalbuoni, M. Castellano, P. Castro, L. Catani, E. Chiadroni, S. Choroba, A. Cianchi, H. Delsim-Hashemi, G. di Pirro, M. Dohlus, S. D??sterer, H. T. Edwards, B. Faatz, A. A. Fateev, J. Feldhaus, K. Fl??ttmann, J. Frisch, L. Fr??hlich, T. Garvey, U. Gensch, N. Golubeva, H. J. Grabosch, B. Grigoryan, O. Grimm, U. Hahn, J. H. Han, M. V. Hartrott, K. Honkavaara, M. H??ning, R. Ischebeck, E. Jaeschke, M. Jablonka, R. Kammering, V. Katalev, B. Keitel, S. Khodyachykh, Y. Kim, V. Kocharyan, M. K??rfer, M. Kollewe, D. Kostin, D. Kr??mer, M. Krassilnikov, G. Kube, L. Lilje, T. Limberg, D. Lipka, F. L??hl, M. Luong, C. Magne, J. Menzel, P. Michelato, V. Miltchev, M. Minty, W. D. M??ller, L. Monaco, W. M??ller, M. Nagl, O. Napoly, P. Nicolosi, D. N??lle, T. Nu??ez, A. Oppelt, C. Pagani, R. Paparella, B. Petersen, B. Petrosyan, J. Pfl??ger, P. Piot, E. Pl??njes,

L. Poletto, D. Proch, D. Pugachov, K. Rehlich, D. Richter, S. Riemann, M. Ross, J. Rossbach, M. Sachwitz, E. L. Saldin, W. Sandner, H. Schlarb, B. Schmidt, M. Schmitz, P. Schm??ser, J. R. Schneider, E. A. Schneidmiller, H. J. Schreiber, S. Schreiber, A. V. Shabunov, D. Sertore, S. Setzer, S. Simrock, E. Sombrowski, L. Staykov, B. Steffen, F. Stephan, F. Stulle, K. P. Sytchev, H. Thom, K. Tiedtke, M. Tischer, R. Treusch, D. Trines, I. Tsakov, A. Vardanyan, R. Wanzenberg, T. Weiland, H. Weise, M. Wendt, I. Will, A. Winter, K. Wittenburg, M. V. Yurkov, I. Zagorodnov, P. Zambolin, and K. Zapfe. *Eur. Phys. J. D*, pages 297–303, 2006.

[55] W. Ackermann, G. Asova, V. Ayvazyan, A. Azima, N. Baboi, J. Bähr, V. Balandin, B. Beutner, A. Brandt, A. Bolzmann, R. Brinkmann, O. I. Brovko, M. Castellano, P. Castro, L. Catani, E. Chiadroni, S. Choroba, A. Cianchi, J. T. Costello, D. Cubaynes, J. Dardis, W. Decking, H. Delsim-Hashemi, A. Delserieys, G. Di Pirro, M. Dohlus, S. Düsterer, A. Eckhardt, H. T. Edwards, B. Faatz, J. Feldhaus, K. Flöttmann, J. Frisch, L. Fröhlich, T. Garvey, U. Gensch, Ch. Gerth, M. Görler, N. Golubeva, H.-J. Grabosch, M. Grecki, O. Grimm, K. Hacker, U. Hahn, J. H. Han, K. Honkavaara, T. Hott, M. Hüning, Y. Ivanisenko, E. Jaeschke, W. Jalmuzna, T. Jezynski, R. Kammering, V. Katalev, K. Kavanagh, E. T. Kennedy, S. Khodyachykh, K. Klose, V. Kocharyan, M. Körfer, M. Kollewe, W. Koprek, S. Korepanov, D. Kostin, M. Krassilnikov, G. Kube, M. Kuhlmann, C. L. S. Lewis, L. Lilje, T. Limberg, D. Lipka, F. Löhl, H. Luna, M. Luong, M. Martins, M. Meyer, P. Michelato, V. Miltchev, W. D. Möller, L. Monaco, W. F. O. Müller, O. Napieralski, O. Napoly, P. Nicolosi, D. Nölle, T. Nuñez, A. Oppelt, C. Pagani, R. Paparella, N. Pchalek, J. Pedregosa-Gutierrez, B. Petersen, B. Petrosyan, G. Petrosyan, L. Petrosyan, J. Pflüger, E. Plönjes, L. Poletto, K. Pozniak, E. Prat, D. Proch, P. Pucyk, P. Radcliffe, H. Redlin, K. Rehlich, M. Richter, M. Roehrs, J. Roensch, R. Romaniuk, M. Ross, J. Rossbach, V. Rybnikov, M. Sachwitz, E. L. Saldin, W. Sandner, H. Schlarb, B. Schmidt, M. Schmitz, P. Schmüser, J. R. Schneider, E. A. Schneidmiller, S. Schnepp, S. Schreiber, M. Seidel, D. Sertore, A. V. Shabunov, C. Simon, S. Simrock, E. Sombrowski, A. A. Sorokin, P. Spanknebel, R. Spesyvtsev, L. Staykov, B. Steffen, F. Stephan, F. Stulle, H. Thom, K. Tiedtke, M. Tischer, S. Toleikis, R. Treusch, D. Trines, I. Tsakov, E. Vogel, T. Weiland, H. Weise, M. Wellhöfer, M. Wendt, I. Will, A. Winter, K. Wittenburg, W. Wurth, P. Yeates, M. V. Yurkov, I. Zagorodnov, and K. Zapfe. *Nat. Photonics*, 1:336–342, 2007.

[56] M. Cornacchia and H. Winick. *Synchrotron Radiat. News*, 5:6–9, 1992.

[57] C. Pellegrini, J. Rosenzweig, H.-D. Nuhn, P. Pianetta, R. Tatchyn, H. Winick, K. Bane, P. Morton, T. Raubenheimer, J. Seeman, K. Halbach, K.-J. Kim, and J. Kirz. *Nucl. Instrum. Methods Phys. Res. A*, 331:223–227, 1993.

[58] B. Aune, R. Bandelmann, D. Bloess, B. Bonin, A. Bosotti, M. Champion,

C. Crawford, G. Deppe, B. Dwersteg, D. A. Edwards, H. T. Edwards, M. Ferrario, M. Fouaidy, P.-D. Gall, A. Gamp, A. Gössel, J. Graber, D. Hubert, M. Hüning, M. Juillard, T. Junquera, H. Kaiser, G. Kreps, M. Kuchnir, R. Lange, M. Leenen, M. Liepe, L. Lilje, A. Matheisen, W.-D. Möller, A. Mosnier, H. Padamsee, C. Pagani, M. Pekeler, H.-B. Peters, O. Peters, D. Proch, K. Rehlich, D. Reschke, H. Safa, T. Schilcher, P. Schmüser, J. Sekutowicz, S. Simrock, W. Singer, M. Tigner, D. Trines, K. Twarowski, G. Weichert, J. Weisend, J. Wojtkiewicz, S. Wolff, and K. Zapfe. *Phys. Rev. Accel. Beams*, 3:092001, 2000.

[59] C. Pellegrini. *Phys. Scr.*, T169:014004, 2016.

[60] K. Tiedtke, A. Azima, N. Von Bargen, L. Bittner, S. Bonfigt, S. Düsterer, B. Faatz, U. Frühling, M. Gensch, Ch Gerth, N. Guerassimova, U. Hahn, T. Hans, M. Hesse, K. Honkavaar, U. Jastrow, P. Juranic, S. Kapitzki, B. Keitel, T. Kracht, M. Kuhlmann, W. B. Li, M. Martins, T. Núñez, E. Plönjes, H. Redlin, E. L. Saldin, E. A. Schneidmiller, J. R. Schneider, S. Schreiber, N. Stojanovic, F. Tavella, S. Toleikis, R. Treusch, H. Weigelt, M. Wellhöfer, H. Wabnitz, M. V. Yurkov, and J. Feldhaus. *New J. Phys.*, 11:023029, 2009.

[61] *FELs of Europe: Whitebook on Science with Free Electron Lasers, Paul Scherrer Institut,Villigen (2016)*.

[62] S. Suckewer, C. H. Skinner, H. Milchberg, C. Keane, and D. Voorhees. *Phys. Rev. Lett.*, 55:1753–1756, 1985.

[63] D. L. Matthews, P. L. Hagelstein, M. D. Rosen, M. J. Eckart, N. M. Ceglio, A. U. Hazi, H. Medecki, B. J. MacGowan, J. E. Trebes, B. L. Whitten, E. M. Campbell, C. W. Hatcher, A. M. Hawryluk, R. L. Kauffman, L. D. Pleasance, G. Rambach, J. H. Scofield, G. Stone, and T. A. Weaver. *Phys. Rev. Lett.*, 54:110–113, 1985.

[64] G. Jamelot, A. Carillon, A. Klisnick, and P. Jaeglé. *Appl. Phys. B*, 50:239–246, 1990.

[65] Pierre Jaeglé, Gérard Jamelot, Antoine Carillon, Annie Klisnick, Alain Sureau, and Hélène Guennou. *J. Opt. Soc. Am. B*, 4:563, 1987.

[66] B. J. MacGowan, S. Maxon, P. L. Hagelstein, C. J. Keane, R. A. London, D. L. Matthews, M. D. Rosen, J. H. Scofield, and D. A. Whelan. *Phys. Rev. Lett.*, 59:2157–2160, 1987.

[67] Shinsuke Fujioka, Hideaki Takabe, Norimasa Yamamoto, David Salzmann, Feilu Wang, Hiroaki Nishimura, Yutong Li, Quanli Dong, Shoujun Wang, Yi Zhang, Yong Joo Rhee, Yong Woo Lee, Jae Min Han, Minoru Tanabe, Takashi Fujiwara, Yuto Nakabayashi, Gang Zhao, Jie Zhang, and Kunioki Mima. *Nature Phys.*, 5:821–825, 2009.

[68] H. G. Wei, J. R. Shi, G. Zhao, Yi Zhang, Quan-Li Dong, Yu-Tong Li, Shou-Jun Wang, Jie Zhang, Zuotang Liang, Ji-Yan Zhang, Tian-Shu Wen, Wen-Hai

Zhang, Xin Hu, Shen-Ye Liu, Yong-Kun Ding, Lin Zhang, Yong-Jian Tang, Bao-Han Zhang, Zhi-Jian Zheng, Hiroaki Nishimura, Shinsuke Fujioka, Fei-Lu Wang, and Hideaki Takabe. *Astrophys. J.*, 683:577–583, 2008.

[69] Paddy Hayden, Anthony Cummings, Nicola Murphy, Gerry O'Sullivan, Paul Sheridan, John White, and Padraig Dunne. *J. Appl. Phys.*, 99, 2006.

[70] Takeshi Higashiguchi, Takamitsu Otsuka, Noboru Yugami, Weihua Jiang, Akira Endo, Bowen Li, Deirdre Kilbane, Padraig Dunne, and Gerry O'Sullivan. *Appl. Phys. Lett.*, 99:97–100, 2011.

[71] H. Fiedorowicz, A. Bartnik, Z. Patron, and P. Parys. *Laser and Particle Beams*, 12:471–483, 1994.

[72] H. Fiedorowicz, A. Bartnik, Z. Patron, and P. Parys. *Appl. Phys. Lett.*, 62:2778–2780, 1993.

[73] Henryk Fiedorowicz, Andrzej Bartnik, Mirosław Szczurek, Hiroyuki Daido, Noriyuki Sakaya, Viliam Kmetik, Yoshiaki Kato, Masayuki Suzuki, Masai Matsumura, Junichi Tajima, Takeyoshi Nakayama, and Thomas Wilhein. *Opt. Commun.*, 163:103–114, 1999.

[74] H Fiedorowicz and A Bartnik. *Bull. Pol. Ac.: Tech.*, 53:103–111, 2005.

[75] H. Fiedorowicz, A. Bartnik, R. Jarocki, R. Rakowski, and M. Szczurek. *Appl. Phys. B: Lasers and Optics*, 70:305–308, 2000.

[76] R. Rakowski, A. Bartnik, H. Fiedorowicz, F. De Gaufridy De Dortan, R. Jarocki, J. Kostecki, J. Mikołajczyk, L. Ryć, M. Szczurek, and P. Wachulak. *Appl. Phys. B: Lasers and Optics*, 101:773–789, 2010.

[77] A. Bartnik, P. Wachulak, H. Fiedorowicz, and W. Skrzeczanowski. *Phys. Plasmas*, 23:043512, 2016.

[78] P.W. Wachulak, A. Bartnik, J. Kostecki, L. Wegrzynski, T. Fok, R. Jarocki, M. Szczurek, and H. Fiedorowicz. *Nucl. Instrum. Methods. Phys. Res. B*, 364:40–48, 2015.

[79] Przemysław Wachulak, Martin Duda, Tomasz Fok, Andrzej Bartnik, Zhanshan Wang, Qiushi Huang, Antoni Sarzyński, Alexandr Jancarek, and Henryk Fiedorowicz. *Materials*, 11:1303, 2018.

[80] Daniel Adjei, Mesfin Getachew Ayele, Przemyslaw Wachulak, Andrzej Bartnik, Łukasz Wegrzynski, Henryk Fiedorowicz, Luděk Vyšín, Anna Wiechec, Janusz Lekki, Wojciech M. Kwiatek, Ladislav Pina, Marie Davídková, and Libor Juha. *Nucl. Instrum. Methods. Phys. Res. B*, 364:27–32, 2015.

[81] V. Schmidt. *Rep. Prog. Phys.*, 55:1483–1659, 1992.

[82] Geoffrey V. Marr and Ingolf Lindau. *Handbook on Synchrotron Radiation, Volume 2*. Physics Today, 1989.

[83] Maria Göppert-Mayer. *Ann. Phys.*, 401:273–294, 1931.

[84] H. Wabnitz, A. R.B. De Castro, P. Gürtler, T. Laarmann, W. Laasch, J. Schulz, and T. Möller. *Phys. Rev. Lett.*, 94:1–4, 2005.

[85] A. A. Sorokin, M. Wellhöfer, S. V. Bobashev, K. Tiedtke, and M. Richter. *Phys. Rev. A*, 75:1–4, 2007.

[86] R. Moshammer, Y. H. Jiang, L. Foucar, A. Rudenko, Th Ergler, C. D. Schröter, S. Lüdemann, K. Zrost, D. Fischer, J. Titze, T. Jahnke, M. Schöffler, T. Weber, R. Dörner, T. J.M. Zouros, A. Dorn, T. Ferger, K. U. Kühnel, S. Düsterer, R. Treusch, P. Radcliffe, E. Plönjes, and J. Ullrich. *Phys. Rev. Lett.*, 98:1–4, 2007.

[87] J Ullrich, R Moshammer, A N Perumal, and R Moshammer. *Rep. Prog. Phys*, 66:1463, 2003.

[88] A. A. Sorokin, S. V. Bobashev, T. Feigl, K. Tiedtke, H. Wabnitz, and M. Richter. *Phys. Rev. Lett.*, 99:1–4, 2007.

[89] M. Richter, M. Ya Amusia, S. V. Bobashev, T. Feigl, P. N. Juranić, M. Martins, A. A. Sorokin, and K. Tiedtke. *Phys. Rev. Lett.*, 102:1–4, 2009.

[90] A. A. Sorokin, S. V. Bobashev, K. Tiedtke, and M. Richter. *J. Phys. B: At. Mol. Opt. Phys.*, 39:L299–L304, 2006.

[91] A. Föhlisch, M. Nagasono, M. Deppe, E. Suljoti, F. Hennies, A. Pietzsch, and W. Wurth. *Phys. Rev. A*, 76:2–5, 2007.

[92] M. A. Baig and J. P. Connerade. *Journal of Physics B: Atomic and Molecular Physics*, 19:L605–L612, 1986.

[93] P. Emma, R. Akre, J. Arthur, R. Bionta, C. Bostedt, J. Bozek, A. Brachmann, P. Bucksbaum, R. Coffee, F. J. Decker, Y. Ding, D. Dowell, S. Edstrom, A. Fisher, J. Frisch, S. Gilevich, J. Hastings, G. Hays, Ph Hering, Z. Huang, R. Iverson, H. Loos, M. Messerschmidt, A. Miahnahri, S. Moeller, H. D. Nuhn, G. Pile, D. Ratner, J. Rzepiela, D. Schultz, T. Smith, P. Stefan, H. Tompkins, J. Turner, J. Welch, W. White, J. Wu, G. Yocky, and J. Galayda. *Nat.Photonics*, 4:641–647, 2010.

[94] G. Doumy, C. Roedig, S. K. Son, C. I. Blaga, A. D. Dichiara, R. Santra, N. Berrah, C. Bostedt, J. D. Bozek, P. H. Bucksbaum, J. P. Cryan, L. Fang, S. Ghimire, J. M. Glownia, M. Hoener, E. P. Kanter, B. Kr??ssig, M. Kuebel, M. Messerschmidt, G. G. Paulus, D. A. Reis, N. Rohringer, L. Young, P. Agostini, and L. F. Dimauro. *Phys. Rev. Lett.*, 106:083002, 2011.

[95] Benedikt Rudek, Sang-Kil Son, Lutz Foucar, Sascha W Epp, Benjamin Erk, Robert Hartmann, Marcus Adolph, Robert Andritschke, Andrew Aquila, Nora

Berrah, Christoph Bostedt, John Bozek, Nicola Coppola, Frank Filsinger, Hubert Gorke, Tais Gorkhover, Heinz Graafsma, Lars Gumprecht, Andreas Hartmann, Günter Hauser, Sven Herrmann, Helmut Hirsemann, Peter Holl, André Hömke, Loic Journel, Christian Kaiser, Nils Kimmel, Faton Krasniqi, Kai-Uwe Kühnel, Michael Matysek, Marc Messerschmidt, Danilo Miesner, Thomas Möller, Robert Moshammer, Kiyonobu Nagaya, Björn Nilsson, Guillaume Potdevin, Daniel Pietschner, Christian Reich, Daniela Rupp, Gerhard Schaller, Ilme Schlichting, Carlo Schmidt, Florian Schopper, Sebastian Schorb, Claus-Dieter Schröter, Joachim Schulz, Marc Simon, Heike Soltau, Lothar Strüder, Kiyoshi Ueda, Georg Weidenspointner, Robin Santra, Joachim Ullrich, Artem Rudenko, and Daniel Rolles. *Nat. Photonics*, 6:858–865, 2012.

[96] Tsumoru Shintake, Hitoshi Tanaka, Toru Hara, Takashi Tanaka, Kazuaki Togawa, Makina Yabashi, Yuji Otake, Yoshihiro Asano, Teruhiko Bizen, Toru Fukui, Shunji Goto, Atsushi Higashiya, Toko Hirono, Naoyasu Hosoda, Takahiro Inagaki, Shinobu Inoue, Miho Ishii, Yujong Kim, Hiroaki Kimura, Masanobu Kitamura, Toshiaki Kobayashi, Hirokazu Maesaka, Takemasa Masuda, Sakuo Matsui, Tomohiro Matsushita, Xavier Maréchal, Mitsuru Nagasono, Haruhiko Ohashi, Toru Ohata, Takashi Ohshima, Kazuyuki Onoe, Katsutoshi Shirasawa, Tetsuya Takagi, Sunao Takahashi, Masao Takeuchi, Kenji Tamasaku, Ryotaro Tanaka, Yoshihito Tanaka, Takanori Tanikawa, Tadashi Togashi, Shukui Wu, Akihiro Yamashita, Kenichi Yanagida, Chao Zhang, Hideo Kitamura, and Tetsuya Ishikawa. *Nat. Photonics*, 2:555–559, 2008.

[97] K. Motomura, H. Fukuzawa, L. Foucar, X.-J. Liu, G. Prümper, K. Ueda, N. Saito, H. Iwayama, K. Nagaya, H. Murakami, M. Yao, A. Belkacem, M. Nagasono, A. Higashiya, M. Yabashi, T. Ishikawa, H. Ohashi, and H. Kimura. *J. Phys. B: At. Mol. Phys*, 42:221003, 2009.

[98] Takahiro Sato, Atsushi Iwasaki, Kazuki Ishibashi, Tomoya Okino, Kaoru Yamanouchi, Junichi Adachi, Akira Yagishita, Hiroki Yazawa, Fumihiko Kannari, Makoto Aoyma, Koichi Yamakawa, Katsumi Midorikawa, Hidetoshi Nakano, Makina Yabashi, Mitsuru Nagasono, Atsushi Higashiya, and Tetsuya Ishikawa. *J. Phys. B: At. Mol. Opt. Phys.*, 44:161001, 2011.

[99] M. Meyer, J. T. Costello, S. Düsterer, W. B. Li, and P. Radcliffe. *J. Phys. B: At. Mol. Opt. Phys.*, 43:194006, 2010.

[100] V. Richardson, J. T. Costello, D. Cubaynes, S. Düsterer, J. Feldhaus, H. W. van der Hart, P. Juranić, W. B. Li, M. Meyer, M. Richter, A. A. Sorokin, and K. Tiedke. *Phys. Rev. Lett.*, 105:013001, 2010.

[101] L. V. Keldysh. *J. Exp. Theor. Phys.*, 20:1307–1314, 1965.

[102] H. R. Reiss. *Phys. Rev. A*, 82:023418, 2010.

[103] P. Lambropoulos, L. A A Nikolopoulos, and M. G. Makris. *Phys.Rev. A*, 72:013410, 2005.

[104] P. Lambropoulos and P. Zoller. *Phys.l Rev. A*, 24:379–397, 1981.

[105] K. Codling and R. P. Madden. *Phys. Rev. Lett.*, 12:106–108, 1964.

[106] K. Codling and R.P. Madden. *J. Res. Natl. Bur. Stand. A*, 76A:1, 1972.

[107] J. M. Bizau, C. Blancard, M. Coreno, D. Cubaynes, C. Dehon, N. El Hassan, F. Folkmann, M. F. Gharaibeh, A. Giuliani, J. Lemaire, A. R. Milosavljević, C. Nicolas, and R. Thissen. *J. Phys. B: At. Mol. Phys*, 44:055205, 2011.

[108] S. H. Southworth, D. A. Arms, E. M. Dufresne, R. W. Dunford, D. L. Ederer, C. Höhr, E. P. Kanter, B. Krässig, E. C. Landahl, E. R. Peterson, J. Rudati, R. Santra, D. A. Walko, and L. Young. *Phys. Rev. A*, 76:043421, 2007.

[109] M. Meyer, D. Cubaynes, V. Richardson, J. T. Costello, P. Radcliffe, W. B. Li, S. Düsterer, S. Fritzsche, A. Mihelic, K. G. Papamihail, and P. Lambropoulos. *Phys. Rev. Lett.*, 104:213001, 2010.

[110] A. Rouzée, P. Johnsson, E. V. Gryzlova, H. Fukuzawa, A. Yamada, W. Siu, Y. Huismans, E. Louis, F. Bijkerk, D. M. P. Holland, A. N. Grum-Grzhimailo, N. M. Kabachnik, M. J. J. Vrakking, and K. Ueda. *Phys. Rev. A*, 83:031401, 2011.

[111] E. V. Gryzlova, Ri Ma, H. Fukuzawa, K. Motomura, A. Yamada, K. Ueda, A. N. Grum-Grzhimailo, N. M. Kabachnik, S. I. Strakhova, A. Rouzée, A. Hundermark, M. J. J. Vrakking, P. Johnsson, K. Nagaya, S. Yase, Y. Mizoguchi, M. Yao, M. Nagasono, K. Tono, T. Togashi, Y. Senba, H. Ohashi, M. Yabashi, and T. Ishikawa. *Phys. Rev. A*, 84:063405, 2011.

[112] S. Mondal, R. Ma, K. Motomura, H. Fukuzawa, A. Yamada, K. Nagaya, S. Yase, Y. Mizoguchi, M. Yao, A. Rouzée, A. Hundertmark, M. J.J. Vrakking, P. Johnsson, M. Nagasono, K. Tono, T. Togashi, Y. Senba, H. Ohashi, M. Yabashi, T. Ishikawa, I. P. Sazhina, S. Fritzsche, N. M. Kabachnik, and K. Ueda. *J. Phys. B: At. Mol. Opt. Phys.*, 46:164022, 2013.

[113] M Braune, G Hartmann, A Ehresmann, A S Kheifets, J Viefhaus, M Ilchen, A Knie, T Lischke, A Reinköster, A Meissner, S Deinert, L Glaser, and O Al-Dossary. *J. Mod. Opt.*, 1:1–10, 2015.

[114] C. N. Yang. *Phys. Rev.*, 74:764–772, 1948.

[115] E. V. Gryzlova, A. N. Grum-Grzhimailo, S. Fritzsche, and N. M. Kabachnik. *J. Phys. B: At. Mol. Opt. Phys.*, 43:225602, 2010.

[116] S Fritzsche, A N Grum-Grzhimailo, E V Gryzlova, and N M Kabachnik. *J. Phys. B: At. Mol. Opt. Phys.*, 41:165601, 2008.

[117] Alexei N. Grum-Grzhimailo, Elena V. Gryzlova, Stephan Fritzsche, and Nikolay M. Kabachnik. *J. Mod. Opt.*, 63:334–357, 2016.

[118] L. A A Nikolopoulos. *Phys. Rev. Lett.*, 111:093001, 2013.

[119] E. V. Gryzlova, A. N. Grum-Grzhimailo, S. I. Strakhova, and M. Meyer. *J. Phys. B: At. Mol. Opt. Phys.*, 46:164014, 2013.

[120] A N Grum-Grzhimailo, E V Gryzlova, and M Meyer. *J. Phys. B: At. Mol. Opt. Phys.*, 45:215602, 2012.

[121] André T.J.B. Eppink and David H. Parker. *Rev. Sci. Instrum.*, 68:3477–3484, 1997.

[122] Lothar Strüder, Sascha Epp, Daniel Rolles, Robert Hartmann, Peter Holl, Gerhard Lutz, Heike Soltau, Rouven Eckart, Christian Reich, Klaus Heinzinger, Christian Thamm, Artem Rudenko, Faton Krasniqi, Kai Uwe K??hnel, Christian Bauer, Claus Dieter Schr??ter, Robert Moshammer, Simone Techert, Danilo Miessner, Matteo Porro, Olaf H??lker, Norbert Meidinger, Nils Kimmel, Robert Andritschke, Florian Schopper, Georg Weidenspointner, Alexander Ziegler, Daniel Pietschner, Sven Herrmann, Ullrich Pietsch, Albert Walenta, Wolfram Leitenberger, Christoph Bostedt, Thomas M??ller, Daniela Rupp, Marcus Adolph, Heinz Graafsma, Helmut Hirsemann, Klaus G??rtner, Rainer Richter, Lutz Foucar, Robert L. Shoeman, Ilme Schlichting, and Joachim Ullrich. *Nucl. Instrum. Methods Phys. Res. A*, 614:483–496, 2010.

[123] M. Richter, A. Gottwald, U. Kroth, A. A. Sorokin, S. V. Bobashev, L. A. Shmaenok, J. Feldhaus, Ch Gerth, B. Steeg, K. Tiedtke, and R. Treusch. *Appl. Phys. Lett.*, 83:2970–2972, 2003.

[124] Paul Kirkpatrick and A. V. Baez. *J. Opt. Soc. Am.*, 38:766, 1948.

[125] Benjamin Erk, Jan P. Müller, Cédric Bomme, Rebecca Boll, Günter Brenner, Henry N. Chapman, Jonathan Correa, Stefan Düsterer, Siarhei Dziarzhytski, Stefan Eisebitt, Heinz Graafsma, Sören Grunewald, Lars Gumprecht, Robert Hartmann, Günter Hauser, Barbara Keitel, Clemens von Korff Schmising, Marion Kuhlmann, Bastian Manschwetus, Laurent Mercadier, Erland Müller, Christopher Passow, Elke Plönjes, Daniel Ramm, Dimitrios Rompotis, Artem Rudenko, Daniela Rupp, Mario Sauppe, Frank Siewert, Dieter Schlosser, Lothar Strüder, Angad Swiderski, Simone Techert, Kai Tiedtke, Thomas Tilp, Rolf Treusch, Ilme Schlichting, Joachim Ullrich, Robert Moshammer, Thomas Möller, and Daniel Rolles. *J. Synchrotron Radiat.*, 25:1529–1540, 2018.

[126] K.-N. Huang, W.R. Johnson, and K.T. Cheng. *At. Data Nucl. Data Tables*, 26:33–45, 1981.

[127] J. L. Dehmer, W. A. Chupka, J. Berkowitz, and W. T. Jivery. *Phys. Rev. A*, 12:1966–1973, 1975.

[128] S. Fritzsche, A. N. Grum-Grzhimailo, E. V. Gryzlova, and N. M. Kabachnik. *J. Phys. B: At. Mol. Phys*, 41:165601, 2008.

[129] Christina H. M. van Oversteeg, Hoang Q. Doan, Frank M. F. de Groot, and Tanja Cuk. *Chem. Soc. Rev.*, 46:102–125, 2017.

[130] Eiji J. Takahashi, Tsuneto Kanai, Kenichi L. Ishikawa, Yasuo Nabekawa, and Katsumi Midorikawa. *Phys. Rev. Lett.*, 101:253901, 2008.

[131] Ch. Spielmann, N. H. Burnett, S. Sartania, R. Koppitsch, M. Schnürer, C. Kan, M. Lenzner, P. Wobrauschek, and F. Krausz. *Science*, 278:661–664, 1997.

[132] A. Bartnik, P. Wachulak, H. Fiedorowicz, R. Jarocki, J. Kostecki, and M. Szczurek. *Radiat. Phys. Chem.*, 93:9 – 13, 2013.

[133] I. Saber, A. Bartnik, P. Wachulak, W. Skrzeczanowski, R. Jarocki, and H. Fiedorowicz. *Springer Proceedings in Physics*, 202:203–211, 2018.

[134] A. Bartnik, P. Wachulak, H. Fiedorowicz, T. Fok, R. Jarocki, and M. Szczurek. *Phys. Plasmas*, 20:1–7, 2013.

[135] A. Bartnik, W. Skrzeczanowski, H. Fiedorowicz, P. Wachulak, and T. Fok. *Laser Part. Beams*, 36:76–83, 2018.

[136] A. Bartnik, P. Wachulak, H. Fiedorowicz, W. Skrzeczanowski, R. Jarocki, T. Fok, and Ł. Wegrzyński. *J. Instrum.*, 11:C03009–C03009, 2016.

[137] A. Bartnik, H. Fiedorowicz, P. Wachulak, and T. Fok. *Laser and Particle Beams*, 36:286–292, 2018.

[138] I Adamovich, S D Baalrud, A Bogaerts, P J Bruggeman, M Cappelli, V Colombo, U Czarnetzki, U Ebert, J G Eden, P Favia, D B Graves, S Hamaguchi, G Hieftje, M Hori, I D Kaganovich, U Kortshagen, M J Kushner, N J Mason, S Mazouffre, S Mededovic Thagard, H-R Metelmann, A Mizuno, E Moreau, A B Murphy, B A Niemira, G S Oehrlein, Z Lj Petrovic, L C Pitchford, Y-K Pu, S Rauf, O Sakai, S Samukawa, S Starikovskaia, J Tennyson, K Terashima, M M Turner, M C M van de Sanden, and A Vardelle. *J. Phys. D, Appl. Phys.*, 50:323001, 2017.

[139] Bruce A. Remington, R. Paul Drake, and Dmitri D. Ryutov. *Rev. Mod. Phys.*, 78:755–807, 2006.

[140] S. Stipcich A. Bianconi, L. Incoccia. Springer-Verlag Berlin Heidelberg, Reading, Massachusetts, 1983.

[141] J. A. Sheehy, T. J. Gil, C. L. Winstead, R. E. Farren, and P. W. Langhoff. *J. Chem. Phys.*, 1989.

[142] M Larsson, W D Geppert, and G Nyman. *Rep. Prog. Phys.*, 75:066901, 2012.

[143] J B West. *J. Phys. B: At. Mol. Phys*, 34:R45–R91, 2001.

[144] I C Lyon, B Peart, J B West, and K Dolder. *J. Phys. B: At. Mol. Phys.*, 19:4137–4147, 1986.

[145] I C Lyon, B Peart, K Dolder, and J B West. *J. Phys. B: At. Mol. Phys.*, 20:1471–1477, 1987.

[146] T Koizumi, Y Itoh, M Sano, M Kimura, T M Kojima, S Kravis, A Matsumoto, M Oura, T Sekioka, and Y Awaya. *J. Phys. B: At. Mol. Phys.*, 28:609–616, 1995.

[147] A. M. Covington, A. Aguilar, I. R. Covington, M. F. Gharaibeh, G. Hinojosa, C. A. Shirley, R. A. Phaneuf, I. Álvarez, C. Cisneros, I. Dominguez-Lopez, M. M. Sant'Anna, A. S. Schlachter, B. M. McLaughlin, and A. Dalgarno. *Phys. Rev. A*, 66:062710, 2002.

[148] M F Gharaibeh, J M Bizau, D Cubaynes, S Guilbaud, N El Hassan, M M Al Shorman, C Miron, C Nicolas, E Robert, C Blancard, and B M McLaughlin. *J. Phys. B: At. Mol. Phys*, 44:175208, 2011.

[149] Stefan Schippers, Ticia Buhr, Alexander Borovik Jr., Kristof Holste, Alexander Perry-Sassmannshausen, Karolin Mertens, Simon Reinwardt, Michael Martins, Stephan Klumpp, Kaja Schubert, Sadia Bari, Randolf Beerwerth, Stephan Fritzsche, Sandor Ricz, Jonas Hellhund, and Alfred Müller. *X-Ray Spectrom.*, pages 1–10, 2019.

[150] E.T Kennedy, J.T Costello, J.-P Mosnier, and P van Kampen. *Radiat. Phys. Chem.*, 70:291 – 321, 2004.

[151] A. Carillon, P. Jaegle, and P. Dhez. *Phys. Rev. Lett.*, 25:140–143, 1970.

[152] J. Balmer, C. L. S. Lewis, R. E. Corbett, E. Robertson, S. Saadat, D. O'Neill, J. D. Kilkenny, C. A. Back, and R. W. Lee. *Phys. Rev. A*, 40:330–340, 1989.

[153] R D'Arcy, J T Costello, C McGuinness, and G O'Sullivan. *J. Phys. B: At. Mol. Phys*, 32:4859–4876, 1999.

[154] G O'Sullivan. *J. Phys. B: At. Mol. Phys.*, 15:L327–L330, 1982.

[155] G O'Sullivan. *J. Phys. B: At. Mol. Phys.*, 15:2385–2390, 1982.

[156] Toshiaki Kita, Tatsuo Harada, N. Nakano, and H. Kuroda. *Appl. Opt.*, 22:512–513, 1983.

[157] Tatsuo Harada and Toshiaki Kita. *Appl. Opt.*, 19:3987–3993, 1980.

[158] P. W. Wachulak, A. Bartnik, H. Fiedorowicz, T. Feigl, R. Jarocki, J. Kostecki, R. Rakowski, P. Rudawski, M. Sawicka, M. Szczurek, A. Szczurek, and Z. Zawadzki. *Appl. Phys. B: Lasers and Optics*, 100:461–469, 2010.

[159] Raymond L. Kelly. *J. Phys. Chem. Ref. Data*, 16:1–649, 1988.

[160] T. K. Sham, B. X. Yang, J. Kirz, and J. S. Tse. *Phys. Rev. A*, 40:652–669, 1989.

[161] John D. Bozek, Norio Saito, and Isao H. Suzuki. *Phys. Rev. A*, 51:4563–4574, 1995.

[162] Y. Ma, C. T. Chen, G. Meigs, K. Randall, and F. Sette. *Phys. Rev. A*, 44:1848–1858, 1991.

[163] Stephen G. Urquhart and Rob Gillies. *J. Phys. Chem. A*, 109:2151–2159, 2005.

[164] G.R. Wight and C.E. Brion. *J. Electron. Spectrosc. Relat. Phenom.*, 4:335 – 345, 1974.

[165] K. Ueda, M. Okunishi, H. Chiba, Y. Shimizu, K. Ohmori, Y. Sato, E. Shigemasa, and N. Kosugi. *Chem. Phys. Lett.*, 236:311 – 317, 1995.

[166] A. Kivimäki, M. Neeb, B. Kempgens, H. M. Köppe, and A. M. Bradshaw. *J. Phys. B: At. Mol. Phys.*, 29:2701–2709, 1996.

[167] U. Ekström, V. Carravetta, M. Alagia, M. Lavolle, R. Richter, C. Bolcato, and S. Stranges. *J. Chem. Phys.*, 128:044302, 2008.

[168] Gérald Dujardin, Dominique Winkoun, and Sydney Leach. *Phys. Rev. A*, 31:3027–3038, 1985.

[169] L E Berg, A Karawajczyk, and C Stromholm. *J. Phys. B: At. Mol. Phys.*, 27:2971–2980, 1994.

[170] P A Hatherly, K Codling, M Stankiewicz, and M Roper. *J. Phys. B: At. Mol. Phys.*, 28:3249–3260, 1995.

[171] Z. D. Pesic, D. Rolles, R. C. Bilodeau, I. Dimitriu, and N. Berrah. *Phys. Rev. A*, 78:051401, 2008.

[172] G. R. Wight and C. E. Brion. *Journal of Electron Spectroscopy and Related Phenomena*, 3:191–205, 1974.

[173] Gunnar Öhrwall, M. M. Sant'Anna, W. C. Stolte, I. Dominguez-Lopez, L. T.N. Dang, A. S. Schlachter, and D. W. Lindle. *J. Phys. B: At. Mol. Phys.*, 35:4543–4552, 2002.

[174] Alexander Kramida. *Atoms*, 7:64, 2019.

[175] K Kawatsura, H Yamaoka, M Oura, T Hayaishi, T Sekioka, A Agui, A Yoshigoe, and F Koike. *J. Phys. B: At. Mol. Phys.*, 35:4147–4153, 2002.

[176] A. Aguilar, A. M. Covington, G. Hinojosa, R. A. Phaneuf, I. Alvarez, C. Cisneros, J. D. Bozek, I. Dominguez, M. M. Sant'Anna, A. S. Schlachter, S. N. Nahar, and B. M. McLaughlin. *Astrophys. J. Suppl. Ser.*, 146:467–477, 2003.

[177] H. Kjeldsen, B. Kristensen, R. L. Brooks, F. Folkmann, H. Knudsen, and T. Andersen. *Astrophys. J. Suppl. Ser.*, 138:219–227, 2002.

[178] H. Kjeldsen, J. E. Hansen, F. Folkmann, H. Knudsen, J. B. West, and T. Andersen. *Astrophys. J. Suppl. Ser.*, 135:285–295, 2001.

[179] H. Kjeldsen, F. Folkmann, J. E. Hansen, H. Knudsen, M. S. Rasmussen, J. B. West, and T. Andersen. *Astrophys. J.*, 524:L143–L146, 1999.

[180] J. M. Bizau, D. Cubaynes, S. Guilbaud, M. M. Al Shorman, M. F. Gharaibeh, I. Q. Ababneh, C. Blancard, and B. M. McLaughlin. *Phys. Rev. A*, 92:023401, 2015.

[181] A S Schlachter, M M SantAnna, A M Covington, A Aguilar, M F Gharaibeh, E D Emmons, S W J Scully, R A Phaneuf, G Hinojosa, I 'Alvarez, C Cisneros, A Müller, and B M McLaughlin. *J. Phys. B: At. Mol. Phys*, 37:L103–L109, 2004.

[182] David Brewster. *Trans. R. Soc. Edinburgh*, 12:519–530, 1834.

[183] George W. Stroke. *Progress in Optics*. 1963.

[184] Patrick Nuernberger, Gerhard Vogt, Tobias Brixner, and Gustav Gerber. *Phys. Chem. Chem. Phys.*, 9:2470, 2007.

[185] T. Baumert, T. Brixner, V. Seyfried, M. Strehle, and G. Gerber. *Appl. Phys. B*, 65:779–782, 1997.

[186] Hirofumi Sakai, H. Stapelfeldt, E. Constant, M. Yu Ivanov, Daniel R. Matusek, James S. Wright, and P. B. Corkum. *Phys. Rev. Lett.*, 81:2217–2220, 1998.

[187] W. C. Wiley and I. H. McLaren. Time-of-flight mass spectrometer with improved resolution. *Rev. Sci. Instrum.*, 26:1150–1157, 1955.

[188] David A. Dahl. *Int. J. Mass Spectrom.*, 200:3–25, 2000.

[189] P. A. Franken, A. E. Hill, C. W. Peters, and G. Weinreich. *Phys. Rev. Lett.*, 7:118–119, 1961.

[190] S. Baker, J. S. Robinson, C. A. Haworth, H. Teng, R. A. Smith, C. C. Chirilă, M. Lein, J. W.G. Tisch, and J. P. Marangos. *Science*, 312:424–427, 2006.

[191] Z. Chen, X. Wang, B. Wei, S. Lin, R. Hutton, and Y. Zou. *Phys. Scr.*, T144:014065, 2011.

[192] Chengyin Wu, Zhifeng Wu, Qingqing Liang, Min Liu, Yongkai Deng, and Qihuang Gong. *Phys. Rev. A*, 75:1–6, 2007.

[193] Sufan Wang, Xiaoping Tang, Lirong Gao, Mohamed E. Elshakre, and Fanao Kong. *J. Phys. Chem. A*, 107:6123–6129, 2003.

[194] M. Sharifti, F. Kong, S. L. Chin, H. Mineo, Y. Dyakov, A. M. Mebel, S. D. Chao, M. Hayashi, and S. H. Lin. *J. Phys. Chem. A*, 111:9405–9416, 2007.

[195] P. B. Corkum. *Phys. Rev. Lett.*, 71:1994–1997, 1993.

[196] K. Nagesha, V. R. Marathe, and D. Mathur. *Rapid Commun. Mass Spectrom.*, 5:15–18, 1991.

[197] D. Mathur and F. A. Rajgara. *J. Chem. Phys.*, 124, 2006.

[198] David W. Chandler and Paul L. Houston. *J. Chem. Phys.*, 87:1445–1447, 1987.

[199] Jack Solomon. *J. Chem. Phys.*, 47:889–895, 1967.

[200] Christoph R. Gebhardt, T. Peter Rakitzis, Peter C. Samartzis, Vlassis Ladopoulos, and Theofanis N. Kitsopoulos. *Rev. Sci. Instrum.*, 72:3848–3853, 2001.

[201] Michael N.R. Ashfold, N. Hendrik Nahler, Andrew J. Orr-Ewing, Olivier P.J. Vieuxmaire, Rachel L. Toomes, Theofanis N. Kitsopoulos, Ivan Anton Garcia, Dmitri A. Chestakov, Shiou Min Wu, and David H. Parker. *Phys. Chem. Chem. Phys.*, 8:26–53, 2006.